Science of Climate Change

Volume 2.3
2022

https://scienceofclimatechange.org

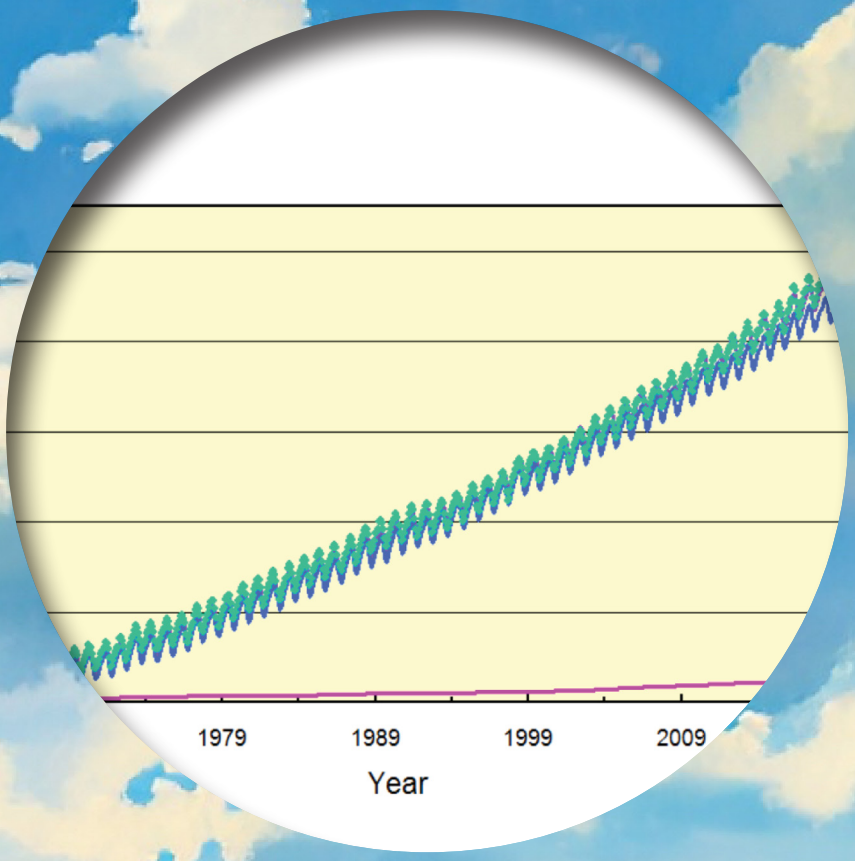

Published by: Klimarealistene (Org. no. 995 314 592)

ISSN 2703-9080 (print) ISNN 2703-9072 (online)

Increase in Atmospheric CO_2 since 1959

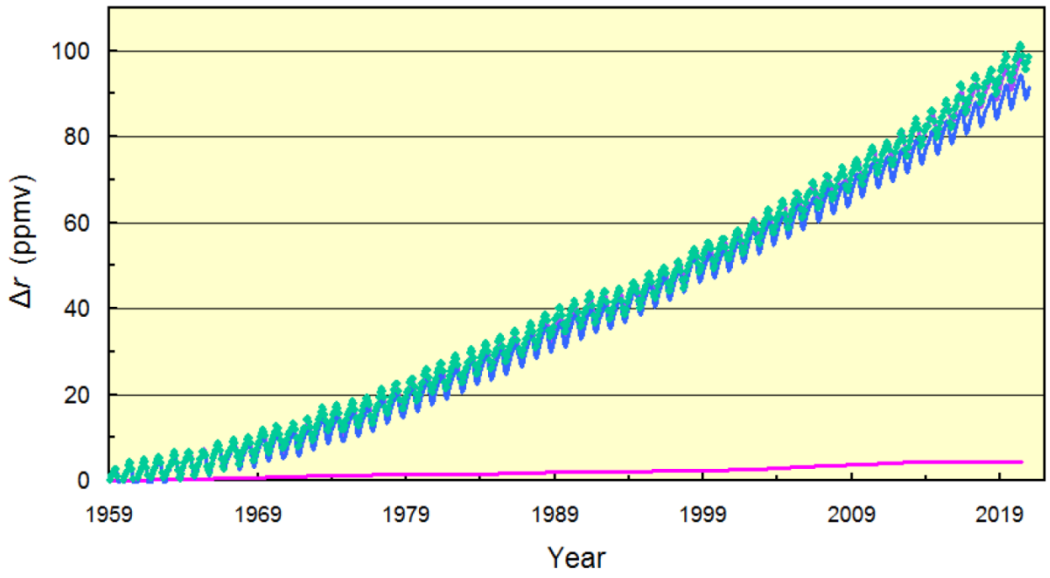

Observed increase of atmospheric CO_2 (Green), compared against the calculated increase (Purple) since 1959. Note: Calculated CO_2 lies mostly beneath observed CO_2 but emerges near the end of the record. Plotted separately is the contribution from thermally-induced emission (Blue) and the contribution from anthropogenic emission (Magenta). The anthropogenic component represents 4.1%.

From an article by Murry Salby and Hermann Harde: *Theory of Increasing Greenhouse Gases.*

Figure 11, page 229

SCIENCE OF CLIMATE CHANGE

Volume 2.3

December 2022

ISSN 2703-9072

Klimarealistene, P.O. Box 33, 3901 Porsgrunn, Norway

Table of Content

Editorial

With this edition Science of Climate Change finishes its second volume. We managed only three issues in this volume, because of a long halt in the editorial work. However, we are proud of finishing in the month prescribed on the title, and we express the hope that we can in the future can keep the schedule and publish quarterly issues.

This issue is first of all a follow up with various papers about the relation between natural and fossil emission of CO_2. Murry Salby and Hermann Harde finish the triology on CO2-origin with a theory for the increasing greenhouse gases. Hans Schrøder calculates the fossil fraction by a balanced network solving simultaneous linear equations, and Harald Yndestad analyze the variations in global CO_2 from Mauna Kea and as estimated by Ernst-Georg Beck back to 1870, and finds the temporal spectrum coinciding with the global sea surface temperature and lunar nodal tide variability. This is another manifestation of natural origin of atmospheric CO_2.

We expect the conclusions about nature providing most of the CO_2 will be challenged, and we have already received commentaries which will be published in the next volume.

Finally we have two articles about climate change during Holocene and the uplift in Norway as a result of glacier unloading since the Little Ice Age, The third and not the last Holocene paper is under consideration for the next issue, which we hope will be published on schedule.

Good reading

Jan-Erik Solheim
Editor

A digital version of this volume can be found here: https://doi.org/10.53234/scc202308/16

SCC

Correspondence to
harde@hsu-hh.de

Vol. 2.3 (2022)
pp. 212-238

Theory of Increasing Greenhouse Gases

Murry Salby[†1], *Hermann Harde*[2]

[1]*Ex Macquarie University, Sydney, Australia*

[2]*Helmut-Schmidt-University, Hamburg, Germany*

Abstract

Unlike elsewhere on the globe, temperature in the tropics has increased systematically. From observed tropical temperature, numerical simulations have reproduced the observed evolution of atmospheric CO_2, including its annual cycle. Much the same has followed empirically from the observed covariance between tropical temperature and *net* emission of CO_2 - the component of emission that actually changes CO_2. Intensified over tropical land, the robust coherence between those observed features establishes that the changes of tropical temperature do not follow from changes of CO_2, but rather produce them.

Here, we investigate the physical mechanisms through which observed warming in the tropics can produce the observed evolution of CO_2. The conservation law governing atmospheric CO_2, supported by the observed temperature dependence of surface fluxes and observed temperature in the tropics, is used to calculate the time-varying response of CO_2 net emission.

Thermally-induced emission is found to account for the preponderance of CO_2 net emission and, thereby, for the vast majority of anomalous CO_2. Magnified over tropical land, it represents interannual intensifications of net emission, notably during episodes of El Niño. Represented equally well is the long-term intensification of net emission during the last half century. That intensification alone accounts for about half of the observed increase of atmospheric CO_2. Anomalous CO_2 introduced by the calculated net emission closely tracks the observed evolution of atmospheric CO_2.

Having similar dependence on temperature is methane. Like net emission of CO_2, net emission of methane is intensified by tropical warming. The simultaneous intensification of CO_2 and CH_4 emission provides a unified understanding of their joint increase, one that follows naturally from thermally-induced emission.

Keywords: Carbon cycle; greenhouse gases; thermally induced CO_2; anthropogenic CO_2; absorption time; mixing ratio; CH_4 emission; tropical temperature change.

Submitted 2022-10-24, Accepted 2022-11-29. https://doi.org/10.53234/scc202212/17

1. Introduction

Preceding studies performed an in-depth analysis on nuclear-perturbed carbon 14, a tracer of carbon dioxide, through which it determined the effective absorption rate of atmospheric CO_2 (Harde and Salby 2021; Salby and Harde 2021a, hereafter SH1). In concert with the conserva-

[†1] Murry Salby unexpectedly passed away, when the manuscript to this contribution was almost ready for submission. As the third and culminating paper of a trifecta, which comprehensively treats the increase of greenhouse gases in the atmosphere, it was a deep commitment to complete this publication, in memoriam of Murry Salby.

tion law governing atmospheric CO_2, the effective absorption rate, in turn, determines the instantaneous equilibrium level of "anthropogenic CO_2" - the perturbation of CO_2 introduced by anthropogenic emission. Representing an upper bound on anthropogenic CO_2, its equilibrium level is much too small for anthropogenic emission to be responsible for the observed increase of atmospheric CO_2.

A companion study then found that much of the observed evolution of *net* CO_2 emission, the component of emission that changes CO_2, is represented by thermally-induced emission: the perturbation of natural emission that accompanies changes of temperature - notably in the tropics, where temperature has increased systematically (Salby and Harde 2021b, hereafter SH2). Represented by thermally-induced emission are sporadic intensifications of net emission, like those observed during episodes of El Niño. Represented equally well is the long-term intensification of net emission, which accelerated CO_2 growth during the last half century. Jointly, these components of net emission yield a thermally-induced perturbation of CO_2 that tracks the observed evolution of CO_2.

Both studies were inspired by numerical simulations which, on the basis of observed temperature, were able to reproduce the observed evolution of atmospheric CO_2, including its annual variation and stepwise increase (see: Harde 2017; Harde 2019; Harde and Salby 2021). Here, we explore the underlying physical mechanisms through which observed changes of temperature can produce the observed evolution of CO_2. Following an overview of the global equilibrium that controls atmospheric CO_2, Section 3 develops how the thermally-induced response to warming results through the conservation law that governs atmospheric CO_2. Section 4 applies the conservation law to calculate the thermally-induced response of net emission to observed warming, along with the resulting change of CO_2. The calculated evolution of CO_2 is then compared against its observed evolution. Finally, Section 5 briefly discusses the CH_4 increase with temperature analogous to CO_2.

2. Global Equilibrium of CO_2

Carbon dioxide in the atmosphere is controlled by a competition between its introduction through global-mean emission, E, and its removal through global-mean absorption, A. This physical constraint is expressed by the conservation law governing atmospheric CO_2:

$$\frac{dr_A}{dt} = E - A = E_{net}, \tag{1}$$

where r_A is the global-mean mixing ratio of atmospheric CO_2 and E_{net} is its global net emission into the atmosphere - the resultant of all contributions. As developed elsewhere (SH2), E_{net} is a small residual of the two competing influences, of order only a few % of E and A. Consequently, CO_2 remains in a state of quasi-equilibrium globally, wherein its emission and absorption approximately cancel one another. The conservation law then reduces to

$$E \cong A = \alpha_{eff} \cdot r_A, \tag{2.1}$$

where α_{eff} is the effective rate of CO_2 absorption. In (2.1), absorption of CO_2 is proportional to the instantaneous abundance of CO_2. Ubiquitous among physical systems, this form of damping is an observed feature of CO_2. It is manifest in the exponential decline of its nuclear-perturbed isotope $^{14}CO_2$, a tracer of overall CO_2 (Harde and Salby 2021; SH1).

Although global emission and absorption remain nearly in balance, their equilibrium can nonetheless drift through changes of emission. By changing atmospheric CO_2, changes of emission induce parallel changes of absorption (2.1), which maintain global CO_2 in quasi equilibrium. According to (1), however, the induced changes of r_A follow, not from E directly, but from its small residual, E_{net}, which determines anomalous CO_2.

The quasi-equilibrium that controls CO_2 globally does not apply locally. Local net emission

($e-a$) is equal to CO_2 flux that is observed locally. Plotted in Fig. 1 as a function of latitude, local net emission is positive in the tropics, over ocean as well as over land (Wanninkhof 1992; Palmer et al. 2019). To maintain global equilibrium, net emission has opposite sign in the extratropics, becoming negative poleward of $\Phi = 20°$:

$$e-a>0 \quad \text{for} \quad |\phi|<20°; \qquad e-a<0 \quad \text{for} \quad |\phi|>20°. \tag{2.2}$$

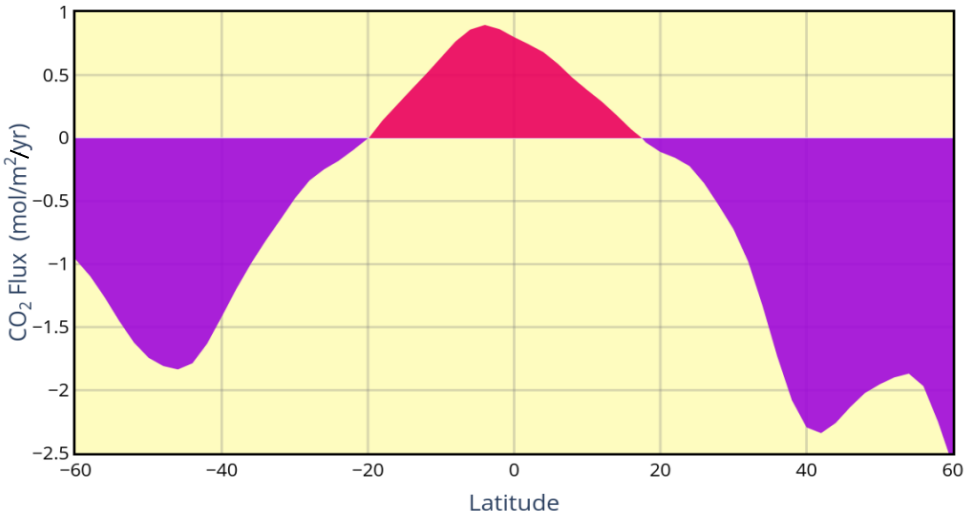

Figure 1: Local CO_2 flux evaluated from CO_2 partial pressure of ocean surface and atmosphere, averaged from estimates of Wanninkhof and McGillis (1999) and Nightingale et al. (2000).

Therefore, net emission integrated over the tropics, $E_T = \int (e-a)\, dS_x$, comprises global emission of CO_2 in (1):

$$E = E_T. \tag{2.3}$$

Likewise, net emission integrated over the extratropics, $A_x = -\int (e-a)\, dS_x$, comprises global absorption of CO_2:

$$A = A_X. \tag{2.4}$$

Global quasi-equilibrium is thus expressed by

$$E_T \cong A_X = \alpha_{eff} \cdot r_A. \tag{3}$$

Further, because CO_2 is well mixed over the atmosphere, on time scales longer than a couple of months, it is largely invariant with latitude.

If subjected to a positive perturbation of emission, $\delta E_T > 0$, the Earth-Atmosphere System (EASy) will adjust to re-establish equilibrium. It does so by increasing r_A until the ensuing perturbation of absorption, $\alpha_{eff} \cdot \delta r_A$, just balances the perturbation of emission, δE_T.

Relationship to Surface Properties

In the tropics, total emission of CO_2 has contributions from Ocean and Land. Those contributions follow from the respective fluxes, E_O and E_L, integrated over surface area:

$$\begin{aligned} E_T &= E_O + E_L \\ &= S\{S_O F_O + S_L F_L\}, \end{aligned} \tag{4}$$

where F_O and F_L denote areal-mean surface fluxes over ocean and land, S_O and S_L the fractional contributions of the tropics occupied by ocean and land, and S the total tropical area.

Over ocean, CO_2 flux is determined by the Atmosphere-Ocean contrast of CO_2:

$$F_O = G(k,s,Sc,v)\cdot\Delta r, \tag{5.1}$$

where

$$\Delta r = r_O - r_A, \tag{5.2}$$

r_O is the mixing ratio of ocean CO_2 (viz of air at equilibrium with ocean surface), G is an empirical function of gas transfer velocity k, solubility s, Schmidt number Sc, and wind speed v. Now, r_O in ppmv is equivalent to the partial pressure of CO_2 in μatm at the surface. Therefore,

$$\Delta r(\text{ppmv}) \Leftrightarrow \Delta p_{CO2}(\mu\text{atm}), \tag{5.3}$$

Δr(ppmv) representing the atmosphere-ocean contrast of CO_2 partial pressure. In (5.1), the temperature dependence of solubility and Schmidt number offset one another (Wanninkhof 2014; Etcheto and Merlivat 1988). Consequently, ocean CO_2 flux (5.1) depends primarily upon wind speed and the atmosphere-ocean contrast of CO_2:

$$F_O \cong B(v)\cdot\Delta r. \tag{6.1}$$

Over land, CO_2 flux follows from soil respiration

$$F_L \cong R(T,\text{m}), \tag{6.2}$$

which depends upon soil temperature T and moisture m. Soil respiration derives from microbial activity and upward diffusion of the produced CO_2 (cf. Maier et al. 2020). It is noteworthy that the partial pressure of CO_2 in soil vastly exceeds its partial pressure in the atmosphere. At 500 - 20,000 ppmv,

$$r_L >> r_A.$$

For a uniform perturbation of surface conditions, the enormous partial pressures of CO_2 found just a few tens of cm beneath the surface makes emission from land determinative in re-establishing equilibrium between the atmosphere and the Earth's surface.

Although R is influenced by soil moisture, it is controlled chiefly by surface temperature (Wood et al. 2013; Zhou et al. 2013), which is determined by air temperature:

$$F_L \cong R(T). \tag{7}$$

The temperature sensitivity of soil respiration,

$$Q_L = \frac{1}{R}\frac{dR}{dT}, \tag{8}$$

is observed in the range 10%/K - 25%/K at temperate and polar latitudes (Reich and Schlesinger 1992; Lloyd and Taylor 1994). In tropical forest, however, copious precipitation and sunlight magnify active biomass, which supports soil respiration. There, the observed sensitivity to temperature is greatest (ibid; Brechet et al. 2018), 30%/K and higher (Wood et al. 2013; Nottingham et al. 2018).

3. Perturbation of Tropical Temperature

Consider now a positive perturbation of tropical surface temperature:

$$\delta T_T > 0,$$

which is imposed and then maintained. Through the temperature sensitivity of surface fluxes, $\delta T_T > 0$ introduces a perturbation in emission, δE_T. It increases E_T, which is then no longer balanced by $A_X = \alpha_{eff}\cdot r_A$ in (2.1). EASy is thus driven out of global equilibrium, with positive net global emission (1). Initially, the atmosphere is unperturbed: $\delta r_A = 0$, so $E_{net} = \delta E_T > 0$. Net emission, however, increases atmospheric CO_2. Accompanying the increase of r_A is an increase of CO_2 absorption, $\alpha_{eff}\cdot\delta r_A$. Atmospheric CO_2 continues to increase until the perturbation of

absorption again balances the perturbation of emission, re-establishing global equilibrium (2.1).

According to (3), (5), and (6), the initial and final equilibria satisfy the balances:

$$S\{S_O B(\nu)\cdot\Delta r + S_L R\} = \alpha_{eff}\cdot r_A \tag{9.1}$$

$$S\{S_O B(\nu)\cdot(\Delta r+\delta\Delta r) + S_L (R+\delta R)\} = \alpha_{eff}\cdot(r_A+\delta r_A)\cdot \tag{9.2}$$

Subtraction yields the balance governing the perturbation:

$$S\{S_O B(\nu)\cdot\delta\Delta r + S_L \delta R\} = \alpha_{eff}\cdot\delta r_A, \tag{9.3}$$

where the LHS represents the perturbation of emission with $\delta\Delta r$ as the perturbation of the atmosphere-ocean contrast Δr and δR as perturbation of the respiration. Dividing (9.3) by (9.1) obtains

$$\frac{S_O B(\nu)\cdot\delta\Delta r + S_L\delta R}{S_O B(\nu)\cdot\Delta r + S_L R} = \frac{\delta r_A}{r_A}. \tag{10}$$

The fractional perturbation of atmospheric CO_2 equals the fractional perturbation of emission, independently of effective absorption.

3.1 Aqua Tropics: $S_L = 0$

In the absence of land, (10) reduces to

$$\frac{\delta r_A}{r_A} = \frac{\delta\Delta r}{\Delta r}, \tag{11}$$

or with (5.2)

$$\frac{\delta r_A}{r_A} = \frac{\delta r_O - \delta r_A}{r_O - r_A}. \tag{12}$$

Upon rearrangement, (12) yields

$$\frac{\delta r_A}{r_A} = \frac{\delta r_O}{r_O}. \tag{13}$$

The fractional increase of atmospheric CO_2 is identical to the fractional increase of ocean CO_2. The latter, in turn, is imposed though the increase of surface temperature, $\delta T_T = \delta T_O$.

Ocean surface temperature is represented in the Sea Surface Temperature Anomaly (SSTA). Plotted in Fig. 2, the record of tropical SSTA extends back through the onset of CO_2 measurements at Mauna Loa, albeit with reduced coverage before the satellite era. At the beginning of the Mauna Loa record, ocean surface in the tropics ($|\phi| < 20°$) had a temperature anomaly of

$$T_O(1959) \cong -0.2\,\mathrm{K}, \tag{14.1}$$

corresponding to an actual surface temperature of about 300 K (26.9°C). During the subsequent era of CO_2 measurements, tropical ocean temperature increased systematically, attaining a net increase in closing years of

$$\delta T_O \cong +0.9\,\mathrm{K}\cdot \tag{14.2}$$

To investigate its impact, δT_O is imposed impulsively in 1959, the start of the Mauna Loa record, and thereafter maintained.[2]

[2] The equilibrium properties in (9) are state variables. Therefore, the transition between the two states is path independent and, hence, independent of whether δT_O is introduced gradually or impulsively.

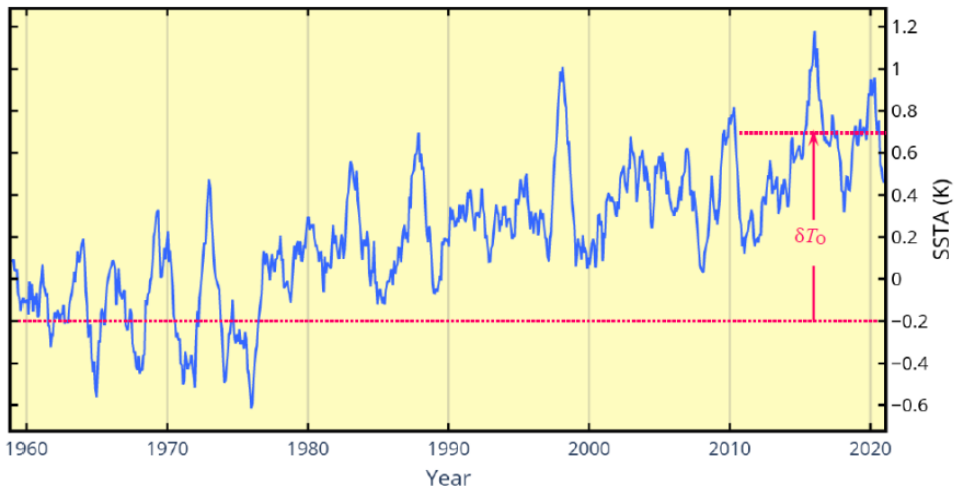

Figure 2: Anomalous sea surface temperature in the tropic (20°S – 20°N). Source HadSST4.0 (Kennedy et al. 2019).

Chemical equilibrium of seawater is governed by carbonate chemistry. Involving dissolved ions, it is determined chiefly by the following reactions (eg., Zeebe 2012):

$$CO_2(g) \Leftrightarrow CO_2(aq) \tag{15.1}$$

$$CO_2(aq) + H_2O \Leftrightarrow H^+ + HCO_3^- \tag{15.2}$$

$$HCO_3^- \Leftrightarrow H^+ + CO_3^{2-}, \tag{15.3}$$

wherein the concentrations [ ] of species define the conserved families: Dissolved Inorganic Carbon (DIC), equivalent to total carbon, and Total Alkalinity (TA) as:

$$DIC = [CO_2(aq)] + [HCO_3^-] + [CO_3^{2-}] \tag{15.4}$$

$$TA = [HCO_3^-] + 2[CO_3^{2-}] + [B(OH)_4^-] + [OH^-] - [H^+] \tag{15.5}$$

with $B(OH)_4^-$ as tetrahydroxyborate. The reactions (15) are temperature dependent. So too then is the chemical equilibrium they describe. In addition to temperature (14.1), chemical equilibrium of the ocean surface is determined by the values of total alkalinity (e.g., Jiang et al. 2014)

$$TA = 2350\ \mu\text{mol/kg} \tag{16.1}$$

and dissolved inorganic carbon (e.g., Wu 2019)

$$DIC = 2000\ \mu\text{mol/kg}, \tag{16.2}$$

properties to which the ocean partial pressure of CO_2 is sensitive.[3]

Through (15), T_O, TA, and DIC determine ocean CO_2. At the start of the Mauna Loa record, chemical equilibrium defined by the above values had ocean CO_2 of

$$r_O = r_O(1959) \cong 354\,\text{ppmv}. \tag{16.3}$$

In the atmosphere, CO_2 then was

$$r_A = r_A(1959) \cong 315\,\text{ppmv}. \tag{16.4}$$

[3] In open ocean, TA varies by +/- 40 μmol/kg. At ocean boundaries it varies even more, by as much as 100 μmol/kg. Such changes have a huge impact on the ocean partial pressure of CO_2: At TA=2300 μmol/kg, a decrease of 40 μmol/kg increases r_O by 175 ppmv (e.g., Robbins et al. 2010). A decrease of 100 μmol/kg increases r_O by 580 ppmv.

The initial atmosphere-ocean contrast of CO_2 was therefore

$$\Delta r(1959) \cong 39\,\text{ppmv}. \tag{16.5}$$

From its initial temperature (14.1), tropical ocean surface warmed during the Mauna Loa era, resulting in the temperature perturbation (14.2) in 2020. This increase of temperature perturbed the ocean surface, driving it to a new chemical equilibrium. The perturbed equilibrium at the new temperature, $T_O + \delta T_O$, has the perturbed CO_2

$$r_O + \delta r_O \cong 367\,\text{ppmv}. \tag{17}$$

According to (16.3) and (17), the temperature perturbation increased ocean CO_2 by

$$\delta r_O \cong 13\,\text{ppmv}. \tag{18.1}$$

The increase of atmospheric CO_2 that eventually results from this increase of ocean CO_2 follows from (13):

$$\delta r_A = (13/354)\cdot 315 \cong 12\,\text{ppmv}. \tag{18.2}$$

Initially, the atmosphere was unperturbed: $\delta r_A\,(1959) = 0$, as illustrated in Fig. 3. The initial perturbation to atmosphere-ocean contrast of CO_2 was therefore

$$\begin{aligned}\delta\Delta r(t=0) &= \delta r_O(1959) - \delta r_A(1959)\\ &= \delta r_O(1959) = 13\,\text{ppmv}\end{aligned}. \tag{19.1}$$

In response to the surface perturbation, however, the resulting disequilibrium with the atmosphere generates positive net emission. Thereby, atmospheric CO_2 develops a perturbation, δr_A (Blue), which steadily increases. It, in turn, increases the back pressure exerted on the ocean surface, which opposes the ocean flux (6) by reducing the atmosphere-ocean contrast of CO_2 (Red). When equilibrium is re-established, the negative feedback of δr_A has increased sufficiently to reduce the perturbation in CO_2 contrast to:

$$\begin{aligned}\delta\Delta r(t\to\infty) &= \delta r_O - \delta r_A(t\to\infty)\\ &\cong 13 - 12\,\text{ppmv} \cong 1\,\text{ppmv}\end{aligned}, \tag{19.2}$$

now with a slightly smaller contrast of Δr = 38 ppmv and a final atmospheric mixing ratio caused only by the oceans of r_A = 327 ppmv.

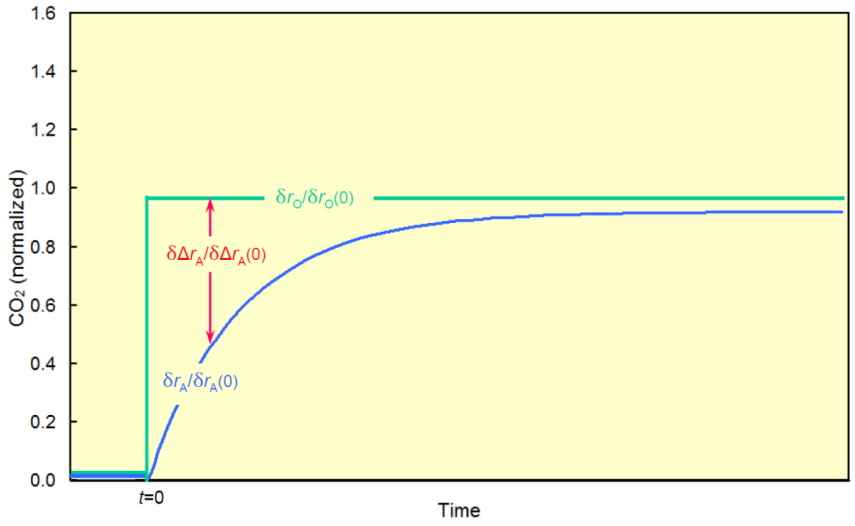

Figure 3: Evolution of anomalous CO_2 in ocean (Green) and in atmosphere (Blue), along with atmosphere-ocean contrast of CO_2 (Red).

https://doi.org/10.53234/scc202212/17

The final perturbation of Δr in the new equilibrium (19.2) is less than 8% of its initial perturbation (19.1). Hence, the atmosphere-ocean contrast of CO_2 changes little, a feature of the observed record (Fig. 4).[4] By eliminating most of the perturbation in Δr, the increased back pressure exerted by the atmosphere $\delta r_A(t \to \infty)$ simultaneously eliminates most of the perturbation in ocean emission, δE_O ; (4) - (5).

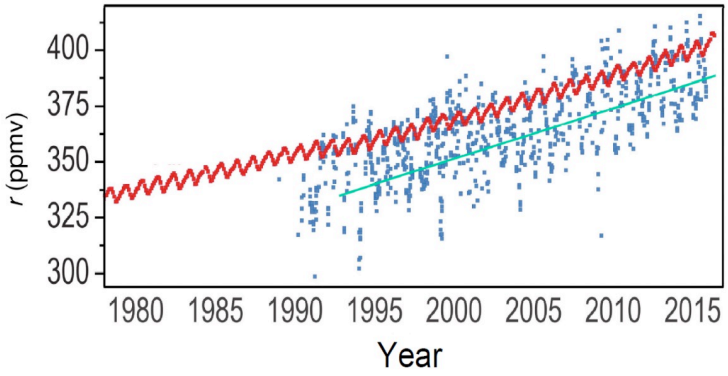

Figure 4: CO_2 mixing ratio observed at Hawaii in the atmosphere (Red) and ocean (Blue). Source: USGCRP (2017), Fig. 13.4.

The foregoing transition between equilibrium states establishes the sensitivity to temperature of ocean emission:

$$Q_O = \frac{1}{E_O}\frac{\delta E_O}{\delta T} = \frac{\delta \Delta r / \Delta r}{\delta T} \quad , \qquad (20)$$
$$= \frac{1/39}{0.9}\mathrm{K}^{-1} = 0.029\,\mathrm{K}^{-1}$$

About 3%/K, the sensitivity to temperature of ocean emission is much smaller than the sensitivity implied by the initial CO_2 contrast (13 ppmv): $Q_O \cong (13/39)/0.9 \cong 37\%/\mathrm{K}$.

3.2 Terrestrial Tropics: $S_O = 0$

The sharp reduction of perturbation emission by ocean (19) follows from its dependence on the resulting perturbation of atmospheric CO_2. Increased back pressure exerted by the atmosphere (δr_A) reduces the perturbation of the atmosphere-ocean contrast, $\delta \Delta r$, eventually limiting the perturbation in ocean emission to a small fraction of its initial perturbation.

Unlike ocean emission, soil respiration (7) has no such limitation - because R is not determined by the contrast of CO_2 between the atmosphere and surface. Rather, $R = F_L$ is determined by the vertical gradient of CO_2 flux beneath the surface, which is imposed from below by upward diffusion of CO_2-rich air through porous media (Maier et al. 2020). And, because CO_2 partial pressure in soil (r_L) vastly exceeds its partial pressure in the atmosphere, increased r_A has little impact on the CO_2 flux gradient and, hence, on respiration R that determines emission from land.

In the absence of ocean, (10) reduces to

$$\frac{\delta r_A}{r_A} = \frac{\delta R}{R}. \qquad (21)$$

The thermally-induced perturbation of respiration follows from the temperature sensitivity of R (8):

[4] Different to the central tropics the ocean-atmosphere flux at Hawaii is already slightly negative (see also Fig.1).

$$Q_L = \frac{1}{R}\frac{\delta R}{\delta T_L}. \tag{22}$$

In contrast to ocean emission, the accompanying perturbation of land emission (7) is undiminished by increasing atmospheric CO_2; relative to thousands of ppmv in soil, increases of a few tens of ppmv in the atmosphere are immaterial. The limiting perturbation of atmospheric CO_2, δr_A ($t \to \infty$), is therefore controlled autonomously by the initial perturbation of emission from land, which is invariant during the adjustment to the new (i.e., perturbed) equilibrium.

The fractional increase of atmospheric CO_2 follows from (21) and (22) as

$$\frac{\delta r_A}{r_A} = Q_L \cdot \delta T_L. \tag{23.1}$$

For finite temperature perturbation, (22) becomes $dR/dT = Q_L \cdot R$. If $Q_L \cong$ const, soil respiration increases with δT_L exponentially:

$$R(\delta T_L) = R(0) \cdot e^{Q_L \cdot \delta T_L}. \tag{23.2}$$

At extra-tropical latitudes, such dependence is, in fact, observed (Lloyd and Taylor 1994; Savage and Davidson 2001). However, at tropical latitudes, the range of temperature is so narrow that deviations from linearity

$$R(\delta T_L) \cong R(0) \cdot \left(1 + Q_L \cdot \delta T_L\right) \tag{23.3}$$

are not observed (see Fig. 5). In tropical forest, observations of soil respiration reveal temperature sensitivity in the range 25-35%/K (Wood et al. 2013; Nottingham et al. 2018; Brechet et al. 2017). Representative is the temperature dependence in Fig. 5, which reflects the temperature sensitivity of land emission:

$$Q_L \cong 0.32\,\mathrm{K}^{-1} >> Q_O \tag{23.4}$$

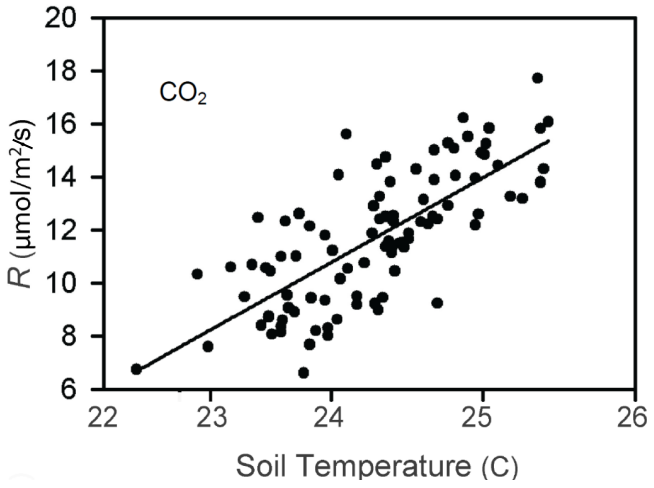

Figure 5: Temperature dependence of soil respiration observed in tropical forest. After Wood et al. (2013).

Measurements of R in Fig. 5 were conducted in Puerto Rico, which lies at the fringe of the tropics. However, biomass, through which soil respiration operates, is concentrated in the deep tropics: the Congo, Amazon basin, and the maritime continent in the western Pacific (Fig. 6). Although measurements are unavailable, temperature sensitivity there may be substantially greater.

The observed perturbation of tropical temperature during the Mauna Loa era (14.2) is represented in the record of SSTA at latitudes $|\phi| < 20°$ (see Fig. 2). It describes the temperature of ocean surface in the tropics. Satellite measurements by the Microwave Sounding Unit (MSU) suite of

instruments sample temperature over both ocean and land. The MSU record of tropical ocean is strongly coherent with the surface record of anomalous SST, but slightly reduced because the MSU record represents atmospheric temperature a couple of km above the surface. Much the same holds for the systematic increase of MSU temperature over tropical landmass (a trend of +0.16 K/decade) vs. over tropical ocean (a trend of +0.12 K/decade). Scaling the perturbation of ocean temperature in (14.2) accordingly provides perturbation temperature that is representative of tropical land:

$$\delta T_L = 1.2\,\mathrm{K} \tag{24}$$

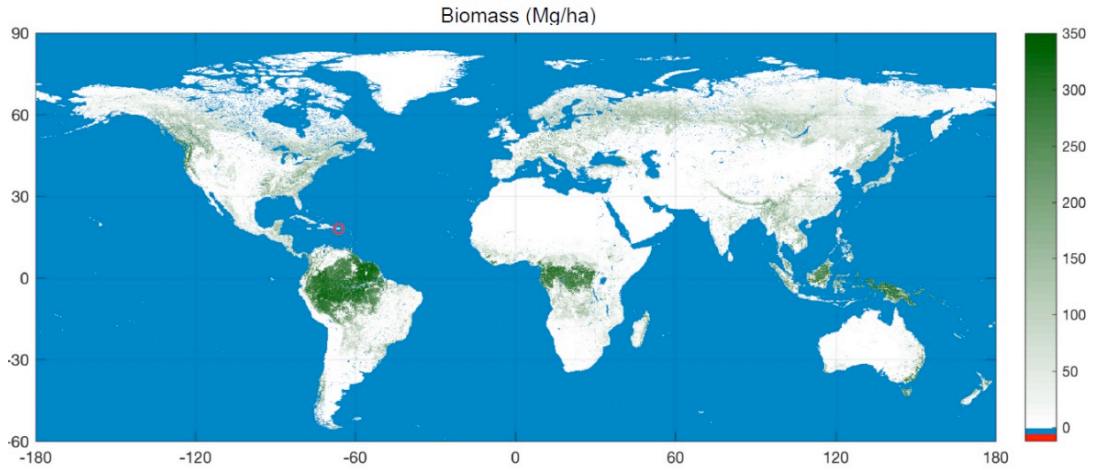

Figure 6: Global distribution of above-ground biomass (Mg/ha), derived from satellite observations. Highlighted is Puerto Rico (Red), the measurement site of soil respiration in the tropics (Fig. 5). Source: European Space Agency.

This temperature perturbation increases land emission (7), which in turn increases atmospheric CO_2. The fractional increase of r_A follows from (23):

$$\frac{\delta r_A}{r_A} \cong 0.39\cdot \tag{25.1}$$

From initial CO_2 of r_A = 315 ppmv (16.4), atmospheric CO_2 thus experiences a thermally induced increase of

$$\delta r_A \cong 122\,\mathrm{ppmv}\cdot \tag{25.2}$$

This corresponds to ending CO_2 in 2020 of

$$\delta r_A \cong 437\,\mathrm{ppmv}\cdot \tag{25.3}$$

3.3 Aqua and Terrestrial Tropics

The presence of both ocean and land couples emission from ocean to emission from land. The perturbation of ocean emission depends upon the perturbation of atmospheric CO_2, which in turn depends upon the perturbation of land emission.

From (10), the fractional increase of atmospheric CO_2 may be expressed

$$\frac{\delta E_O + \delta E_L}{E_O + E_L} = \frac{\delta r_A}{r_A}. \tag{26}$$

Although differing in surface area, tropical ocean and land have comparable total emission. According to marine observations of Δr (Takahashi 1997; Feely et al. 2001) and satellite observations of CO_2 over tropical land (Palmer et al. 2019), emission from tropical ocean and land surface lie in the range

$$0.63E_O < E_L < 4.57E_O. \tag{27}$$

With (26), it follows (Appendix A) that the fractional increase of atmospheric CO_2 must lie in the range:

$$0.15 < \frac{\delta r_A}{r_A} < 0.34. \tag{28}$$

The thermally-induced increase of atmospheric CO_2, collectively from tropical ocean and land, must therefore lie in the range

$$47\,\text{ppmv} < \delta r_A < 107\,\text{ppmv}. \tag{29.1}$$

This range of fractional increase corresponds to ending CO_2 during 2020 in the range

$$362\,\text{ppmv} < r_A < 422\,\text{ppmv}. \tag{29.2}$$

Observed CO_2 during 2020 was ~ 414 ppmv.

4. Response to Observed Warming

Over much of the Earth, evidence of a systematic and sustained change of temperature is scarce (SH2). What warming has occurred during the Mauna Loa era occurred sporadically, incoherent in time. At mid-latitudes, the MSU record reveals no systematic change. At polar latitudes, where a trend is evident, MSU retrievals are vulnerable to ice, snow, and high terrain, features that are prevalent at polar latitudes (see, e.g., Maslanic 2007; Wang et al. 2017; Cui et al. 2020; Swanson 2003).

In contrast, temperature in the tropics has increased systematically (Fig. 2). Evident in the records of both MSU and SSTA, this systematic warming is free of the uncertainty that surrounds microwave retrievals at polar latitudes. According to the development in Sec. 3, the systematic warming of tropical ocean and land surface must be attended by intensified net emission of CO_2. In fact, it is (SH2). Intensified net emission, in turn, must induce a drift in global equilibrium, with an attendant increase of CO_2.

Investigating the thermally-induced perturbation of CO_2 requires a record of tropical temperature that extends back to 1959, when Mauna Loa measurements began. Over ocean, this requirement is met by the record of SSTA (Fig. 2), albeit with limited accuracy before the advent of global coverage by satellites. Over tropical land, no such record is available. There, we must also rely on SSTA.

Ocean temperature is less coherent with the observed record of net CO_2 emission than is land temperature (ibid). Nevertheless, it is strongly coherent with land temperature, which is largely imposed by surrounding ocean. The strong interdependence of land and ocean temperature is evidenced during the satellite era, when there is complete coverage of the tropics. The two then vary co-dependently, achieving a correlation of 0.94. Despite the limitation of coverage, SSTA is the only means by which tropical temperature can be extended back to the onset of Mauna Loa measurements. Mindful of the limitations, we employ the record of SSTA to explore the thermally-induced perturbation of CO_2, which can then be compared against the observed evolution of CO_2. From (10), the fractional perturbation of emission equals the fractional perturbation of atmospheric CO_2. Hence,

$$\delta E = E\frac{\delta r_A}{r_A}, \tag{30.1}$$

where the perturbation of emission has contributions from ocean and land:

$$\delta E = E_O \cdot Q_O \cdot \delta T_O + E_L \cdot Q_L \cdot \delta T_L, \tag{30.2}$$

Then

$$\frac{\delta E}{E} = \frac{E_O \cdot Q_O \cdot \delta T_O + E_L \cdot Q_L \cdot \delta T_L}{E_O + E_L} = \frac{E_O (Q_O \cdot \delta T_O + \gamma \cdot Q_L \cdot \delta T_L)}{E_O (1+\gamma)}, \tag{31.1}$$

where

$$\gamma = \frac{E_L}{E_O} \tag{31.2}$$

represents the relative emission from tropical land and ocean (27). The fractional perturbation of emission then becomes

$$\frac{\delta E}{E} = \frac{Q_O \cdot \delta T_O + \gamma \cdot Q_L \cdot \delta T_L}{1+\gamma}. \tag{32}$$

Owing to the strong interdependence of temperature over tropical land and ocean, temperature over land can be expressed in terms of temperature over ocean. Proceeding as in Sec. 3.2, (24) obtains

$$T_L \cong (0.16/0.12) T_O = 1.33 T_O \cdot \tag{33}$$

The fractional perturbation of emission (32) then reduces to

$$\frac{\delta E}{E} = \frac{Q_O + 1.33 \cdot \gamma \cdot Q_L}{1+\gamma} \delta T = \overline{Q} \cdot \delta T, \tag{34.1}$$

where

$$\overline{Q} = \frac{Q_O + 1.33 \cdot \gamma \cdot Q_L}{1+\gamma} \tag{34.2}$$

represents the effective temperature sensitivity of tropical surface, collectively from ocean and land, and T is understood hereafter to refer to T_O .

For finite temperature perturbation and integration of (34.1) obtains the perturbation of overall emission from the tropics in terms of anomalous temperature of tropical ocean:

$$E(\delta T) = E(0) \cdot e^{\overline{Q} \cdot \delta T}, \tag{35}$$

where $E(0)$ is CO_2 emission in the unperturbed equilibrium state and δT is the departure of temperature from that state.

Anomalous emission in (35) describes the temperature-dependent part. Total emission is then

$$E = E_0 + \hat{E}(\delta T), \tag{36}$$

with E_0 representing emission that is not temperature dependent and $\hat{E}(\delta T)$ given by (35). Time-varying net emission, $\hat{E}(\delta T(t))$, can be evaluated over the Mauna Loa era from the contemporaneous record of SSTA: $\delta T(t)$.

4.1 Constant Effective Absorption

We are interested in determining E_{net} , the component of emission that controls anomalous CO_2. The conservation law (1) defines net emission,

$$E_{net} = E - \alpha_{eff} \cdot r_A, \tag{37.1}$$

which determines anomalous CO_2 through

$$E_{net} = \frac{dr_A}{dt}. \tag{37.2}$$

For constant α_{eff}, differentiating (37.1) obtains the balance governing net emission of CO_2:

$$\frac{dE_{net}}{dt} + \alpha_{eff} E_{net} = \frac{dE}{dt}. \tag{38}$$

Equation (38) can be solved analytically. Incorporating an integrating factor yields its solution:

$$E_{net}(t) = \left[E_{net}(0) - \hat{E}(0)\right] e^{-\alpha t} + \hat{E}(t) - \alpha e^{-\alpha t} \int_0^t e^{\alpha t'} \hat{E}(t')\, dt', \tag{39.1}$$

wherein initial conditions are embodied in the term in brackets, α represents α_{eff}, and

$$\hat{E}(t) = \hat{E}(0) \cdot e^{\overline{Q} \cdot \delta T(t)}. \tag{39.2}$$

Although restricted to α = const, an analytical solution of E_{net} affords insight that is not available from a numerical solution. For times long compared to the effective absorption time ($t >> \alpha^{-1}$), net emission reduces to the limiting form

$$E_{net}(t) \sim \hat{E}(t) - \alpha e^{-\alpha t} \int_0^t e^{\alpha t'} \hat{E}(t')\, dt'. \tag{40}$$

Therein, net emission of CO_2 follows from a competition between temperature-induced emission, embodied in the first term on the right-hand side, and absorption of the resulting CO_2, embodied in the second term. In the latter, absorption discriminates according to the time scale of emission, through the exponential kernel of the integral in (40). Fluctuations of $\hat{E}$ on time scales shorter than α^{-1} experience strong cancellation in the integral. Thereby, those components are suppressed in the absorption term, leaving them largely undamped. If, however, α also discriminates according to time scale, as will emerge in Sec. 4.2, then short time scales can nevertheless experience strong absorption.

Notice: If the perturbation of temperature is invariant, δT= const,

$$\begin{aligned} E_{net}(t) &= \hat{E}(0) e^{\overline{Q} \cdot \delta T} - \alpha \hat{E}(0) e^{\overline{Q} \cdot \delta T} e^{-\alpha t} \int_0^t e^{\alpha t'} dt' \\ &= \hat{E}(0) e^{\overline{Q} \cdot \delta T} - \alpha \hat{E}(0) e^{\overline{Q} \cdot \delta T} \cdot \frac{1 - e^{-\alpha t}}{\alpha} \quad , \\ &\sim 0 \qquad\qquad \text{for } t >> \alpha^{-1} \end{aligned} \tag{41}$$

Irrespective of how large the temperature perturbation is, net emission eventually vanishes - because anomalous CO_2 eventually increases enough to restore the system to equilibrium. The same holds for any constant perturbation of emission (e.g., anthropogenic emission, were it to remain constant). It follows that, under these conditions, CO_2 cannot accumulate in the atmosphere indefinitely. Net emission can remain nonzero and, hence, continue to change CO_2, only if emission continues to change.

Because the global system remains in a state of quasi-equilibrium, wherein emission is largely balanced by absorption (2.1), induced changes of CO_2 must track changes of emission that produce them. These circumstances apply to thermally-induced CO_2, including the component forced by the systematic increase of tropical temperature (Fig. 2).

4.2 Arbitrary Absorption

For $\alpha = \alpha_{eff}$ variable, as emerges from the record of nuclear-perturbed carbon 14 (Harde and Salby 2021; SH1), differentiating (37) leads to the more general balance that governs net emission:

$$\frac{dE_{net}}{dt} = \frac{dE}{dt} - \alpha E_{net} - \frac{d\alpha}{dt} r_A. \tag{42}$$

With (36) and (37.2), this can be rearranged into

$$E_{net}(t) = \frac{1}{\alpha}\left[\frac{d\hat{E}}{dt} - \frac{dE_{net}}{dt}\right] - \frac{d\ln\alpha}{dt}\int_0^t E_{net}(t')\,dt' \cdot \tag{43}$$

Governing net emission under conditions of arbitrary absorption, the balance (43) is an integro-differential equation of the Volterra class (Goltser and Litsyn 2005).

Anomalous surface temperature (Fig. 2) and, hence, thermally-induced emission (35) involve two spectral components of disparate time scales: (i) interannual fluctuations, with periods of a couple of years, and (ii) the systematic increase of temperature, with periods much longer than a decade. Because their time scales are widely separated, those spectral components correspond to high- and low-pass filtered forms of δT. Through (35), they introduce similar components into thermally-induced emission:

$$\hat{E}(t) = \hat{E}_{LP}(t) + \hat{E}_{HP}(t) \cdot \tag{44}$$

Anomalous CO_2 produced by these spectral components of emission experiences different effective absorption, which depends upon time scale.

As developed in SH1, effective absorption of CO_2 is modulated by its re-emission from the Earth's surface. By offsetting direct absorption, re-emission slows effective absorption of CO_2. For short time scales (e.g., induced by interannual fluctuations of δT), re-emission has little time to intensify before δT reverses. Direct absorption of CO_2 then experiences little offset, leaving α_{eff} fast. However, for long time scales (e.g., induced by the systematic increase of δT), re-emission has ample time to intensify. Direct absorption of CO_2 then experiences a large offset, which renders α_{eff} slow.

The dependence on time scale is manifest in the response of CO_2 to $\hat{E}_{LP}$ and $\hat{E}_{HP}$. An oscillatory perturbation of temperature

$$\delta T = \mathrm{T}\ e^{-i\omega t} \tag{45.1}$$

and thus of emission

$$\delta E = \mathrm{E}\, e^{-i\omega t} \tag{45.2}$$

is introduced in the 3-volume system of SH1, a system that reproduces the observed evolution of nuclear-perturbed carbon 14 in the same way as seasonal oscillations. Through Fourier transform, spectral components of the form (45) comprise the LP and HP components of δT and, thereby, the respective components of thermally-induced emission, $\hat{E}_{LP}$ and $\hat{E}_{HP}$. For specified ω, the perturbation $\delta\mathrm{E}$ introduces an oscillatory perturbation in atmospheric CO_2. The amplitude of anomalous CO_2 measures effective absorption of that spectral component.

Anomalous tropospheric CO_2 in the 3-volume system (viz. r_A) is coupled to anomalous CO_2 in the surface layer and in the stratosphere through exchanges of carbon. Nevertheless, r_A still obeys the conservation law (1), which may be expressed abstractly

$$\frac{dr_A}{dt} + \alpha_{eff}\, r_A = F, \tag{46}$$

where the forcing operator F includes perturbation emission of CO_2, as well as exchanges of CO_2 between the troposphere, surface layer and stratosphere. Letting

$$\begin{aligned} F &= \mathrm{F}\ e^{-i\omega t} \\ r_A &= \mathrm{R}\, e^{-i\omega t} \end{aligned} \tag{47.1}$$

transforms (46) into

$$-i\omega\mathrm{R} + \alpha_{eff}\,\mathrm{R} = \mathrm{F}\ . \tag{47.2}$$

Anomalous CO_2 induced by the perturbation of emission (45.2) thus oscillates with the complex amplitude

$$\mathrm{R} = \frac{\mathrm{F}}{-i\omega + \alpha_{eff}} \cdot \tag{48}$$

The perturbation of tropospheric CO_2 has the limiting form

$$\mathrm{R} \sim \begin{cases} \dfrac{\mathrm{F}}{-i\omega} = \dfrac{\mathrm{F}}{\omega} e^{i\pi/2} & \omega/\alpha_{eff} \to \infty \\ \dfrac{\mathrm{F}}{\alpha_{eff}} & \omega/\alpha_{eff} \to 0 \end{cases} . \tag{49}$$

Short time scales ($\omega \to \infty$) are introduced by $\hat{E}_{HP}$ (44). Anomalous CO_2 then becomes small and oscillates *in quadrature* with thermally-induced emission. In this limit, the troposphere and surface layer are out of equilibrium: CO_2 in one never equals that in the other. Re-emission from the Earth's surface is therefore weak. Consequently, it provides little offset to direct absorption, leaving α_{eff} fast.

Long time scales ($\omega \to 0$) are introduced by $\hat{E}_{LP}$. Anomalous CO_2 then oscillates *in phase* with thermally-induced emission. In this limit, the troposphere and surface layer have time to attain quasi-equilibrium, with CO_2 in one nearly equal to that in the other. Re-emission has then intensified. It offsets much of direct absorption, rendering α_{eff} slow.

Rearrangement of (48) obtains the effective absorption rate in terms of the amplitude of the spectral component with frequency ω:

$$\alpha_{eff}^2 = \frac{|\mathrm{F}|^2}{|\mathrm{R}|^2} - \omega^2 \cdot \tag{50}$$

Note: Since R scales directly with F, α_{eff} is independent of the forcing amplitude. Without loss of generality, F may therefore be set equal to 1 ppmv/yr.

Plotted in Fig. 7 is anomalous CO_2 that is induced by the spectral component of F with a period $2\pi/\omega = 2000$ yrs (Blue), which is inherent to the long-term increase in Fig. 2. Anomalous r_A that it produces is seen to vary in phase with its forcing, $F_{Re} = Re\{\mathrm{F}\, e^{-i\omega t}\} \sim \cos(\omega t)$. Related to $|\mathrm{F}|$ it has an amplitude of 9.6 ppmv. According to (50), the LP component of anomalous CO_2 therefore experiences effective absorption

$$\alpha_{eff}^{LP} \cong 0.104\ yr^{-1}, \tag{51.1}$$

or an effective absorption time $\tau_{eff} = 9.6$ yr in full agreement with Harde and Salby 2021 and SH1.

Also plotted in Fig. 7 is anomalous CO_2 that is induced by the spectral component of F with a period 2.8 yrs (Red), equal to the mean period of interannual fluctuations in Fig. 2. It is inherent to the HP component of thermally-induced emission. Despite being forced by the same amplitude in the same system, anomalous CO_2 introduced by the HP component of emission achieves an amplitude of only 0.37 ppmv. According to (50), it experiences effective absorption

$$\alpha_{eff}^{HP} \cong 1.51\ yr^{-1}, \tag{51.2}$$

corresponding to an effective absorption time of less than a year.

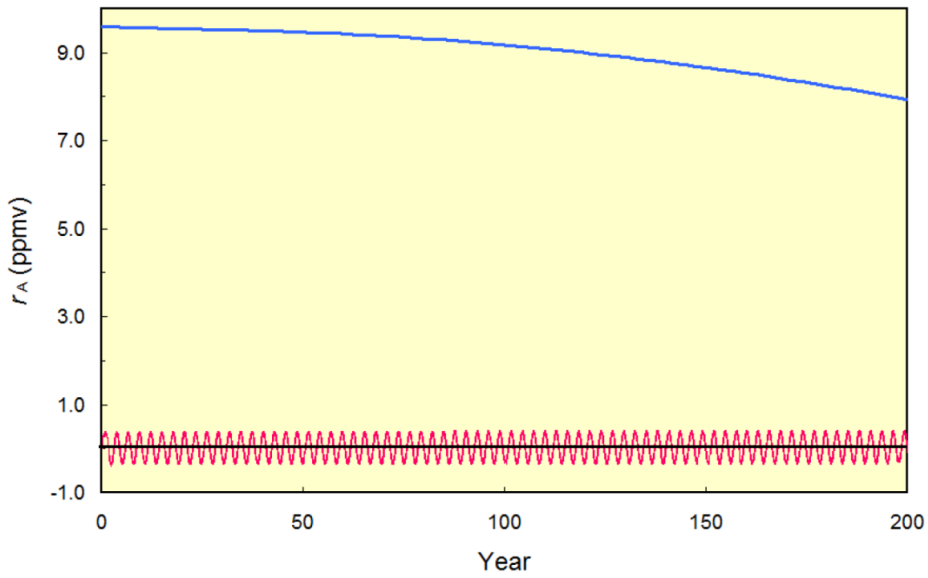

Figure 7: Response of tropospheric CO_2 to harmonic surface emission with a period of 2000 yrs (Blue) and a period of 2.8 yrs (Red), equal to the mean period of interannual fluctuations of net emission in the observed record: see text.

It is noteworthy that absorption of the HP component of anomalous CO_2 can also be deduced empirically. Interannual fluctuations of CO_2 are observed to operate coherently with but lag interannual fluctuations of temperature (Humlum et al. 2013; Salby 2013; Harde 2019). Independent of the above analysis, the observed lag reveals effective absorption of $\alpha_{eff}^{HP} \cong 1.35\ yr^{-1}$.[5]

The governing balance (43) is now solved numerically for thermally-induced net emission, $E_{net}(\delta T)$, through 4th order Runge-Kutta treatment. With $\hat{E}(t)$ prescribed through SSTA (39.2), anomalous temperature (Fig. 2) is filtered to periods longer and shorter than two decades, thereby discriminating between the LP and HP components of δT. Anomalous CO_2 introduced by the respective components of thermally-induced emission (39.2) is subjected to effective absorption in (51), which is varied weakly according to observed α_{eff} (SH1). Representative of the effective temperature sensitivity of tropical surface (34) is $\overline{Q} = 0.30\ K^{-1}$ (Fig. 5).[6] The corresponding value of γ in (31.2) is 2.7. It falls squarely within the observed range of emission inferred from observations (27).

Plotted in Fig. 8 is thermally-induced net emission (Blue). Despite having several hundred observations, of order a hundred independent degrees of freedom, $E_{net}(T)$ tracks the observed record of E_{net} (Red). The correspondence holds for interannual fluctuations of net emission, notably during the El Niños of 1973, 1997, and 2016, as well as for its long-term intensification, wherein E_{net} and $E_{net}(\delta T)$ intensify from ~ 0.7 ppmv/yr to almost 2.5 ppmv/yr. Notice that, before the El Niño of 1973, observed net emission remains approximately level: E_{net} undergoes no systematic change until after that El Niño. Thermally-induced net emission, $E_{net}(\delta T)$, undergoes the same transformation; cf. Fig. 2. With a correlation of 0.78, the two records in Fig. 8 are strongly interdependent. Their correlation is, in fact, quite close to the correlation between observed E_{net} and thermally-induced emission that is deduced empirically (SH2).

---

[5] Consistent with both analyses is the observed annual cycle of emission from tropical land in the Northern Hemisphere, where its annual cycle is strongest (Palmer 2019). It varies nearly in phase with the annual cycle of CO_2. According to (49), this HP component of CO_2 must therefore experience effective absorption shorter than a year.

[6] In light of the paucity of measurements in the deep tropics, where biomass is concentrated, this value may well underestimate the actual temperature sensitivity.

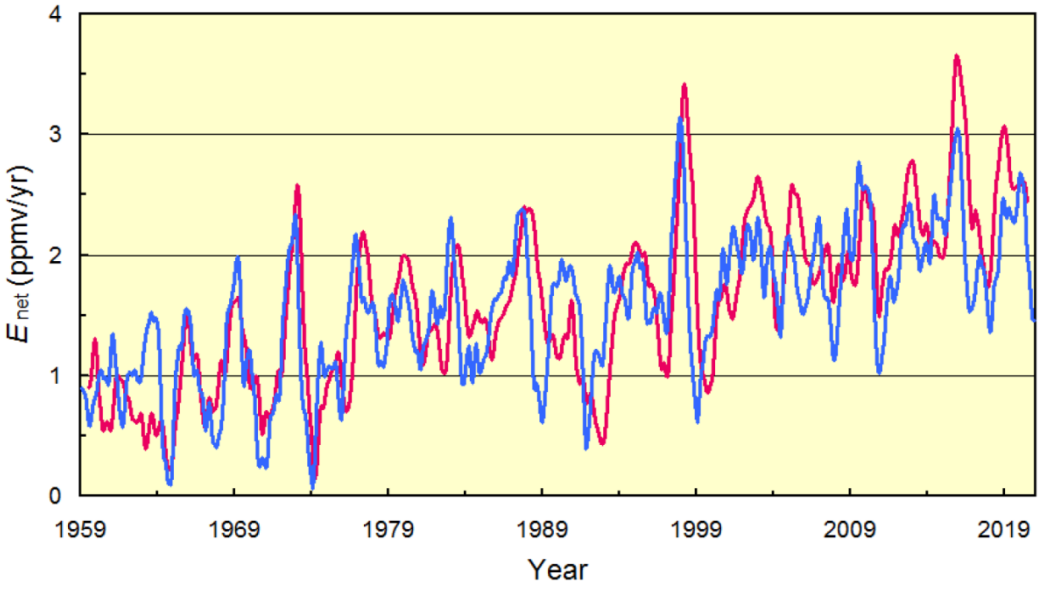

Figure 8: Net CO_2 emission observed (Red), low-pass filtered to periods longer than a year, along with its thermally-induced component (Blue), calculated from the observed record of tropical temperature.

Subject to the same physical processes is anthropogenic emission, E^{Ant}, which is plotted in Fig. 9. It, too, must obey the governing balance (43), with E^{Ant} in place of $\hat{E}$. There is, however, an important distinction. Unlike thermally-induced emission from the surface, anthropogenic emission operates directly in the atmosphere. For re-emission of CO_2 to amplify and slow effective absorption of CO_2, anthropogenic emission must enrich CO_2 in the surface layer relative to that in the atmosphere. As detailed in SH1, the continuous re-supply of anomalous CO_2 in the atmosphere maintains the troposphere and surface layer out of equilibrium. Thereby, it limits re-emission and its offset of direct absorption, leaving α_{eff} fast.

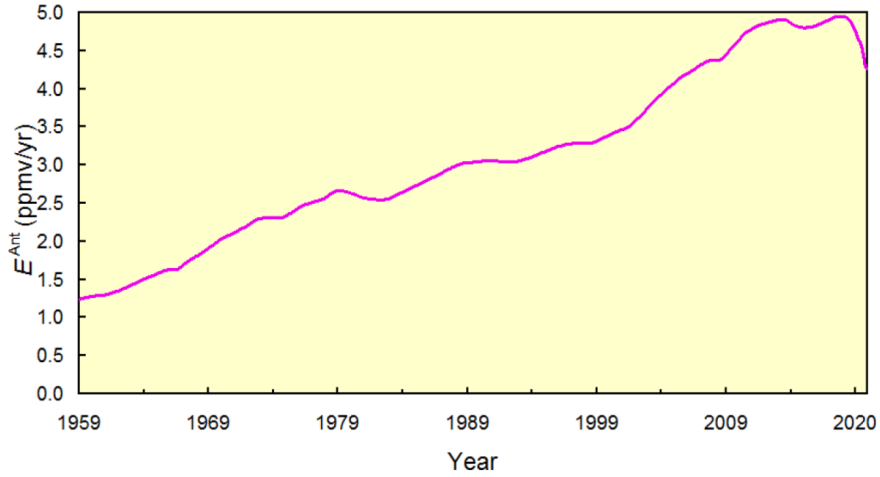

Figure 9: Global anthropogenic emission of CO_2. Sourced from CDIAC (2017) and Le Quéré et al. (2021).

The 3-volume system of Fig. 7 is now perturbed by atmospheric emission with a period of 2000 yrs, characteristic of the long-term increase of anthropogenic emission (Fig. 9). Anomalous CO_2 (not shown) evolves similarly to the LP spectral component in Fig. 7, which results from surface emission. However, forced by emission in the atmosphere, r_A now achieves an amplitude of only 1.105 ppmv. From (50), anomalous CO_2 therefore experiences effective absorption of

$$\alpha_{eff}^{Ant} \cong 0.91 \ yr^{-1}, \tag{51.3}$$

corresponding to an effective absorption time of about a year. Much the same effective absorption is found for monotonically-increasing anthropogenic emission (SH1).

Plotted in Fig. 10 is net emission (43) that follows from anthropogenic emission, E_{net}^{Ant}(Magenta, Lower Graph). Owing to rapid absorption, anthropogenic CO_2 is removed almost as fast as it is introduced. Consequently, $E_{net}^{Ant}$is only a few tenths of a ppmv/yr, an order of magnitude weaker than net emission from the Earth's surface that is thermally-induced, $E_{net}(\delta T)$; cf Fig. 8.

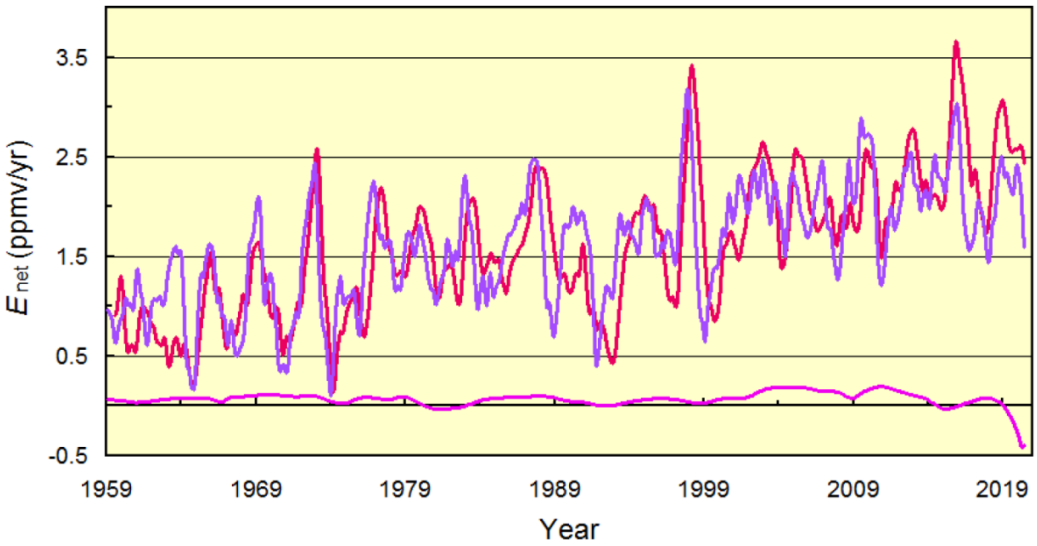

Figure 10: Net CO_2 emission observed (Red), along with the total calculated net emission, comprised of thermally-induced and anthropogenic components (Purple). Plotted separately is the anthropogenic component alone (Magenta, Lower Graph).

Superimposed in Fig. 10 is total net emission: $E_{net} = E_{net}(\delta T) + E_{net}^{Ant}$(Purple). It tracks the observed record of net emission (Red). Total net emission follows almost entirely from the thermally-induced component (Fig. 8). Relative to mean net emission observed during the Mauna Loa era, the thermally-induced component represents 95.9%. The anthropogenic component represents 4.1%. Almost the same is expected from the natural to anthropogenic emission ratio.

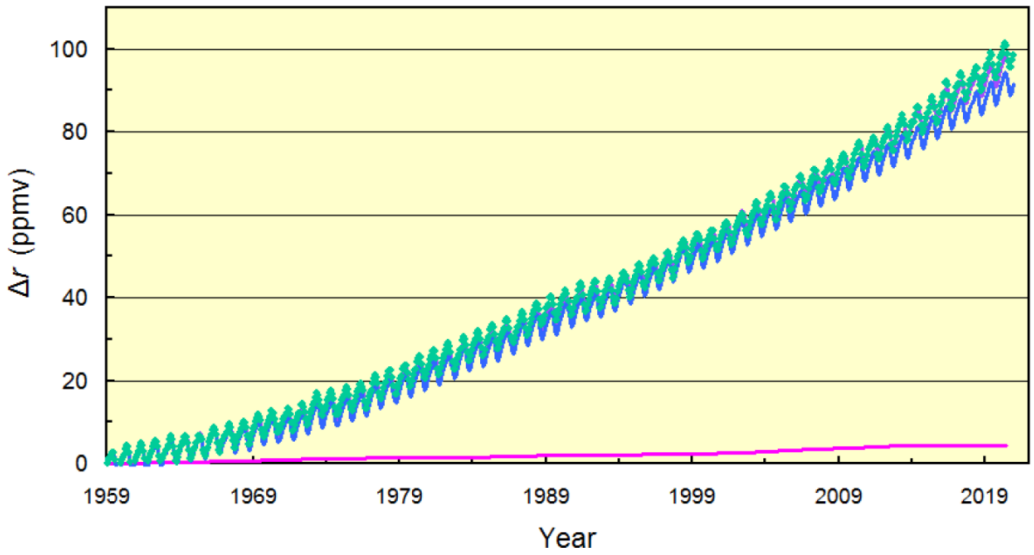

Figure 11: Observed increase of CO_2 (Green), compared against the calculated increase (Purple). Note: Calculated CO_2 lies mostly beneath observed CO_2, but emerges near the end of the record. Plotted separately is the contribution from thermally-induced emission (Blue) and the contribution from anthropogenic emission (Magenta).

In Fig. 11 is displayed the observed increase of r_A (Green). Superimposed is anomalous CO_2 (37.2) that is forced by the total emission in Fig. 10 (Purple - almost completely covered by the Green graph). It closely tracks the observed evolution of anomalous CO_2. Tracking observed CO_2 almost as closely is the thermally-induced component of anomalous CO_2 (Blue). Also superimposed in Fig. 11 is the anthropogenic component of anomalous CO_2 (Magenta). Comparatively small, it tracks the instantaneous equilibrium level of anthropogenic CO_2 (Sec. 1) (see also Harde 2019, Figs 8 and 10; and SH1, Fig 14).

In this context we note that from estimates of the anthropogenic emission rate E^{Ant} and the observed increase $\Delta r_A/\Delta t$ of the atmospheric mixing ratio within one year, it is widely inferred that about 44% of these emissions (or an equivalent mass) as so-called Airborne Fraction AF remains in the atmosphere, while the rest is absorbed by extraneous reservoirs (Sixth Assessment Report (AR6), 2021, Chap. 5, Fig 5.7). Therefore, nature is assumed to be a net sink, and not natural but almost exclusively anthropogenic sources are made responsible for the increasing atmospheric CO_2.

However, this interpretation neglects that changes in the mixing ratio, which are initiated in a linearly responding system, cannot be greater than the perturbation, and these changes are responding with some delay to the emissions, determined by the effective absorption time τ_{eff}. So, comparing the growth rate $\Delta r_A/\Delta t$ of the mixing ratio with an additional emission ΔE, native or anthropogenic, it is obvious that $\Delta r_A/\Delta t < \Delta E$, until new equilibrium or quasi-equilibrium can establish with $\Delta r_A^{eq} = \Delta E \cdot \tau_{eff}$. But by far this does not mean that nature would be a net sink and could not contribute on its own to an increasing mixing ratio (see Appendix B).

For a more detailed discussion of the different paradigms of native or anthropogenic contributions to the CO_2 mixing ratio in the atmosphere, see also Connolly et al. 2020.

5. Methane Emission

Like carbon dioxide emission, CH_4 emission increases with temperature (Fig. 12). Methane has likewise been systematically increasing, albeit in an observed record that is much shorter than the Mauna Loa record of CO_2. It too is emitted by biomass (Fig. 6), chiefly through anaerobic processes that operate in well-irrigated regions like wetlands. Owing to its production in aqueous environments, however, methane emission is also dependent upon precipitation, which is plotted in Fig. 13a. It mirrors the observed distribution of methane, presented in Fig. 13b. Accordingly, those influences magnify CH_4 emission from tropical land, where biomass and precipitation are abundant (Pangala et al. 2017; Lunt et al. 2019; Gauci et al. 2021).

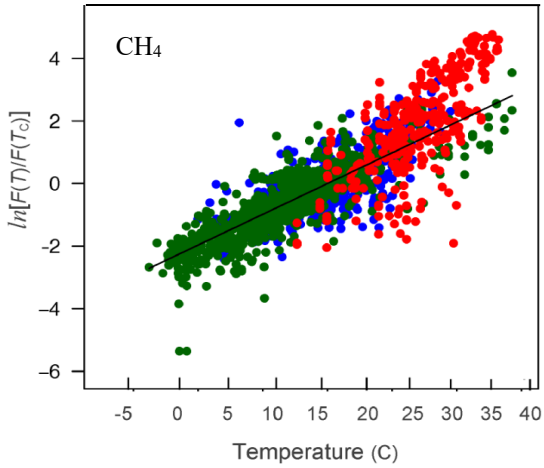

Figure 12: Observed temperature dependence of methane emission in wetland (Green), aquatic (Blue), and rice paddy (Red) environments. F is the production rate of CH_4, analogous to respiration, in Arrhenius exponential form of temperature dependence. After Durocher et al. (2014).

The popularized view of the simultaneous increase of carbon dioxide and methane, namely, that it is the result of humans, is paradoxical. Promulgated by the UN's IPCC, this view holds that their joint increase follows, purportedly, from anthropogenic sources, even though anthropogenic sources of CO_2 and CH_4 are physically independent.

In contrast, the simultaneous intensification of CO_2 emission and CH_4 emission is precisely what must accompany observed warming in the tropics. Evidenced here in observed behavior, this single physical mechanism provides a unified understanding of the joint increase of these greenhouse gases, one that follows naturally from thermally-induced emission.

In this context we have to point to an often found misinterpretation concerning the global warming potential of methane. So, the radiative efficiency of CH_4 with $3.7x10^{-4}$ W/m^2/ppbv is classified to be 25x larger than that of CO_2 with $1.4x10^{-5}$ W/m^2/ppbv. Such values are derived from the changing absorptivity or emissivity of the gases, when their concentration is changing by 1 ppbv. But these radiative efficiencies compare the two gases under completely different conditions: CH_4 at a concentration of 1.8 ppmv and CO_2 at a 200x larger concentration, when it is already strongly saturated. Also, the interference with other greenhouse gases, particularly with water vapor, is for both gases completely different.

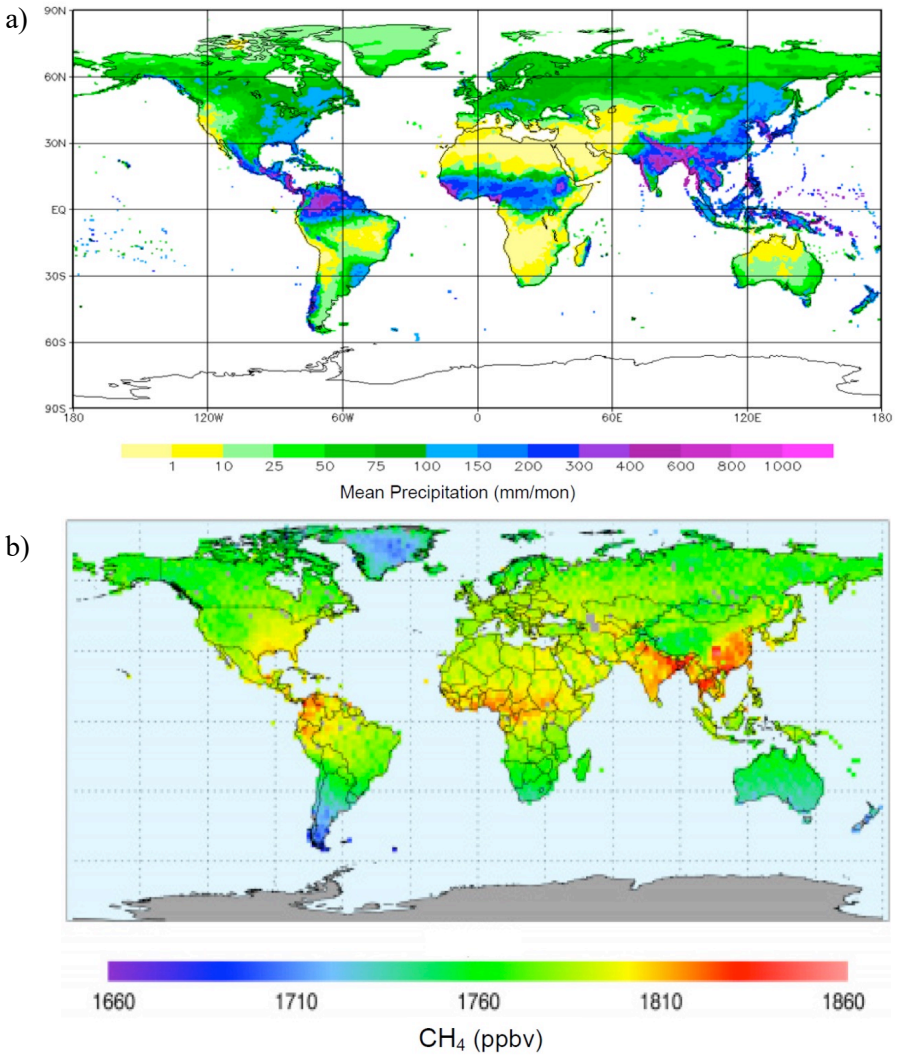

Figure 13: a) Mean global distribution of precipitation in July. Source: GPCC (2020).
b) Mean global distribution of methane, observed by satellite. Source: ESA (2017).

Only these diverse conditions pretend a much higher radiative efficiency of methane, respectively a considerably lower value for CO_2. So, at a comparable concentration of 400

ppmv for CH_4 in the atmosphere the radiative efficiency drops to about 65% of CO_2, and at a concentration of only 1.8 ppmv of CO_2 the efficiency is about 1.5 times larger than that of CH_4 (see also Wijngaarden and Happer 2019). Only due to the different saturation strengths on quite different scales is CH_4 assumed to have a 25x larger global warming potential, while a more realistic consideration supposing a doubling each of the actual CH_4 and CO_2 concentrations shows that CH_4 does not contribute more than about 2% to global warming relative to CO_2 (Harde 2021).

6. Conclusion

Thermally-induced emission in the tropics closely tracks observed net emission of CO_2. It thus accounts for the preponderance of CO_2 net emission, which in turn determines anomalous CO_2. For this reason, the thermally-induced response to observed warming in the tropics represents nearly all of the observed increase of atmospheric CO_2.

The geographical site of net emission is noteworthy. Through the conservation law, the strong correspondence to observed net emission follows theoretically from behavior in the tropics - not in the extratropics, where anthropogenic emission is concentrated. Independently, the same correspondence to observed E_{net} follows empirically from anomalous temperature in the tropics (SH2), as well as from a time-lag analysis of anomalous CO_2 (Humlum et al. 2013). Especially noteworthy is that, in the time-lag analysis, strong coupling of anomalous CO_2 appears initially in the tropics, but then advances poleward into each hemisphere.

In both theoretical and empirical evaluations, thermally-induced emission of CO_2 represents interannual intensifications of net emission, notably during episodes of El Niño. Represented equally well is the long-term intensification of net emission during the last half century. The strong correspondence to observed changes indicates that, although operating on disparate time scales, both unsteady components of CO_2 net emission share the same physical mechanism.

Long-term intensification of E_{net} is manifest in both the observed and calculated records. It accounts for about half of the observed increase of atmospheric CO_2 (SH2). Owing to the fundamental sensitivity to temperature of surface flux (Fig. 5), such intensification is an inevitable consequence of systematic warming in the tropics.

In relation to CO_2, what is responsible for that warming is immaterial. Its influence on CO_2 should not be confused through circular reasoning. The observed warming, which forces increased CO_2 through intensified net emission, cannot itself be the result of increased CO_2. Were it, anomalous CO_2 and net emission that forces it would have increased twice as much as was observed: (i) the increase required to produce the observed warming plus (ii) the thermally-induced response to that warming, which, irrespective of what caused the warming, induces an intensification of net emission that is nearly identical to what is observed. For a detailed consideration of the "hen-or-egg causality" see also Koutsoyiannis & Kundzewicz

That net emission of CO_2 is not the cause of but the response to changes of temperature is also clear from their robust coherence, which is observed *on all time scales* (SH2). Likewise, for their in-phase relationship. Simultaneous changes of tropical temperature and net emission of CO_2 are inherent to their long-term increase as well as to interannual fluctuations, which arise unambiguously from natural changes of surface temperature. Anthropogenic emission, on the other hand, could introduce only long-term changes but not the observed interannual changes - incongruous with the strong coherence that is observed irrespective of time scale.

More fundamentally, causation by anthropogenic emission of CO_2 is eliminated by the observed *in-phase* relationship between E_{net} and tropical temperature. Simultaneous changes in those properties contradict the *in-quadrature* relationship they would have were the changes of temperature forced by changes of CO_2 (ibid). The observed in-phase relationship thus establishes unambiguously that net emission of CO_2 is forced by changes of tropical temperature - not vice

versa.

Like carbon dioxide emission, also CH_4 emission increases with temperature (Fig. 12). It too is emitted by biomass (Fig. 6), chiefly through anaerobic processes that operate in well-irrigated regions like wetlands, and those influences magnify CH_4 emission particularly from tropical land, where biomass and precipitation are abundant.

The simultaneous intensification of CO_2 emission and CH_4 emission is precisely what is expected from observed warming in the tropics. Therefore, this single physical mechanism provides a unified understanding of the joint increase of these greenhouse gases, one that follows naturally from thermally-induced emission.

Funding

This research was performed without funding, from government or commercial source.

Editor: Prof. Jan-Erik Solheim, **Guest-Editor**: Prof. Ole Humlum, Reviewers: anonymous

Acknowledgements

The authors had a very stimulating cooperation over almost ten years, molded by many inspiriting discussions and encouragements of late Murry Salby. He was one of the few top experts in atmospheric physics and climate sciences, who had extensively studied the main processes controlling the Earth-Atmosphere System, and who was able to deduce from this the true connections of increasing greenhouse gases and a changing climate. In times that are more determined by pseudo-science than serious climate science we have lost an important voice standing up for the true values in science and research and, even more so, in spite of the great personal attacks and existential impairments he had to bear over recent years. We pay the greatest tribute to the deceased for his extensive scientific work which has contributed to a much deeper understanding of climate processes.

We thank the Chief-Editor Prof. Jan-Erik Solheim and the Guest-Editor Prof. Ole Humlum for their continuous support in the publication process and their valuable comments. We also thank the Reviewers for their additional important suggestions and comments.

Appendix A

Observed Range of Tropical Emission

From (26) and (27), the fractional increase of atmospheric CO_2 must lie in the range:

$$\frac{\delta E_O}{E_O + 4.57\,E_O} + \frac{\delta E_L}{E_L/0.63 + E_L} < \frac{\delta r_A}{r_A} < \frac{\delta E_O}{E_O + 0.63\,E_O} + \frac{\delta E_L}{E_L/4.57 + E_L}, \quad \text{(A1.1)}$$

which reduces to

$$0.18\frac{\delta E_O}{E_O} + 0.39\frac{\delta E_L}{E_L} < \frac{\delta r_A}{r_A} < 0.61\frac{\delta E_O}{E_O} + 0.82\frac{\delta E_L}{E_L}. \quad \text{(A1.2)}$$

In terms of surface properties, this relationship becomes

$$0.18\frac{S_O B(\nu)\cdot\delta\Delta r}{S_O B(\nu)\cdot\Delta r} + 0.39\frac{S_L\delta R}{S_L R} < \frac{\delta r_A}{r_A} < 0.61\frac{S_O B(\nu)\cdot\delta\Delta r}{S_O B(\nu)\cdot\Delta r} + 0.82\frac{S_L\delta R}{S_L R} \quad \text{(A2.1)}$$

or
$$0.18\frac{\delta\Delta r}{\Delta r}+0.39\frac{\delta R}{R}<\frac{\delta r_A}{r_A}<0.61\frac{\delta\Delta r}{\Delta r}+0.82\frac{\delta R}{R}. \tag{A2.2}$$

According to (27), $E_L = S_L F_L$ is comparable to or greater than $E_O = S_O F_O$. On the other hand, coverage of the tropics by ocean exceeds that by land ($S_L < S_O$). It follows from (27) that the areal-mean flux from land must be comparable to or exceed the flux from ocean: $F_L \geq F_O$. Replacing the contribution $S_O F_O$ under exclusively ocean conditions by a greater contribution $S_L F_L$ when land is present, can only increase atmospheric back pressure (δr_A) on the ocean surface. It in turn reduces the CO_2 contrast between the atmosphere and ocean, $\delta\Delta r = \delta r_O - \delta r_A$, below its value under exclusively ocean conditions: $\delta\Delta r|_{S_L=0}$.

Consequently,
$$\frac{\delta\Delta r}{\Delta r}\leq\left.\frac{\delta\Delta r}{\Delta r}\right|_{S_L=0}. \tag{A3.1}$$

From (11),
$$\frac{\delta\Delta r}{\Delta r}=\left.\frac{\delta r_A}{r_A}\right|_{S_L=0}=\frac{12}{315}=0.038. \tag{A3.2}$$

Hence, the right-hand side of the inequality (A4.1) is already quite small. Since $\delta\Delta r/\Delta r$ must remain positive, the fractional increase of CO_2 contrast between the atmosphere and ocean must be confined to the narrow range

$$0<\frac{\delta\Delta r}{\Delta r}<\left.\frac{\delta\Delta r}{\Delta r}\right|_{S_L=0}$$

or
$$0<\frac{\delta\Delta r}{\Delta r}<0.038. \tag{A4.1}$$

Similarly, the fractional increase in respiration follows from (22) - (24) as

$$\frac{\delta R}{R}=0.322\cdot 1.2=0.386. \tag{A4.2}$$

With (A4), (A2) reduces to

$$0.18\cdot 0+0.386\cdot 0.386<\frac{\delta r_A}{r_A}<0.614\cdot 0.038+0.82\cdot 0.386,$$

or finally
$$0.15<\frac{\delta r_A}{r_A}<0.34. \tag{A5}$$

Appendix B

Environment as a Net Sink or Net Emitter?

According to the conservation law (1) changes of the CO_2 mixing ratio r_A are controlled by a competition between the total emission rate E and its removal through an absorption rate A:

$$\frac{dr_A}{dt}=E-A=E-\frac{r_A}{\tau_{eff}}, \tag{B1}$$

where the absorption is proportional to the instantaneous abundance of CO_2 and τ_{eff} is the effective absorption time.

With a constant emission E_0 and a perturbation ΔE, Eq. (B1) can also be expressed in the form:

$$\frac{dr_A}{dt} - \Delta E = E_0 - \frac{r_A}{\tau_{eff}}. \tag{B2}$$

For ΔE as the anthropogenic emission rate, as derived from the CDIAC-data, and with the observed increase of the mixing ratio $\Delta r_A/\Delta t$ over one year at Mauna Loa it is obvious that the net flux, E_0 - A can quite well be assessed without needing to know the absolute magnitudes of E_0 or A, quantities which on their parts are often highly uncertain. It is also evident that in a linearly responding system without some virtual amplification the changes $\Delta r_A/\Delta t$ cannot be greater than the perturbation itself, and that these changes are responding with some delay to the emissions, controlled by the effective absorption time τ_{eff}. So, with the left side of (B2) negative, also the right side is negative, and the environmental uptake $A = r_A/\tau_{eff}$ must be larger than the natural emissions E_0. From this statement, however, often wrong conclusions are derived that the environment must have acted as a net sink throughout the Industrial Era, and thus, nature could not have been the reason for any observed CO_2 increase.

For simplicity considering for a moment a constant perturbation ΔE, native or anthropogenic origin or both, the general solution of (B2) is:

$$r_A(t) = r_A(0) \cdot e^{-t/\tau_{eff}} + (E_0 + \Delta E) \cdot \tau_{eff} \cdot \left(1 - e^{-t/\tau_{eff}}\right), \tag{B3}$$

and with $r_A(0) = E_0 \cdot \tau_{eff}$ as the equilibrium concentration for the constant emission E_0, the excess concentration $\Delta r_A(t) = r_A(t) - r_A(0)$ becomes

$$\Delta r_A(t) = \Delta E \cdot \tau_{eff} \cdot \left(1 - e^{-t/\tau_{eff}}\right). \tag{B4}$$

Assuming an increase of the mixing ratio over one year, as derived from an airborne fraction of AF = 44%, but this growth related to the maximum expected increase at a new equilibrium $\Delta r_A^{eq} = \Delta E \cdot \tau_{eff}$, gives a conditional equation with an upper limit for τ_{eff}:

$$\begin{aligned} 0.44 \cdot \Delta r_A^{eq} &= \Delta E \cdot \tau_{eff} \cdot \left(1 - e^{-1\,yr/\tau_{eff}}\right), \\ 0.44 &= 1 - e^{-1\,yr/\tau_{eff}} \end{aligned} \tag{B5.1}$$

or

$$\tau_{eff} = -\frac{1\,yr}{ln(1 - 0.44)} = 1.72 \text{ yrs}. \tag{B5.2}$$

Relating the 44% increase directly to the emission rate ΔE, also over one year (Δt = 1 yr), in agreement with the definition of the airborne fraction, this gives:

$$\begin{aligned} 0.44 \cdot \Delta E \cdot \Delta t &= \Delta E \cdot \tau_{eff} \cdot \left(1 - e^{-\Delta t/\tau_{eff}}\right) \\ 0.44 \cdot \Delta t &= \tau_{eff} \cdot \left(1 - e^{-\Delta t/\tau_{eff}}\right) \end{aligned} \tag{B5.3}$$

and can be seen as a condition for a lower limit, yielding an effective absorption time of only τ_{eff} = 0.51 yrs, close to the calculations for thermally induced emissions of interannual fluctuations with τ_{eff} = 0.67 yrs (Eq.(51.2)). These rough estimates confirm quite well the independently derived result for anthropogenic absorption (51.3) with τ_{eff} = 1.1 yrs, and they explain, why the airborne fraction is largely independent of the size of a perturbation ΔE.

The preceding considerations make also clear that from a negative left hand side of (B2) or a lower concentration $\Delta r_A(\Delta t) \le \Delta E \cdot \Delta t$ (see Eqs.(B5)) we cannot simply infer that nature is a net sink and therefore could not be responsible for any increasing CO_2 level.

Related to a constant native emission E_0 and the initial equilibrium mixing ratio $r_A(0) = E_0 \cdot \tau_{eff}$, nature surely acts as a further increasing sink, driven by the additional native or human emissions ΔE. Thus, the environment indeed looks like a net absorber. But this absorption tracks the anomalous emission ΔE with some delay and cannot be larger than this emission, which in reali-

ty is even further increasing over time. Because native emission and absorption processes are largely independent phenomena, also with an increasing absorption can nature still be a net emitter to the atmosphere and even by far the strongest donator, as this and our previous studies (SH2; Harde 2019, Figs 8-10, Subsec. 5.3) clearly demonstrate.

References

Brechet, L., Lopez-Sangil, L., George, C., Birkett, A., Baxendale, C., Trujillo, B., and E. Sayer, 2018: *Distinct responses of soil respiration to experimental litter manipulation in temperatue woodland and tropical forest*, Ecol and Evolution, 8, 3787-3796.

CDIAC, 2017: Carbon Dioxide Information Analysis Center, ESS-DIVE Archive, https://cdiac.ess-dive.lbl.gov/, October 2022.

Connolly, R., M. Connolly, R. M. Carter, W. Soon, 2020: *How Much Human-Caused Global Warming Should We Expect with Business-As-Usual (BAU) Climate Policies? A Semi-Empirical Assessment,* Energies, vol. 13(6), 1365, pp. 1-51; https://doi.org/10.3390/en13061365.

Cui, Z., Zhao, Z., Zhai, Y., Sun, Z., Cheng, W., and C. Gu, 2020: *Use of double channel differences for reducing the surface emissivity dependence of microwave atmospheric temperature and humidity retreivals,* Earth and Space Science, 7, https://doi.org/10.1029/2019EA000854.

Durocher, G., Allen, A., Bastviken, D., Conrad, R., Gudasz, C., St-Pierre, A., Thanh-Duc, N., and P. del Giorgio, 2014: *Methane fluxes show consistent temperature dependence across microbial to ecosystem scales,* Nature, 507, 488-491.

ESA, 2017: Tropopheric Monitoring Instrument, ESA Greenhouse Gas CCI Project, http://www.esa-ghg-cci.org/, October 2022.

Etcheto, J. and L. Merlivat, 1988: *Satellite determination of the carbon dioxide exchange coefficient at the ocean-atmosphere interface: a first step*, J. Geophys Res., 93, 15669-15678.

Feely, R., Sabine, C., Takahashi, T., and R. Wanninkhof, 2001: *Uptake and storage of carbon dioxide in the ocean: The global CO_2 survey*, Oceanography, 14, 18-32.

Gauci, V., Gedney, N., Pangala, S., Stauffer, T., Weedon, G., and A. Enrich-Prast, 2021: *Non-flooded riparian Amazon trees are a regionally significant methane source*, Phil. Trans. Royal Soc., A380, 20200446.

Goltser, Y. and E. Litsyn, 2005: *Volterra integro-differential equations and infinite systems of ordinary differential equations*, Math. Comp. Modelling, 42, 221-233.

GPCC, 2020: Global Precipitation Climatology Centre, v2020, https://www.dwd.de/EN/ourservices/gpcc/gpcc.html, October 2022.

Harde, H., 2017: *Scrutinizing the carbon cycle and CO2 residence time in the atmosphere*, Global & Planetary Change, 152, pp. 19-26, http://dx.doi.org/10.1016/j.gloplacha.2017.02.009.

Harde, H, 2019: *What humans contribute to atmospheric CO_2: Comparison of carbon cycle models and observations*. Earth Sciences, 8, pp. 139-158, doi: 10.11648/j.earth.20190803.13.

Harde, H., 2021: *Methane Sensitivity*, http://hharde.de/#xl_xr_page_climate%20b, October 2022

Harde, H. and M. Salby, 2021: *What controls the atmospheric CO_2 level?* Science Climate Change, Vol.1, No.1, pp. 54 - 69, https://doi.org/10.53234/scc202106/22

Humlum, O., K. Stordahl and J.-E. Solheim, 2013: *The phase relation between atmospheric carbon dioxide and global temperature,* Global Planetary Change, 100, 51-69.

Jiang, Z., Tyrrell, T., Hydes, D., Dai, M., and S. Hartman, 2014: *Variability of alkalinity and the alkalinity-salinity relationship in the tropical and subtropical surface ocean*, Glob. Biogeochem. Cycles, 28, 729-742, https://doi.org/10.1002/2013GB004678

Kennedy, J., N. Rayner, C. Atkinson and R. Killick, 2019: *An ensemble data set of sea surface temperature change from 1850: The Met Office Hadley Centre HadSST.4.0.0.0 Data Set*, JGR Atmospheres, 124, 7719-7763.

D. Koutsoyiannis, Z. W. Kundzewicz, 2020: *Atmospheric Temperature and CO_2: Hen-Or-Egg Causality?*, Sci 2020, 2, 72; https://doi.org/10.3390/sci2040083

Le Quéré, C., Peters, G., Friedlingstein, P., Andrew, R., Canadell, J., Davis, S., Jackson, R., and M. Jones, 2021: *Fossil CO_2 emissions in the post-COVID-19 era*, Nature, 13, 197-199.

Lloyd, J. and J. Taylor, 1994: *On the temperature dependence of soil respiration*, Functional Ecology, 8 315-323.

Lunt, M., Palmer, P., Feng, L., Taylor, C., Boesch, H., and R. Parker, 2019: *An increase in methane emissions from tropical Africa between 2010 and 2016 inferred from satellite data*, Atmos. Chem. Phys., 19, 14721-14740.

Maier, M., Gartiser, V., Schengel, A., and V. Lang, 2020: *Long term gas monitoring as tool to understand soil processes*, Appl. Sci., 10, 8653-8683.

Maslanik, J., 2007: *Effects of weather on the retrieval of sea ice concentration and ice type from passive microwave data*, Int. J. Remote Sensing, 13, 37-54.

Nightingale, P., Malin, G., Law, C., Watson, A., Liss, P., Liddicoat, M., Boutin, J., and R. Upstill-Goddard, 2000: *In situ evaluation of air-sea gas exchange parameterizations using novel conservative and volatile tracers*, Global Biogeochem., 14, 373-387.

Nottingham, A., Baath, E., Reischke, S., Salinas, N., and P. Meir, 2018: *Adaptation of soil microbial growth to temperature: Using a tropical elevation gradient to predict future changes*, Glob. Change Biol., 25, 827-838.

Palmer, P., L. Eng, D. Baker, F. Chevallier, H. Bosch and P. Somkuti, 2019: *Net carbon emissions from African biosphere dominate pan-tropical atmospheric CO_2 signal*, Nature Comm., https://doi.org/10.1038/s41467-019-11097-w.

Pangala, S., Enrich-Prast, A., Basso, L., Peixoto, R., Bastviken, D., Hornibrook, E., Gatti, L., Marotta, H., Calazans, L., Sakuragui, C., Bastos, W., Malm, O., Gloor, E., Miller, J., and V. Gauci, 2017: *Large emissions from floodplain trees close the Amazon methane budget*, Nature, 552, 230-234.

Robbins, L., Hansen, M., Kleypas, J., and S. Meylan, 2010: *User-Friendly Seawater Carbon Calculator*, USGS Report 2010-1280, 17pp.

Salby, M., 2013: *Relationship between greenhouse gases and global temperature*, Video of lecture at Helmut-Schmidt-University, Hamburg, https://youtu.be/HeCqcKYj9Oc.

Salby, M., 2016: *Atmospheric carbon: Why it's not pollution and why humans cannot regulate it*. Video presentation, 18 July, University College London, https://youtu.be/3q-M uYkpT0.

Salby, M. and H. Harde, 2021a (SH1): *Control of atmospheric CO_2 - Part I: Relation of carbon 14 to the removal of CO_2*, Science Climate Change vol. 1, no. 2, pp. 177-195, https://doi.org/10.53234/scc202112/30.

Salby, M. and H. Harde, 2021b (SH2): *Control of Atmospheric CO_2 - Part II: Influence of Tropical Warming*, Science of Climate Change, Vol. 1, No.2, pp. 196-212, https://doi.org/10.53234/scc202112/12.

Savage, K. and E. Davidson, 2001: *Interannual variation of soil respiration in two New England forests*, Glob. Biogeochem. Cycles, 15, 337-350.

Sixth Assessment Report (AR6), IPCC, 2021: V. Masson-Delmotte, P. Zhai, A. Pirani et al.: Climate Change 2021: *The Physical Science Basis. Contribution of Working Group I to the*

Sixth Assessment Report of the Intergovernmental Panel on Climate Change, Cambridge University Press, https://report.ipcc.ch/ar6/wg1/IPCC_AR6_WGI_FullReport.pdf.

Swanson, R., 2003: *Evidence of possible sea-ice influence on microwave sounding unit tropospheric temperature trends in polar regions*, Geophys. Res. Lett., 30, https://doi.org/10.1029/2003GL017938.

Takahashi, T., Feely, R., Weiss, R., Wanninkhof, R., Chipman, D., Sutherland, S. and T. Takahashi, 1997: *Global air-sea flux of CO_2: An estimate based on measurements of sea-air pCO_2 difference,* Proc. Nat. Acad. Sci. USA, 94, 8292-8299.

USGCRP, 2017: *Climate Science Special Report: 4th National Climate Assessment*, US Global Change Research Program, Washington DC, 470 pp, doi: 10.7930/J0J964J6.

Wang, D., C. Prigent, L. Kilic, S. Fox, C. Harlow, C. Jimenez, F. Aires, C. Grasiotti and F. Karbou, 2017: *Surface emissivity at microwaves to millimeter waves over polar regions: Parameterization and evaluation with aircraft experiments*, J. Atm. Ocean Tech., 34, 1039-1059.

Wanninkhof, R. and W. McGillis, 1999: *A cubic relationship between gas transfer and wind speed*, Geophys. Res. Lett., 26, 1889-1893.

Wanninkhof, R., 2014: *Relationship between wind speed and gas exchange over the ocean revisited*. Limnol Oceanogr. Methods, 12, 351-362.

Wijngaarden, W. A. van, W. Happer, 2020: *Dependence of Earth's Thermal Radiation on Five Most Abundant Greenhouse Gases,* arXiv.org > physics > arXiv:2006.03098 https://arxiv.org/pdf/2006.03098.pdf.

Wood, T., Detto, M., and W. Silver, 2013: *Sensitivity of soil respiration to variability in soil moisture and temperature in a humid tropical forest*, *PLOS ONE*, 8, https://doi.org/10.1371/journal.pone.0080965.

Wu, Y., Hain, M., Humphreys, M., Hartman, S., and T. Tyrrell, 2019: *What drives the latitudinal gradient in open-ocean surface dissolved inorganic carbon concentration?,* Biogeosci., 16, 2661-2681.

Zeebe, R., 2012: *History of seawater carbonate chemistry, atmospheric CO_2, and ocean acidification*, Annual Rev. Earth Plan. Sci., 40, 141-165, https://doi.org/10.1146/annurev-earth-042711-105521

Zhou, Z., Jian, L., Du, E., Hu, H., Li, Y., Chen, D., and J. Fang, 2013: *Temperature and substrate availability regulate soil respiration in the tropical mountain rainforests, Hainan Island, China,* J. Plant Ecology., Vol. 6, pp. 325-334, https://doi.org/10.1093/jpe/rtt034.

Vol 2.3 (2022)
pp. 239-257
Correspondance to
hans@schroder.dk

Less than Half of the Increase in Atmospheric CO_2 is Due to the Burning of Fossil Fuels

Hans Schrøder, MSc

Skodsborg, Denmark

Abstract:

The question is: What fraction of the observed increase in atmospheric CO_2 since 1750 is due to the burning of fossil fuels? Is it close to 1.0 as the IPCC and the climate policy makers would have us believe by saying that all, or nearly all, of the increase is due to the burning of fossil fuels i.e., the climate changes we are seeing are caused by humans. This paper is all about this fraction. I use networks of boxes and arrows that visualize the carbon accounting. I incorporate the photosynthesis and the temperature dependent non-fossil emission. The networks are balanced by solving simultaneous, linear equations, one for each box. Based on the law of the conservation of mass, in addition to elementary linear algebra, I present and apply a simple, universal, method for global carbon accounting. Assuming that the atmosphere behaves like a physical system with constant residence time 4.1 years, I apply the method and calculate the fraction to be 0.25. In addition, I find that the fraction is linked to the greening of the Earth, quantified as the increase in the photosynthesis on land and in the ocean. Finally, I render it probable that the increase in the non-fossil emission is caused by the temperature increase, the warming of the globe.

Keywords: Carbon balance, atmospheric CO_2, residence time, photosynthesis, greening
Submitted 24-02-2022. Accepted 20-09-22. Revised 10-10-2022. https://doi.org/10.53234/scc202112/17

1. Introduction

At the onset of the industrial revolution, about 1750, the atmosphere's CO_2 concentration was about 280 ppm and had been so for several hundreds of years, IPCC (2013). In the 2010s, it was about 405 ppm and rising. The increase, ΔC=125 ppm, is the sum of two parts. One is due to the burning of fossil fuels, ΔC_f, where subscript *f* stands for fossil. The other is ΔC_n, the non-fossil part, where subscript n stands for non-fossil. We have $\Delta C = \Delta C_f + \Delta C_n$. This paper is all about determining the fraction $\Delta C_f / \Delta C$ in order to answer the question: What fraction of the observed increase in atmospheric CO_2 is due to the burning of fossil fuels? This question is important, perhaps the most important question in the climate debate. If the fraction is smaller than 0.5, then the climate policy is way off the track. If it is close to 0, there is no climate crisis at all. The climate change is then not at all caused by humans. It is natural.

2. Assumptions and general notes

Some of the carbon fixed by photosynthesis is 'burned off' in the internal plant metabolism. The plant respiration, also called the autotrophic respiration, returns carbon to the atmosphere. According to Kirschbaum et al. (2001), it typically amounts to about half the carbon fixed by photosynthesis. This is adopted as the main assumption that underlies the present analysis: *Plant respiration is half of the photosynthesis.*

In Section 4.2, I apply yet another assumption: *The atmosphere behaves like a physical system with constant carbon residence time of 4.1 years.*

The concentration of atmospheric CO_2 is in units of ppmv (parts per million by volume in dry air). I omit the "v". To convert this CO_2 concentration into the total mass of atmospheric carbon in GtC (Gigatons of carbon), multiply the ppm by 2.12.

Data for this paper, up to and including Appendix A, come from The Global Carbon Project's (GCP) Global Carbon Budget for the 2010s found in Friedlingstein et al. (2020).

3. Method

3.1 General

It is a matter of conservation of carbon and linear algebra. The global carbon balance is depicted as a network of five boxes (control volumes) connected by arrows symbolizing flows. The conservation equation states that the stock change, in all boxes, over a specified period of time, equals input minus output during the same period of time. This translates into five simultaneous, linear equations with five unknowns making the double-entry bookkeeping method, and the input-output method, a matter of elementary linear algebra.

The method owes a lot to the classical input-out analysis, Leontief (1986). The differences are that I use networks of boxes instead of input-output tables, and my "currencies" are not goods, services and money, but any conserved quantity, carbon in this case.

An ambition of this paper is to keep things as simple as possible, especially the network. The simplest possible network for the global carbon balance, I can think of, is shown in Figure 1.

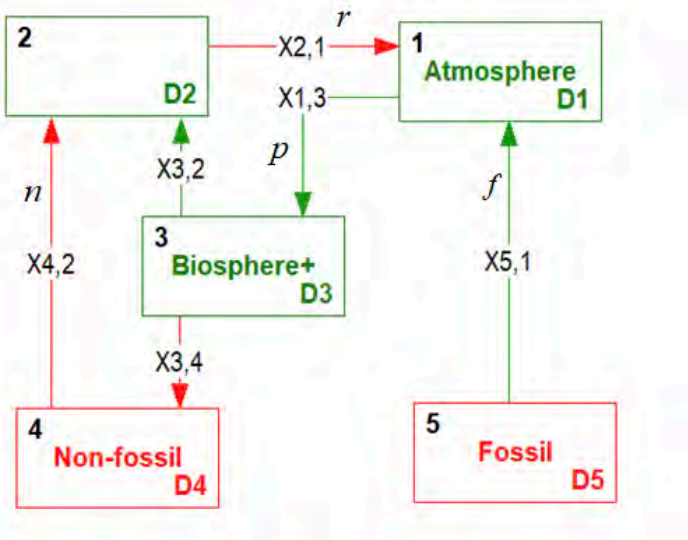

Figure 1. Flows and stock changes in the global carbon balance. Box numbers stand in upper left-hand corners. Xi,j is the flow of carbon from Box i into Box j. The stock change is placed in the lower right-hand corner. Green = knowns; Red = unknowns.

This is a simplified balance. It works on the assumption that there are two separate carbon cycles: A cycle linking land and the atmosphere, and another cycle linking the ocean and the atmosphere. In Figures 1, 3, 4 and 5, these cycles are added. In other words, I add the land-atmosphere cycle (annually fueled by 120 GtC fixed by land photosynthesis), and the ocean-atmosphere cycle (annually fueled by 90 GtC fixed by ocean photosynthesis), in order to keep the network as simple as possible. At the expense of simplicity, in Appendix C, I show the two cycles separately.

The flows are,

p is photosynthesis = X1,3

n is the non-fossil, temperature dependent, emission = X4,2

f is the emission from fossil fuels burning and cement production = X5,1

r is respiration = X2,1

The changes are,

*D*1 is the change of the stock of atmospheric carbon

*D*2 is nil by definition

*D*3 is land use change (mainly deforestation)

*D*4 is the change of the earth's stock of organic matter (recently) accumulated on land and in sediments of the ocean and the freshwaters

*D*5 is the change of the earth's stock of fossil fuels and limestone.

The sum of these stock changes must equal zero, because the system is closed.

Box 2 has no stock change since it is not a physical system; it merely serves to receive two flows, X4,2 and X3,2 and pass them on to the atmosphere. To mix physical and nonphysical systems is not normally done. Here I make an exception.

The balanced networks in Figures 1, 3, 4 and 5 incorporate the photosynthesis, *p*, and the non-fossil, temperature dependent flow, *n*, in the balance and links them to other variables, such as *f*, by linear algebra. Thereby, the carbon *balance* differs from IPCC's and GCP's carbon cycles or budgets.

Suppose we aggregate Box 2, 3 and 4 into a single box, in other words, that we add their balance equations. That would leave us with a diagram showing a one-way flow of carbon from the stock of fossil fuels into the atmosphere, and from there into land and ocean reservoirs. The photosynthesis, and the non-fossil emission cancel. This makes the burning of fossil fuels the only source of carbon to the atmosphere. This wrong perception becomes apparent, when the IPCC claims that carbon from the stock of fossil fuels is "distributed" to three reservoirs: The atmosphere, land, and the ocean.

It certainly looks so, since the negative change of the stock of fossil fuels carbon, added to the positive stock changes in the atmosphere, on land, and in the ocean is zero by virtue of the law of the conservation of mass. But we need to understand how this distribution to the three reservoirs comes about by applying linear algebra.

3.2 The equations

The conservation equation for atmospheric carbon is,

$$D1 = input - output \tag{1}$$

Referring to Figure 1, we have,

$$D1 = r + f - p \tag{2}$$

The main assumption translates into,

$$r = n + 0.5p \tag{3}$$

Insert this in Equation (2), and arrange terms to get,

$$D1 + 0.5p = n + f \tag{4}$$

By definition we have,

$$D1 = \frac{dA}{dt} \tag{5}$$

So, in recognizable mathematical notation, the equation for the conservation of atmospheric carbon is this first order differential equation,

$$\frac{dA}{dt} + 0.5p(A) = n(T(t)) + f(t) \tag{6}$$

On the left-hand side of the equation, A is the atmosphere's stock of carbon, and t is time. The photosynthesis $p(A)$ is a function of A, and therefore also of t.

On the right-hand side of the equation is the "forcing functions", called so because they are independent of the stock. The non-fossil emission $n(T(t))$ is a function of temperature T, which is a function of time; $f(t)$ is a function of time only.

The atmosphere can be thought of as a bathtub with two forcing functions represented by two faucet flows, n and f. We have an output of $0.5p$ 'down the drain', see Figure 2. Half of the total output, i.e., the photosynthesis, is returned to the atmosphere by plant respiration. This circular flow makes no difference to the balance since it is an input and an output.

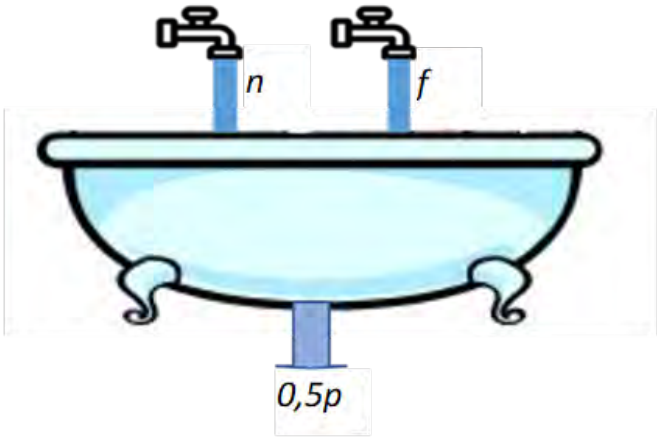

Figure 2. The atmosphere compared to a bathtub with two faucets.

The conservation equation is valid at any time. I consider two points in time: 1750 (t = 0), and the 2010s (t =265 years). Suppose the flows n and f increased in equal amounts, $\Delta n = \Delta f$, then they would each contribute half of the observed increase. In general, the fraction due to the burning of fossil fuels is,

$$\alpha_f = \frac{\Delta f}{\Delta f + \Delta n} = \frac{\Delta C_f}{\Delta C} \tag{7}$$

where Δf is the increase in the emission of CO_2-C due to the burning of *f*ossil fuels, and Δn is the increase in the non-fossil, temperature dependent, emission.

The fraction, α_f, is also the increase in atmospheric CO_2 concentration, due to the burning of fossil fuels, in proportion to the observed increase.

This is an approximation. Strictly speaking, it is valid only under steady-state conditions, i.e., when the stock changes are zero. It applies as an approximation to conditions in which the stock changes are so small, compared to other terms in the equation, that they can be omitted in a first order approximation. In the present case, the stock change term amounts to about five percent. Considering the other uncertainties involved, the approximation is considered acceptable.

4. Results

4.1 Determining Δn, the increase in the non-fossil, temperature dependent emission

First, consider the balance equation for atmospheric carbon,

$$D1(t) + 0.5p(t) = n(t) + f(t) \tag{8}$$

Second, set t = 0 to get the balance in 1750,

$$D1(0) + 0.5p(0) = n(0) + f(0) \tag{9}$$

At that time, the system, supposedly, was in a steady state. In other words, the change of the atmosphere's stock of carbon, $D1(0)$ was close to zero, and, of course, $f(0) = 0$. Hence,

$$0.5\, p(0) = n(0) \tag{10}$$

Subtract Equation (10) from Equation (8) to get,

$$D1(t) + 0.5\Delta p = \Delta n + \Delta f \tag{11}$$

in which Δp is the increase in the photosynthesis on land and in the ocean. Δn is the increase in the non-fossil emission, from land and from the ocean, and finally, Δf is the increase in the emission of carbon due to the burning of fossil fuels.

Rearrange to get,

$$\Delta n = 0.5\Delta p + D1(t) - f(t) \tag{12}$$

Note that $f(t) = \Delta f$ since $f(0) = 0$.

At t = 265 years, we have $D1(t)$ = 5.1 GtC per year, and $f(t)$ = 9.4 GtC per year, Friedlingstein et al. (2020), so that,

$$\Delta n = 0.5\Delta p - 4.3 \text{ (GtC per year)} \tag{13}$$

which lets us calculate Δn, and subsequently α_f, as a function of Δp, the increase in the global photosynthesis, the "greening of the Earth".

Solve for Δp and get,

$$\Delta p = 2\Delta n + 8.6 \text{ (GtC per year)} \tag{14}$$

The IPCC and the climate policy makers seem to believe that there is only one source of carbon dioxide to the atmosphere: the burning of fossil fuels. This is true only if one assumes that the flow, n, has stayed constant since 1750 in spite of the warming. In other words, Δn = 0. Insert this in Equation to get Δp = 8.6 GtC per year, which is the corresponding increase in the photosynthesis.

Up to this point, I have only considered the increase in the photosynthesis without mentioning its actual magnitude. The Global Carbon Budget 2020, shown in Appendix A, indicates that the photosynthesis in the 2010s is 120 GtC per year on land, and 90 GtC per year in the ocean, a total of 210 GtC per year. For Δn = 0, the photosynthesis would therefore have increased by a factor of 210/(210–8.6) =1.04 or four percent, which is much lower than normally estimated in climate research.

IPCC (2013) estimates that Δn = 34.1 GtC per year, see Table B1. The factor then is 210/(210 –34.1) = 1.19 or 19 percent, which is likely, but it contradicts IPCC's own claim that burning of fossil fuels is the only source of carbon to the atmosphere.

4.2 Calculation of α_f assuming the atmosphere behaves like a physical system with constant residence time 4.1 years

A commonly applied hypothesis in the modelling of physical systems, is that outflow is proportional to level, Berry (2021). In other words, output is proportional to stock. The photosynthesis, p, is the dominant output from the atmosphere. The residence time T_r, also called the turnover time, or the "e- time", is defined as the stock, A(t), divided by the output, p(t),

$$T_r = \frac{A(t)}{p(t)} \tag{15}$$

The hypothesis output is proportional to stock, is equivalent to saying that T_r is constant, and that p is proportional to A, and hence to C. For t=256 years (the 2010s), $C(t)$ = 405 ppm, so that,

$$T_r = \frac{2.12 \times 405}{210} = 4.1 \text{ years} \tag{16}$$

The hypothesis works well for physical systems, e.g., electrical circuits, but it has to be a first order approximation when applied to the global carbon balance. Nevertheless, tentatively assume that the residence time is constant, the same at all times, including t = 0. Then,

$$\frac{A(t)}{p(t)} = \frac{A(0)}{p(0)} \tag{17}$$

and therefore,

$$\frac{A(t)}{A(0)} = \frac{p(t)}{p(0)} = \frac{C(t)}{C(0)} \tag{18}$$

from which,

$$p(0) = \frac{C(0)}{C(t)} p(t) \tag{19}$$

and,

$$\Delta p = p(t)\left(1 - \frac{C(0)}{C(t)}\right) = 210\left(1 - \frac{280}{405}\right) = 65 \text{ GtC per year} \tag{20}$$

which inserted in Equation (13) gives Δn = 0.5×65–4.3 = 28.2 GtC per year, which inserted in Equation (7), along with Δf = 9.4 GtC per year, gives α_f = 9.4 / (9.4 +28.2) = 0.25.

So, assuming a constant residence time of 4.1 years (in addition to the main assumption of this paper), 25 percent of the observed increase in the CO_2 concentration is due to the burning of fossil fuels.

4.3 Others' results

Berry (2021) applies a residence time, or "e-time" as he calls it, of 3.5 years. As opposed to the present analysis, he used IPCC data only and numerically solved four simultaneous differential equations using recursive, annual time steps from 1750 to 2020. He found ΔC_f = 33 ppm and ΔC = 133 ppm (in 2020) from which α_f = 33 / 133 = 0.25.

Applying a constant residence time of 3.5 years, instead of 4.1 years, gives, α_f = 0.22. Likewise, the number of years since 1750 plays a role. The present analysis deviates (slightly) from Berry's on both accounts. Yet, the result comes out to be the same to the second decimal place.

Skrable et al. (2022) established annual mean values in 1750 through 2018 of the atmosphere's specific activity of ^{14}C, which gets diluted when fossil CO_2-C (devoid of ^{14}C) enters the atmosphere. From this, they were able to calculate ΔC_f = 47 ppm (in 2018) out of the observed increase of 129 ppm, which makes α_f =47 / 129 = 0.36.

Harde (2019) found ΔC_f = 17 ppm. He sets the concentration increase since 1750 at 113 ppm, making α_f = 17 / 113 = 0.15.

4.4. The fraction α_f is linked to the greening

There is a unique relationship between the greening, the increase in the photosynthesis, on the one hand, and the fraction α_f on the other. An estimate of Δp, translates into an estimate of α_f.

Table 1. Results in the framework of the present analysis.

	α_f	Photosynthesis increase percent	Δn GtC/yr	Δf GtC/yr	Δp GtC/yr	$n(t) / n(0)$
IPCC	1.00	4	0	9.4	8.6	1.00
For reference	0.50	15	9.4	9.4	27.4	1.10
Skrable et al.	0.36	25	16.7	9.4	42.0	1.20
Present + Berry	0.25	45	28.2	9.4	65.0	1.39
Harde	0.15	121	53.3	9.4	115.0	2.12

The increase in the photosynthesis is four percent in the very unlikely event that the rate of decomposition of organic matter stayed constant ($\Delta n = 0$) since 1750 – in spite of the warming. At 15 percent increase, $\alpha_f = 0.50$, and so on down to the bottom row, where $\alpha_f = 0.15$, i.e., 15 percent of the increase in atmospheric CO_2 is due to the burning of fossil fuels.

This result, however, does not fit the present analysis, since it is not likely that the photosynthesis more than doubled. An increase in the range 25 to 45 percent is more likely, corresponding to α_f in the range 0.36 to 0.25, say about a third.

5. Balanced networks visualize the carbon accounting

One can also determine Δn, and therefore also α_f, by means of networks of boxes, with stock changes, and arrows as flows, balanced by solving the simultaneous conservation equations.

In money accounting, one has to record all flows and stock changes to make sure money neither disappears nor appears. In carbon accounting, we know for sure that carbon is a conserved quantity. Each box in the network therefore holds its balance equation. This allows us to calculate, in the present case, five variables (flows and stock changes). This approach makes things easy; it is nothing but linear algebra. In addition, the visualization of the accounting makes the balance easier to comprehend.

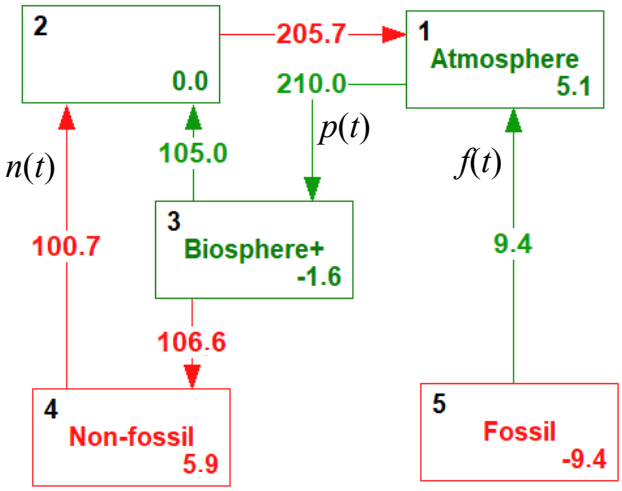

Figure 3. The global carbon balance averaged over the 2010s, GtC per year. Compare with the Global Carbon Budget 2020, Friedlingstein et al. (2020) shown in Appendix A.

The Global Carbon Budget 2020, and the present global carbon balance for the 2010s, are compared in Appendix A. Notice that

$$D3 + D4 = -1.6 + 5.9 = 4.3 = p - r = f - D1 \tag{21}$$

and that the sum of the stock changes equals zero.

There are five boxes, and therefore five linear conservation equations with five unknowns, dependent variables, data output shown in red.

In contrast, the green variables are independent variables, data input. So, if we enter the variables valid for the time around 1750, and solve the new set of simultaneous equations, we get the global carbon balance at that time.

In the pre-industrial era, $f(0) = 0$. The system supposedly was in quasi-steady state with stock changes close to zero – with one exception, namely the land use change, $D3$, which was minus 0.7 GtC per year at that time.

The photosynthesis in 1750 ($t = 0$) remains to be estimated in order to proceed. Take for example

$$p(0) = 145 \text{ GtC/year} \tag{22}$$

to make the fraction 0.25. Now, the five simultaneous equations can be solved to yield the balanced network for 1750 shown in Figure 4.

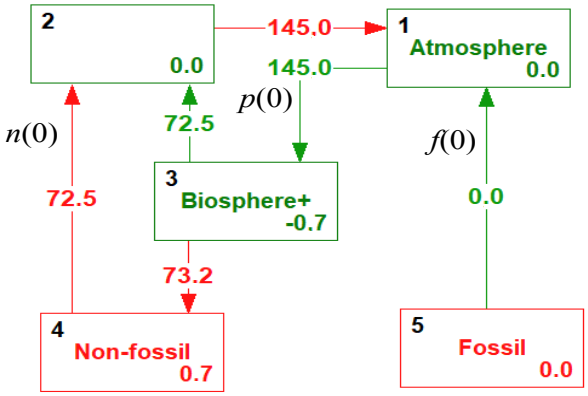

Figure 4. The global carbon balance 1750, GtC per year.

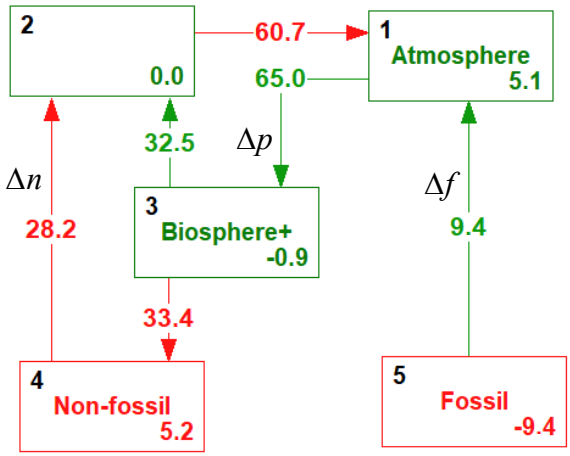

Figure 5. The balance in Figure 3 (2010s) minus the balance in Figure 4 (1750) in GtC per year.

In Figure 5,

$$\Delta n = 28.2 \text{ GtC per year} \tag{23}$$

and

$$\Delta f = 9.4 \text{ GtC per year} \tag{24}$$

Applying Equation (7), we get

$$\alpha_f = \frac{9.4}{9.4 + 28.2} = 0.25 \tag{25}$$

The input-output approach is easy to comprehend because of the visualization. It is a matter of using an easily programmed piece of software, which, based on the network, automatically sets up the simultaneous equations and solves them on command.

6. The role of the ocean

It is often asserted that the ocean plays a decisive role. During the glacial-interglacial cycles, the ocean has no doubt played an important role, but apparently not during the last 265 years.

My explanation is this: In the 2010s, the land sink was 3.4 GtC per year, and the ocean sink 2.5 GtC per year, see Appendix A. The total sink (stock change) is 5.9 GtC per year, which stands in the lower right-hand corner of Box 4 in Figure 3.

The land sink is caused by the photosynthesis, it is biological only, while the ocean sink has a physical component (governed by Henry's Law) in addition to a biological component, the biological pump.

The physical component has to be smaller than 2.5 GtC per year in order to leave room for the biological pump. I estimate it to be in the order of 0.5 GtC per year, which, considering the uncertainties involved, is too small to justify a (much) more detailed network to account for it.

7. Discussion

7.1 The hypothesis residence time is constant

The outflow is proportional to level (stock) hypothesis is equivalent to saying that the photosynthesis is proportional to the CO_2 concentration. Think of it as a giant plant nutrition experiment. The fertilizer, CO_2, is added to the atmosphere in increasing amounts.

In response, the yield, the photosynthesis, increases, but why exactly in direct proportion to the concentration? This would make the yield curve a straight line passing through the origin of the coordinate system. The yield curve, however, is expected to bend downwards, and it doesn't pass through the origin of the coordinate system since the photosynthesis ceases to work when the CO_2 concentration gets below 150 ppm.

Still, the result that about 25 percent of the increase in atmospheric CO_2 is due to the burning of fossil fuels, stands out. First, because the result has been obtained independently by two researchers. Second, because the result can be calculated using elementary mathematics.

7.2 Sensitivity to the main assumption

The main assumption is that the plant respiration is half of the photosynthesis: 0.5p. Had the coefficient instead been 0.4, it would change the fraction α_f from 0.25 to 0.30. Had it been 0.6, it would change it to 0.21. So, the result depends on the estimate of the coefficient, but not to an extent where it invalidates the conclusion.

7.3 The temperature increase explains the non-fossil emission increase

The temperature increase has a direct effect on the emission, *n(t)*, since it speeds up the rate of decomposition of organic matter. The temperature coefficient, Q_{10}, is defined as the factor by which the rate increases when the temperature is increased 10°C. For most biological systems, Q_{10} is between 2 and 3, say 2.5. The non-fossil emission today divided by the emission in 1750 is

$$\frac{n(t)}{n(0)} = Q_{10}^{\left\{\frac{\Delta T}{10}\right\}} \tag{26}$$

in which $\Delta T = 1.1$ °C is the increase in the average global temperature since 1750, so that the factor becomes $2.5^{0.11} = 1.1$. In other words, the non-fossil emission, n, would increase by about 10 percent, if the direct effect of temperature on the rate of decomposition were the only governing variable.

It isn't. A warmer climate is generally also a wetter climate because of increased evaporation. So, on land, there is an indirect, additional effect of the warming since the extra soil moisture enhances the rate of decomposition. Hence, the actual effect of the temperature increase is to make the above-mentioned factor greater than 1.1, and therefore α_f smaller than 0.5, see Table 1.

Harde (2019) concludes: "Thus, not really anthropogenic emissions but mainly natural processes, in particular the temperature, have to be considered as the dominating impacts for the observed CO_2 increase over the last 270 years."

Temperature is the only 'process' by which carbon can move from land and ocean reservoirs into the atmosphere. In conclusion, the increase in the non-fossil emission is caused by the temperature increase, the warming of the globe.

Berry (2021), Harde (2019) and others speak of *n*, the non-fossil, temperature dependent emission, as the "natural" emission. I prefer to call it the "non-fossil" emission, because not all of the temperature increase is natural.

Conclusion

Less than half of the observed increase in atmospheric CO_2 since 1750, probably about a third, is due to the burning of fossil fuels. The rest of the increase is caused by the warming.

Acknowledgment

I am indebted to Niels Kristian Højerslev (PhD, physical oceanography) for undaunted support and encouragement. Also, I thank Ulla Kjær for helpful comments on the manuscript. Special thanks to two anonymous referees for a thorough review, which significantly improved the paper.

References

Berry, E.X., 2021: **The impact of human CO_2 on atmospheric CO_2**. Science of Climate Change, vol. 1, no. 2, Nov. 2021, pp. N3 1-46. The impact of human CO_2 on atmospheric CO_2 - SCC (klimarealistene.com)

Friedlingstein, P., O'Sullivan, M., Jones, M. W., Andrew, R. M., Hauck, J., Olsen, A., Peters, G. P., Peters, W., Pongratz, J., Sitch, S., Le Quéré, C., Canadell, J. G., Ciais, P., Jackson, R. B., Alin, S., Aragão, L. E. O. C., Arneth, A., Arora, V., Bates, N. R., Becker, M., Benoit-Cattin, A., Bittig, H. C., Bopp, L., Bultan, S., Chandra, N., Chevallier, F., Chini, L. P., Evans, W., Florentie, L., Forster, P. M., Gasser, T., Gehlen, M., Gilfillan, D., Gkritzalis, T., Gregor, L., Gruber, N., Harris, I., Hartung, K., Haverd, V., Houghton, R. A., Ilyina, T., Jain, A. K., Joetzjer, E., Kadono, K., Kato, E., Kitidis, V., Korsbakken, J. I., Landschützer, P., Lefèvre, N., Lenton, A., Lienert, S., Liu, Z., Lombardozzi, D., Marland, G., Metzl, N., Munro, D. R., Nabel, J. E. M. S., Nakaoka, S.-I., Niwa, Y., O'Brien, K., Ono, T., Palmer, P. I., Pierrot, D., Poulter, B., Resplandy, L., Robertson, E., Rödenbeck, C., Schwinger, J., Séférian, R., Skjelvan, I., Smith, A. J. P., Sutton, A. J., Tanhua, T., Tans, P. P., Tian, H., Tilbrook, B., van der Werf, G., Vuichard, N., Walker, A. P., Wanninkhof, R., Watson, A. J., Willis, D., Wiltshire, A. J., Yuan, W., Yue, X., and Zaehle, S.: **Global Carbon Budget 2020**, Earth Syst. Sci. Data, 12, 3269–3340, https://doi.org/10.5194/essd-12-3269-2020, 2020. https://essd.copernicus.org/articles/12/3269/2020/#abstract

Harde, H., 2019: **What Humans Contribute to Atmospheric CO_2: Comparison of Carbon Cycle Models with Observations**. Earth Sciences. Vol. 8, No. 3, 2019, pp. 139-159. https://www.researchgate.net/publication/335418316_What_Humans_Contribute_to_Atmospheric_CO2_Comparison_of_Carbon_Cycle_Models_with_Observations

IPCC, 2013: Ciais, P., C. Sabine, G. Bala, L. Bopp, V. Brovkin, J. Canadell, A. Chhabra, R. DeFries, J. Galloway, M. Heimann, C. Jones, C. Le Quéré, R.B. Myneni, S. Piao and P. Thornton, 2013: **Carbon and Other Biogeochemical Cycles. In: Climate Change 2013: The Physical Science Basis**. Contribution of Working Group I to the Fifth Assessment Report of the Intergovernmental Panel on Climate Change [Stocker, T.F., D. Qin, G.-K. Plattner, M. Tignor, S.K. Allen, J. Boschung, A. Nauels, Y. Xia, V. Bex and P.M. Midgley (eds.)]. Cambridge University Press, Cambridge, United Kingdom and New York, NY, USA.https://www.ipcc.ch/site/assets/uploads/2018/02/WG1AR5_Chapter06_FINAL.pdf

Kirschbaum, M.U.F., Eamus, D., Gifford R.M., Roxburgh, S.H., and Sands, P.J., 2001: **Definitions of some ecological terms commonly used in carbon accounting**. NEE Workshop Proceedings: 18-20 April 2001 https://www.researchgate.net/publication/239863843

Leontief, W., 1985: **Input-output analysis**. Chapter in Input-Output Economics. Oxford University Press, 1986. https://books.google.dk/books?id=hBDEXblq6HsC&pg=PA19&hl=da&source=gbs_toc_r&cad=3#v=onepage&q&f=false

Pollard, P.C., 2022: **Globally, Freshwater Ecosystems Emit More CO_2 Than the Burning of Fossil Fuels**. Frontiers in Environmental Science http://doi.org/10.3389/fenvs.2022.904955

Skrable, K., Chabot, G., French, C., 2022: **World Atmospheric CO_2, Its 14C Specific Activity, Non-fossil Component, Anthropogenic Fossil Component, and Emissions (1750–2018)**. Health Physics: February 2022 - Volume 122 - Issue 2 - p 291-305 http://doi.org/10.1097/HP.0000000000000014

Appendix A

The Global Carbon Project's (GCP) global carbon budget for the 2010s and its transformation into a balanced network

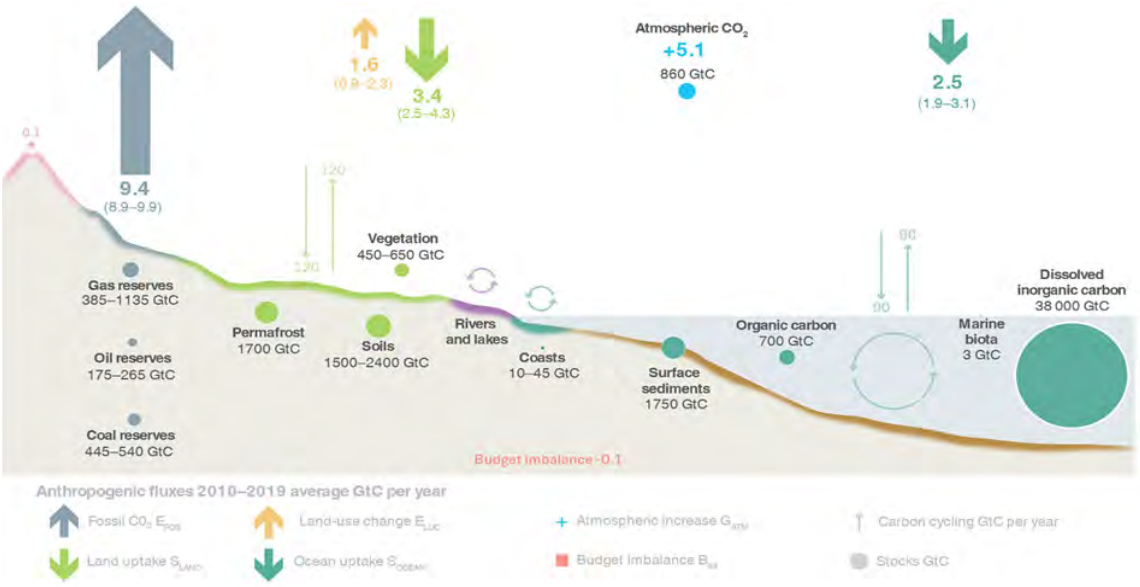

Figure A1. The Global Carbon Budget 2020, GtC per year for the 2010s, from Friedlingstein et al. (2020).

As mentioned in the main text, five data inputs are required in order to solve the balance equation and thus create a balanced network. Four of them are found in Figure A1:

p(t) = Photosynthesis, land + ocean =120 + 90 = 210 GtC per year (X1,3)
f(t) = Fossil fuels burning = 9.4 GtC per year (X5,1)
Stock change in the atmosphere = 5.1 GtC per year (D1)
Land use change = -1.6 GtC per year (D3)

The fifth follows from the main assumption,

0.5p(t) = Plant respiration = 105.0 GtC per year (X3,2)

The balanced network is shown in Figure A2, which is identical to Figure 3 in the main text.

The balance equations are,

$$D1 = X2,1+X5,1–X1,3$$
$$0 = X4,2+X3,2–X2,1$$
$$D3 = X1,3–X3,2–X3,4$$
$$D4 = X3,4–X4,2$$
$$D5 = –X5,1$$

Green are independent variables, data input: X1,3; X5,1; X3,2; D1; D2(=0); D3. Red are dependent variables, data output: X4,2; X2,1; X3,4; D4; D5

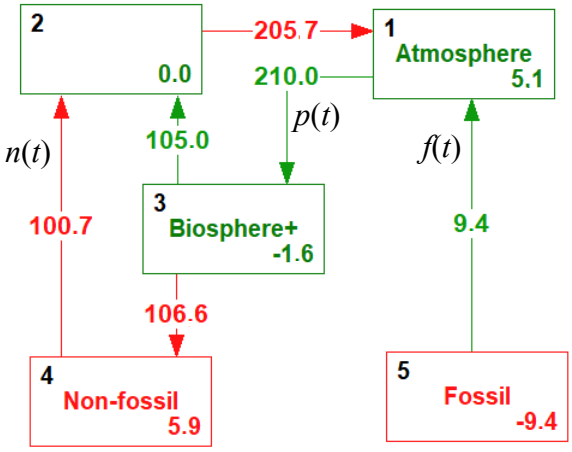

Figure A2. Figure 3 in main text. The Global Carbon Budget in Figure A1 transformed into a balanced network. The stock changes, and hence the grand balances, are the same. The difference is that the balanced network incorporates the photosynthesis, and the important non-fossil, temperature dependent flow of carbon, into a firm and simple mathematical structure, a set of (in the present case) five simultaneous linear equations.

Manually to set up the matrix of coefficients, and the right-hand side of the equations, is a tedious and time-consuming task. Fortunately, it is easily programmed. We draw a network of boxes connected by flows. The program automatically establishes the associated set of balance equations, and solves them as soon as one enters the green variables.

Appendix B

IPCC's carbon cycle and its transformation into a balanced network

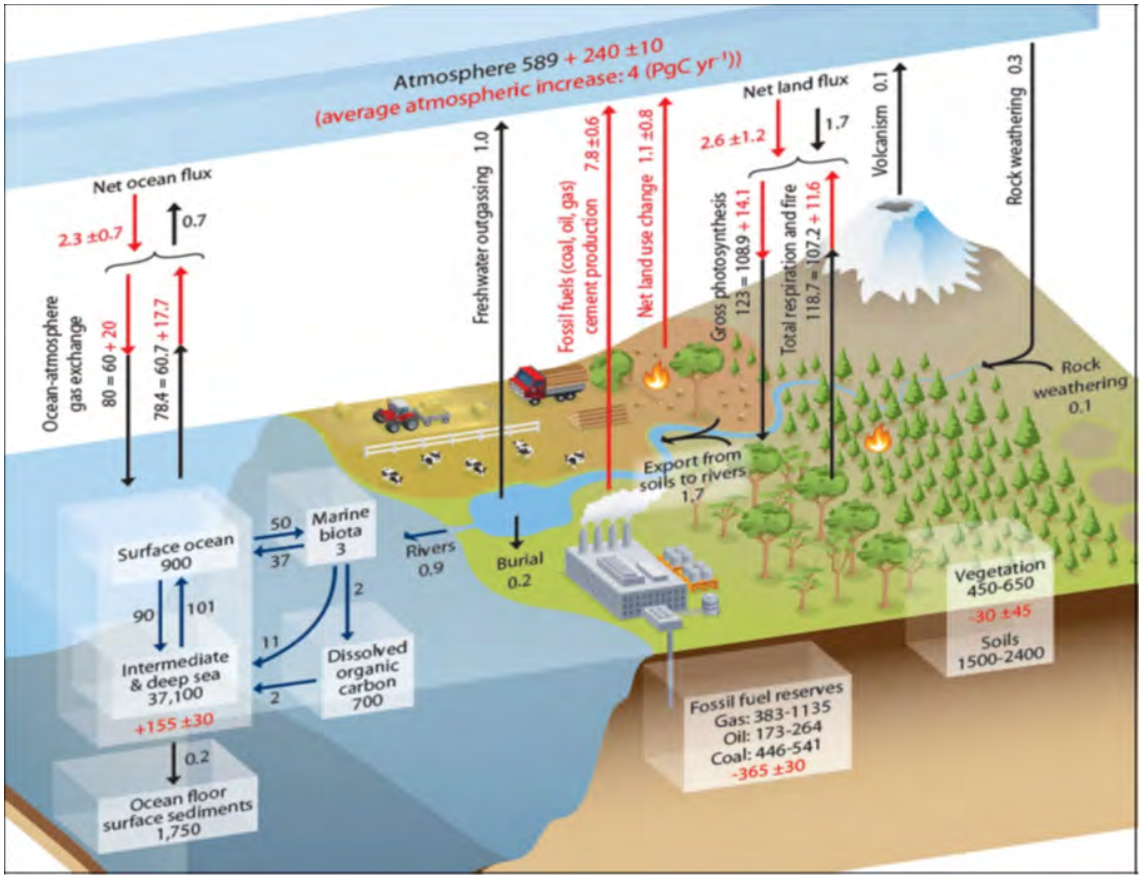

Figure B1 = Figure 6.1 in IPCC (2013) showing IPCC's data for natural (black) and human (red) carbon cycles.

IPCC's carbon cycle does not specifically mention the ocean photosynthesis, it only implies its presence by the arrows labelled "Ocean-atmosphere gas exchange". This gas exchange is generated by the ocean photosynthesis and respiration.

Likewise, IPCC does not distinguish between plant respiration (autotrophic) on the one hand, and respiration from bacterial decay (heterotrophic) on the other, but considers the total only, meaning autotrophic plus heterotrophic, not total in the sense global.

Table B1. IPCC data extracted from Figure B1.

GtC per year	Input to atmosphere			Output from atmosphere			Input - output = stock change		
	Natural	Human	Total	Natural	Human	Total	Natural	Human	Total
Land	107.2	11.6	118.8	108.9	14.1	123.0	-1.7	-2.5	-4.2
Surface ocean	60.7	17.7	78.4	60.0	20.0	80.0	0.7	-2.3	-1.6
Fossil fuels and cement prod.	0.0	7.8	7.8	0.0	0.0	0.0	0.0	7.8	7.8
Outgassing	1.0	0,0	1.0	0.0	0.0	0.0	1.0	0.0	1.0
Net land use change	0.0	1.1	1.1	0.0	0.0	0.0	0.0	1.1	1.1
Total	**168.9**	**38.2**	**207.1**	**168.9**	**34.1**	**203.0**	**0.0**	**4.1**	**4.1**

Note that the natural stock changes are not zero, as they should be. Another problem with IPCC's data is that the net land use change is not a flow, but a stock change. In addition, the fresh water outgassing seems to be greatly underestimated, Pollard (2022), see Appendix C.

Disregarding these shortcomings, Table B1 yields,

X1,3 = *p(t)* = Photosynthesis, land + ocean =123 + 80 = 203 GtC per year

X5,1 = *f(t)* = Fossil fuels burning = 7.8 GtC per year

D1 = Stock change in the atmosphere = 4.1 GtC per year

D3 = Land use change = –1.1 GtC per year

The last data input follows from the main assumption,

X3,2 = 0.5*p(t)* = Plant respiration = 0.5·203 = 101.5 GtC per year.

By entering these numbers, the five simultaneous linear equations can be solved. The result is the balanced network shown in Figure B2.

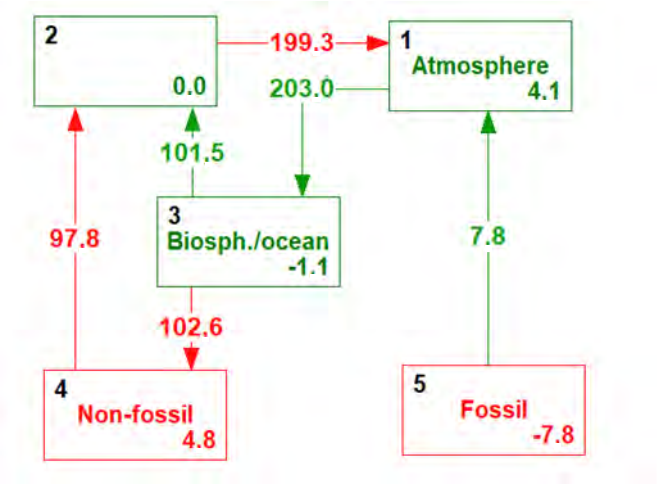

Figure B2. The global carbon balance for the 2000s derived from IPCCs carbon cycle data. GtC per year. The 4.8 GtC per year in the lower right-hand corner of Box 4 is the sum of the land sink of 2.5 GtC per year and the ocean sink of 2.3 GtC per year.

Compare with Figure A2. The difference between the balances in Figure A2 and B2 is explained by the fact that they are 10 years apart. The flow that drives the balance has increased 3.4 percent over 10 years, which looks reasonable. Oher variables, such as D1 and D5 are measured.

Note that the sum of the stock changes is zero. Also note that D3 + D4 = –1.1 + 4.8 = 3.7 = 203.0 –199.3 = 7.8 – 4.1. The ocean sink is 2.5 and the land sink is 2.3 making a total sink of 4.8, which stand in the lower right-hand corner of Box 4.

Table B2. Flows and stock changes in the balanced network a) according to the IPCC for the 2000s (2005) in Figure B2, and b) according to the GCP for the 2010s (2015) shown in Figure 3 (and Figure A2).

			IPCC	GCP
			2005	2015
			GtC per year	
Flows			Fig. B2	Fig. 3
p(t)	**X1,3**	**Photosynthesis**	**203.0**	**210.0**
f(t)	**X5,1**	**Fossil fuels and cement prod.**	**7.8**	**9.4**
0.5*p(t)*	**X3,2**	**Plant respiration**	**101.5**	**105.0**
n(t)	**X4,2**	**Non-fossil emission**	**97.8**	**100.7**
r(t)	**X2,1**	**Total respiration**	**199.3**	**205.7**
	X3,4	**Net primary production**	**102.6**	**106.6**
Stock changes				
	D1	**Atmosphere**	**4.1**	**5.1**
	D2	**Zero per definition**	**0.0**	**0.0**
	D3	**Land use change**	**-1.1**	**- 1.6**
	D4	**Non-fossil (organic matter)**	**4.8**	**5.9**
	D5	**Fossil fuels**	**-7.8**	**-9.4**

Appendix C

Detailing the network by separating the land and the ocean system and by including inland fresh waters

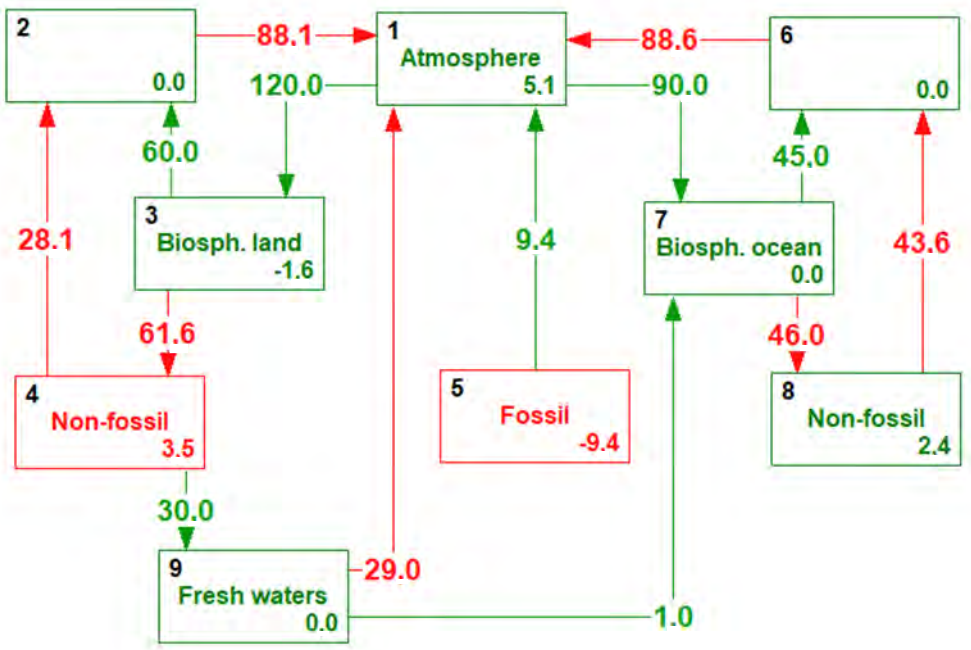

Figure C1. The network in Figure 3 detailed by separating the land and the ocean system, and by including inland fresh waters. GtC per year.

In the previous networks, I have added the land (120 GtC per year) and the ocean photosynthesis (90 GtC per year) to keep the network as simple as possible. At the expense of simplicity, I now separate the land balance from the ocean balance as shown in Figure C1. First, ignore Box 9 and notice the land sink = 3.4 GtC per year (Box 4), and the ocean sink = 2.5 GtC per year (Box 8), the total of which (5.9 GtC per year) stand in the lower right-hand corner of Box 4 in Figure 3. So, the land network on the left-hand side of Figure C1 added to the ocean network on the right-hand side yields the network in Figure 3.

To include the carbon emission from fresh waters, I add Box 9: Fresh waters. First consider Box 3, the Biosphere on land including inland (fresh) waters. The photosynthesis on land is about 120 GtC per year. According the main assumption of this paper, half of it is plant respiration, the other half is biomass. Hence, roughly half of the carbon fixed by photosynthesis, about 60 GtC per year, end up as biomass, dead or alive, on land and in fresh waters.

The magnitude of the fresh water outgassing

Then consider Box 4, labelled "Non-fossil" meaning it contains biomass accumulated on land and in fresh waters subject to bacterial decay. There is only one input to Box 4: X3,4. It is approximately half of the photosynthesis, hence about 60 GtC per year. There are two outputs from Box 4, one (X4,2) comes from solid land (excluding fresh waters), the other from fresh waters only (X9,1). In the numerical example, I have, for the sake of argument, taken X4,2 to be about equal to X9,1 so that about half of the carbon is emitted from land, and the rest from fresh waters.

Pollard (2022) finds that the emission of carbon from fresh waters on a global scale amounts to 58.5 GtC per year. For that to be true, there would be no emission from land. All of the decay of organic matter would take place in inland waters. It would take a violation of the law of the conservation of mass to fit the 58.5 GtC per year into the balance.

In the other extreme, the IPCC takes the fresh water outgassing to be in the order of 1 GtC per year. For this to be true, nearly all of the decay would take place from solid land, and comparatively nothing from fresh waters. In conclusion, the fresh water outgassing is somewhere in the interval between 1.0 and 58.5 GtC per year.

Guest editor: Stein Storlie Bergsmark. 2 anonymous referees.

Lunar Forced Mauna Loa and Atlantic CO_2 Variability

Correspondence to
Harald.Yndestad@ntnu.no

Vol. 2.3 (2022)
pp. 258-274

Harald Yndestad

Norwegian University of Science and Technology,
N-6025, Aalesund, Norway

Abstract

The source of atmospheric CO_2 variations is poorly understood. At Mauna Loa Hawaii, atmospheric CO_2 has been recorded from 1959. This is a short period for a reliable variability signature identification. From the 19th century, atmospheric CO_2 has been recorded in several short periods over the Atlantic Ocean and Europe. A number of these data series are compiled into a single atmospheric Atlantic CO_2 data series from 1820 to 1960. Altogether, this time series covers atmospheric CO_2 records over a total period of 200 years. In this investigation, a wavelet spectrum analysis identifies the signature of Mauna Loa atmospheric CO_2 growth from 1960 to 2020 and Atlantic atmospheric CO_2 for the period 1870 to 1960. The result reveals that the Atlantic CO_2 variability from 1870-1960 coincides with Mauna Loa CO_2 growth variability, global sea surface temperature variability and lunar nodal tide variability. The Atlantic CO_2 signature and global sea surface temperature signature and the have a phase difference of $\pi/2$ (rad), which reveals a sea temperature driven atmospheric CO_2 variation. The CO_2 variability signature coincides with the global sea temperature signature and the lunar nodal signature spectrum. The identified lunar nodal tide spectrum reveals a chain of events from lunar nodal tide variations to global sea surface temperature variations and atmospheric CO_2 variations. A lunar nodal tide spectrum in atmospheric CO_2 growth reveals that CO_2 is not controllable.

Keywords: Mauna Loa atmospheric CO_2 variability; Atlantic atmospheric CO_2 variability; Global Sea surface temperature variability; Lunar nodal tide variability.

Submitted 2022-10-08, Accepted 2022-12-18, https://doi.org/10.53234/scc202212/13.

1. Introduction

1.1 CO_2 at Mauna Loa, Hawaii

There had been a prevailing view of a direct connection between CO_2 and acidity in rivers and groundwater. In 1956, the young polymer chemistry scientist Charles David Keeling, began measuring the concentration of CO_2 in the atmosphere. The results showed that there was no such direct connection. At the same time, he discovered that CO_2 in the atmosphere had its own cycle. The concentration of CO_2 in the atmosphere was lower during the day, when nature absorbed CO_2 in photosynthesis. At sunset, photosynthesis stopped and released CO_2 back into the atmosphere. Keeling had discovered that the local forest breathed in diurnal variations.

Keeling used a new method to record CO_2, based on infrared spectroscopy, to create comparable samples over larger areas. With faster measurements, he was able to detect variations in CO_2 in landscapes and urban areas. CO_2 had large diurnal variations related to local conditions. In hope of finding a stable CO_2 background level, Keeling started monitoring CO_2 at Mount Mauna Loa, Hawaii. It soon turned out that the atmosphere breathed in annual

rhythm and CO_2 also did not have a stable background level. The CO_2 background level increased slightly each year. David Keeling had discovered that concentration of CO_2 in the atmosphere background was growing. This atmospheric CO_2 growth must have a source. The suspicion was accumulation of CO_2 from combustion of fossil fuels, which confirmed the Greenhouse paradigm (Kunzig and Wallace 2008; Keeling et al. 1976; Thoning et al. 1989; Thomas et al. 2016).

1.2 The Greenhouse paradigm

At the beginning of the 19th century, there was a belief in science that large stones in open landscapes were remnants of the flood, known from the Bible. Around 1830, it was discovered that these stones were remnants from an ice age. The discovery of ice ages created speculations about possible causes for these. In 1850, the Irish physicist John Tyndall conducted a laboratory experiment that showed that atmospheric infrared absorption is largely due to carbon dioxide and water vapor. The evidence was that water vapor has a strong effect on the absorption of infrared radiation emitted from the earth's surface. He stressed that the climate would be much colder at night in the absence of the greenhouse effect. This experiment created the idea, that CO_2 enters the atmosphere, and acts as a global climate regulator. He concluded that water vapor is the gas that most strongly absorbs heat radiation in the atmosphere and controls the air temperature (Kunzig and Wallace 2008; Thomas et al. 2016).

The Swedish geologist Arvid Högblom believed that CO_2 from volcanoes created large climate variations and controlled the risk of new ice ages. When volcanoes created a high concentration of CO_2 in the atmosphere, we had a warm climate period, where photosynthesis created more growth in the global ecosystem. The growth of the ecosystem drew CO_2 out of the atmosphere, and into the earth as plant remains. Less CO_2 in the atmosphere led to a gradually colder climate, and eventually a new ice age. Sooner or later, CO_2 emissions came into the atmosphere from volcanoes, which started a new warm climate period. There was a direct connection between CO_2, ecosystems, and ice ages. In the 1890s, the Swedish chemist Svante Arrhenius made calculations which showed that halving CO_2 in the atmosphere led to a global temperature reduction of 4-5 degrees. A doubling of CO_2 will lead to an estimated increase of 5-6 degrees. Arrhenius believed that human CO_2 supply to the atmosphere, had saved us from a new ice age (Kunzig and Wallace 2008; Thomas et al. 2016).

The English railway engineer Gay Stewart Callendar (1898-1964) began studying the relationship between global temperature and CO_2. Based on data from 147 global measuring stations, he was able to show that the global temperature had risen 0.3 degrees C from 1880 to 1930. This corresponds to approximately 0.6 degrees in 100 years. From 1880 to 1930, selected CO_2 measurements had risen by 6 %. In 1938 he wrote an article in which he pointed out that humans have already contributed to half of the CO_2 growth in the atmosphere. Humans had increased the global temperature by 0.3 degrees per century. This had led to a more pleasant climate in the northern hemisphere, following the cold climate of the 19th century, and saved the planet. Callendar developed a model that showed a linear relationship between man-made CO_2 and global temperature. This linear relation between CO_2 and global temperature, introduced the idea of climate as a closed system on Earth, which ignores natural variations (Kunzig and Wallace 2008; Thomas et al. 2016; Anderson et al. 2016).

1.3 Ocean surface carbon system

The young Japanese student Taro Takahashi studied to become a mining engineer, like his father and grandfather. After his studies, he was tempted to participate in the study of the Atlantic Ocean to record CO_2 in the atmosphere. This was the start of a 60-year research project. Atmospheric CO_2 growth had raised questions about the impact on the ocean's carbon system. In the 1970s, Taro Takahashi began measuring CO_2 over oceans. He discovered that oceans breathed CO_2 over diurnal variations, between cold and warm ocean variations and between

climate variations. Warm sea regions released CO_2 from the sea area and increased the concentration of the CO_2 atmosphere. In the cold sea areas between Iceland and Greenland, CO_2 was absorbed from the atmosphere by the sea. Takahashi had discovered that a higher sea temperature released more CO_2 into the atmosphere. CO_2 in the atmosphere was climate-driven, with air currents carrying CO_2 between different regional ocean areas. However, climate-driven CO_2 is not the same as a CO_2-driven climate. He discovered that CO_2 over the oceans acts as a dynamic system associated with marine ecosystems, cold and warm ocean currents, with circulation times from years to thousands of years. At the same time CO_2 in the atmosphere is a distribution system between sea areas, land, and ecosystems, in short and long circulation periods (Kunzig and Wallace 2008; Tansinez et al. 1990; Krajick 2019; Gruber et al. 2009).

1.4 Atlantic CO_2 variations 1826-1960

Ernst-Georg Beck was a German teacher of biology, of the old school, at the Merian Technical Grammar School in Freiburg and co-founder of the European Institute for Climate and Energy (EIKE). Beck began asking critical questions about the recorded CO_2 time-series at the Hawaiian volcano Mauna Loa. He considered warming of the Earth's atmosphere, due to an increase in CO_2 in the atmosphere, as impossible. At the same time, he believed that the CO_2 records at Mauna Loa could not be extrapolated linearly back to the 19th century, as has been done at Mauna Loa Observatory (Keeling et al. 1976).

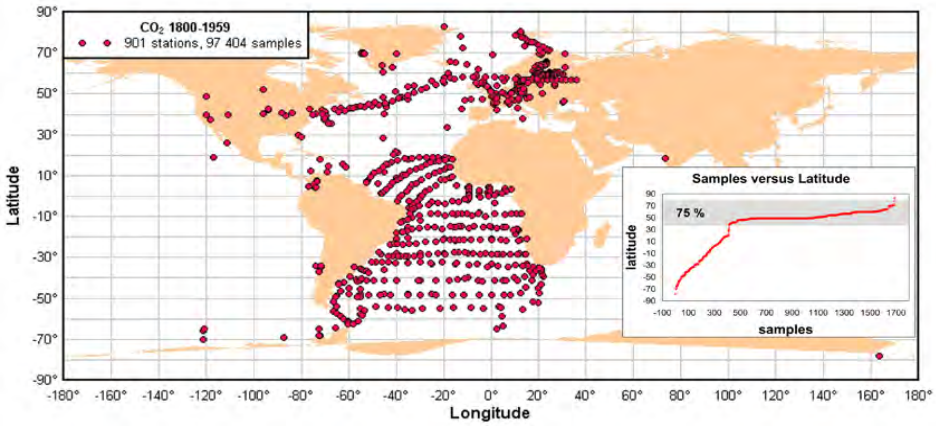

Figure 1: 901 sampling stations of direct measured CO_2 near ground 1800-1960 (Beck 2007).

Estimates of atmospheric CO_2 did not start with David Keeling and Takahashi. Chemical estimates of atmospheric CO_2 have been recorded since beginning of the 19th century. Callendar used previous CO_2 records from 1880 to 1930 to estimate a relation between global CO_2 and global warming. Seventy years later, Ernst Beck began estimating a new CO_2 time series based on previously published CO_2 time-series, most likely, including some of the same data, as used by Callendar (Anderson et al. 2016). In this extensive and highly impressive work, Beck conducted a review of approximately 100.000 CO_2 records from 901 recording stations (Fig. 1).

The result was published in 2007 (Beck 2007). In the Abstract Beck writes:" More *than 90,000 accurate chemical analyses of CO_2 in air since 1812 are summarized. The historic chemical data reveal that changes in CO_2 track changes in temperature, and therefore climate in contrast to the simple, monotonically increasing CO_2 trend depicted in the post-1990 literature on climate-change. Since 1812, the CO_2 concentration in northern hemispheric air has fluctuated exhibiting three high level maxima around 1825, 1857 and 1942 the latter showing more than 400 ppm."* This result questioned the Greenhouse paradigm in several ways. CO_2 was not accumulated in the atmosphere. There were large CO_2 fluctuations between 1826 and 1960.

Ralph F. Keeling, (son of David Keeling) responded. "*If Beck's contentions were true, they would overthrow 50 years of scientific advance and discovery. Unfortunately for Beck—as well as for humanity—the claims don't stand up. A historic perspective is useful. The modern era of CO_2 measurements effectively began with work by C. D. Keeling while he was a postdoc at the California Institute of Technology in the mid 1950's. It should be added that Beck's analysis also runs afoul of a basic accounting problem. Beck's 11-year averages show large swings, including an increase from 310 to 420 ppm between 1920 and 1945 (Beck's Fig. 11). To drive an increase of this magnitude globally requires the release of 233 billion metric tons of carbon to the atmosphere. The amount is equivalent to more than a third of all the carbon contained in land plants globally. Other CO_2 swings noted by Beck require similarly large releases or uptakes. To make a credible case, Beck needed to offer evidence for losses or gains of carbon of this magnitude from somewhere. He offered none. »* (Keeling 2007).

The time series from Beck showed that CO_2 had an unexpectedly strong growth between 1920 and 1945. Beck had not explained this CO_2 growth. A temporary CO_2 growth, which did not agree with the idea of accumulated CO_2 in the atmosphere, from combustion of fossil fuels. This led to questions about the credibility of the Atlantic CO_2 time series from Beck.

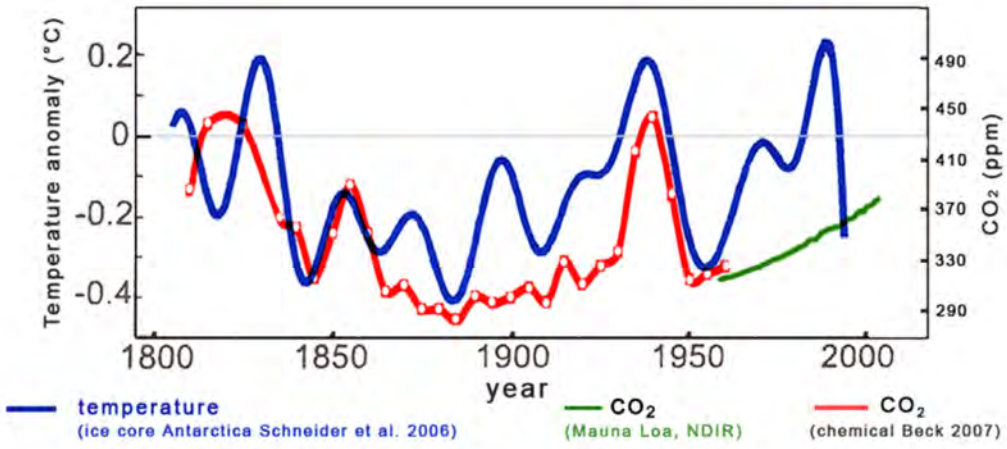

Figure 2: Atlantic CO_2 (1812-1961), Antarctic temperature (1812-1990), Mauna Loa atmospheric CO_2 (1960-2005) (Beck 2008b).

Beck responded to the criticism from Ralph Keeling (2007) with a discussion article in 2008 (Beck E. G. 2008b). Here he presents a figure that shows a reasonably good agreement between CO_2 and temperature changes in Antarctica from ice core samples (Fig. 2). The Mauna Loa CO_2 showed a slow growth, without large fluctuations. This close relation between Atlantic CO_2 and Antarctic temperature estimates was published in December 2008.

In 2008 a wavelet spectrum analysis of the North Atlantic water (NAW) inflow from 1900 to 2007 (Yndestad et al. 2008) was published. This paper revealed a close relation between (NAW) and CO_2 growth between 1930 and 1950. In this paper Beck found the explanation for the unexpected CO_2 growth in the atmosphere during this period. Temperature variations in Atlantic water released large amounts of CO_2 into the atmosphere. The unknown source of CO_2 growth coincided with temperature variations in the North Atlantic Ocean. In 2009 Beck started to work on an updated manuscript. In this manuscript, he adds a review of estimate variations, and selected the most reliable data and explained the CO_2 growth from 1920 to 1945.

The manuscript was submitted for publication in August 2010 (Beck February 2010). In the discussion Beck writes: *"Using a Savitzky-Golay smoothed curve with a higher moving window*

width of 7 to correct problems around 1880 and 1930. Observed a periodic cycling with maxima at: 1836: 343,9 ppm; 1857: 334,2 ppm; =1878: 309,7 ppm; 1896: 312 ppm; 1915: 320,7 ppm; 1941: 371,4 ppm. The average period is 21 years (21, 21, 18, 19, 26 years).

The sharp drop in 1922 and the changing period length at those times points to phase change in the time series supports the findings of Yndestad in the NAW (Northern Atlantic water temperature) [Yndestad et al. 2008], evidence for the lunar nodal cycle and its harmonics as the controlling forces behind the northern and Arctic climate"…"Since 1870 two periods of about 60-70 years (1870-1940) and 1949 -2009 can be observed with such a slowly rise of the CO_2 levels to a maximum level of about + 70 ppm in about 1943 and today. The overall rising CO_2 levels since 1870 to today has been also supported by the reconstructed ice core data despite of its much worse resolution compared to the presented data (see fig. 25). The maxima around 1860, 1940 contrast with the published literature. They can be described by an about 70-80-year cycle". Beck died of cancer in September 2010. The manuscript was rejected for publication on November 15, 2010. The last reviewer comment was "*I must categorically advise rejection of this paper without possibility of resubmission or revision"* (Beck 2007; Harro A.J. Meiyer. 2007; Keeling R.F. 2007; Beck E. G. 2008a; Beck E. G. 2008b; Massen, Francis and Beck E. G. 2011; Keeling R.F. 2007; Beck E. G. February 2010; Ernst-Georg Beck's scientific contributions. ResearchGate).

Taro Takahashi and Ernst Beck argued that CO_2 variations in the atmosphere were controlled by sea surface temperature. This can be verified by computing the variability signature atmospheric CO_2 and global sea surface temperature. In 2008, a wavelet spectrum analysis of North Atlantic Water from the year 1900 was published (Yndestad et al. 2008). The analysis confirmed a coincidence between Atlantic CO_2 and sea surface temperature variations in the period 1930-1960. This analysis confirmed the last part of the data series for Beck, and it explained the 1930-1950 CO_2 bubble. In 2022 there was published a wavelet spectrum analysis global sea surface temperature variability from 1850 to 2020. The wavelet spectrum revealed a coincidence to the lunar nodal tide spectrum signature (Yndestad 2022). The implication of a lunar nodal spectrum in global sea temperature variations is that the sea temperature variations are controlled by the lunar nodal tide, which is not controllable. This study investigates the Mauna Loa CO_2 variability signature from 1959 and Atlantic CO_2 variability signature from 1850 to 1960.

2. Materials and methods

2.1 Materials

The Mauna Loa CO_2 time series, shown on Fig. 3 covers the period 1958 to 2021, representing the longest continuous recording of direct atmospheric CO_2 measurements. Data are recorded at an altitude of 3400 m in the northern subtropics, which is not identical to the global average CO_2 concentration at the surface. The time series is monitored by the NOAA Global Monitoring Laboratory (https://gml.noaa.gov/ccgg/trends/data.html). The red graph shows annual seasonal variations around an average annual CO_2 growth that apparently has an exponential growth (Fig. 3). The source of annual seasonal variations is believed to be seasonal variations from photosynthesis in nature. The overall increase in CO_2 from 1958 has been associated with accumulation of CO_2 from fossil fuels. The Atlantic CO_2 time series is based on Beck (2022; https://doi.org/10.53234/scc202206/20).This time series covers records from the Atlantic Ocean and Northern Europe. The time series covers the period 1826 to 1960, estimated from selected 97 404 selected samples from 901 stations compiled in 87 data files (Beck 2022). The sea surface temperature (SST) time series (HadSST3) consists of anomalies on a 5°-by-5° global grid and is published by the Climatic Research Unit. The SST signature is computed in (Yndestad 2022). (For SST, see https://www.metoffice.gov.uk/hadobs/hadsst3/).

2.2 Methods

A wavelet analysis provides temporal, cycle period and cycle phase information in time series. The wavelet spectrum transform is based on a correlation between a time series and a bell-shaped wavelet pulse s(t) that moves along the time axis of the time series t = [first…last]. You then get a large numeric value where you have a match between the wavelet pulse and periodic changes in the time series. By changing the pulse width, one can identify all the periodic changes in the time series. Cycle periods and cycle phase relations are identified in the wavelet spectra by the continuous wavelet transform:

$$W_{a,b}(t) = \frac{1}{\sqrt{a}} \int_R \; x(t)\, \Psi\left(\frac{t-b}{a}\right) dt \tag{1}$$

where x(t) is the analyzed temperature time series after being scaled to zero mean value and scaled by variance. In the present case, Ψ() is a coif3 wavelet impulse function. $W_{a,b}(t)$ is a set of wavelet cycles, b is the translation in time, and a is the time-scaling parameter in the wavelet transformation (Daubechies 1992; MATLAB, 2020), which is in this case performed as a discrete wavelet transform. In this analysis, the time translation b = 0, and the computed wavelet transform, $W_a(t)$, represents a moving correlation between x(t) and the impulse function Ψ() over the entire time-series x(t). The moving correlated wavelets, s(t), are collected into a wavelet spectrum, W(s, t), for t = [first…last] (yr.) and s = [1…(last-first)/2] (yr.), to comply with the sampling theorem. Stationary cycles are identified by computing the autocorrelation of the wavelet spectrum W(s, t), as follows:

$$WA(R(s), m) = E[W(s, t)W(s, t + m)], \tag{2}$$

where WA(R, T) represents a set of maximum correlation values R = [max 1…max n] with the dominant cycles T = [T1…Tn] (yr.).

2.3 Scientific approach

A CO_2 time series has a spectrum signature: $S_{co2}(T_{co2}, F_{co2})$, where T_{co2} represents a set of stationary CO_2 cycle periods and F_{co2} represents CO_2 cycle phase relations (min/max). Global Sea Surface Temperature (SST) has a spectrum signature $S_{sst}(T_{sst}, F_{sst})$, where T_{sst} represents a set stationary SST cycle periods and F_{sst} represents a set of cycle phase relations. The CO_2 spectrum signature and the SST spectrum signature have a relation:

$$S_{co2}(T_{co2}, F_{co2}) = S_{sst}(T_{sst,} F_{sst}) + S_{err}(T_{err}, F_{err}), \tag{3}$$

where $S_{err}(T_{err}, F_{err})$ represents a spectrum from an unknown source. A CO_2 signature $S_{co2}(T_{co2}, F_{co2})$ coincides with the Sea Surface Temperature (SST) signature, $S_{sst}(T_{sst}, F_{sst})$, if: $S_{co2}(T_{co2}, F_{co2}) = S_{sst}(T_{sst}, F_{sst})$. The CO_2 signature, $S_{co2}(T_{co2}, F_{co2})$, has a π/2 (rad) phase lag if: $S_{co2}(T_{co2}, F_{co2}) = S_{sst}(T_{sst}, F_{sst} + T_{sst}/4)$.

3. Results

3.1. Mauna Loa CO_2 variability 1959-2021

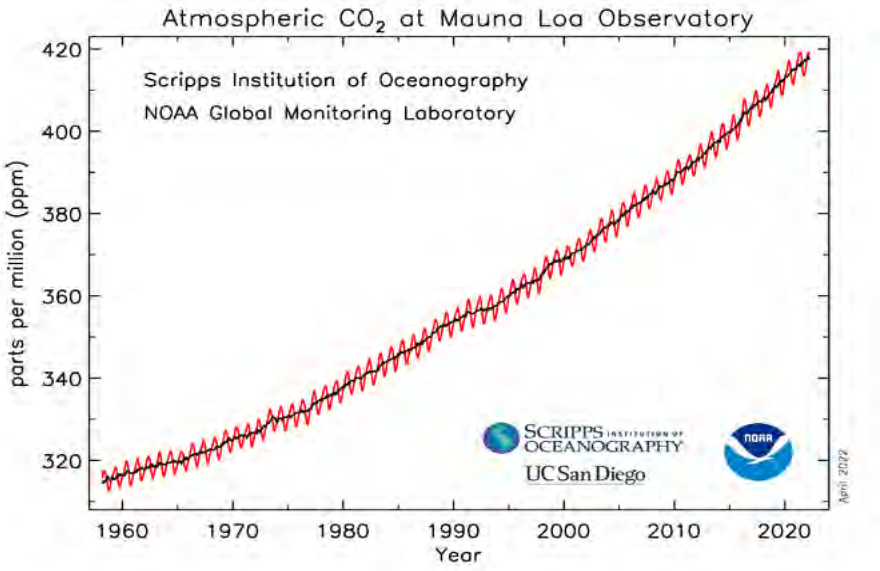

Figure 3: Mauna Loa, Hawaii, recorded atmospheric CO_2 (ppm) for the years t = 1959...2021.

Records of CO_2 from 1959 to 2021 at Mauna Loa, Hawaii is shown on Fig. 3. The CO_2 level appears to have an exponential growth. This exponential growth must have a source. Possible sources are emission from fossil fuels and net outgassing of CO_2 from the oceans. The CO_2 time series covers a period of 62 years. In this short time-period, CO_2 has grown by 100 ppm and global temperature has grown by 0.6 degrees C. The CO_2 growth at Mauna Loa is time-variant. The growth has a minimum in the cold climate period during the 1960´s and a maximum growth in the warm climate period close to 2020. The time-variant growth rate signature may reveal the source of the Mauna Loa CO_2 variations.

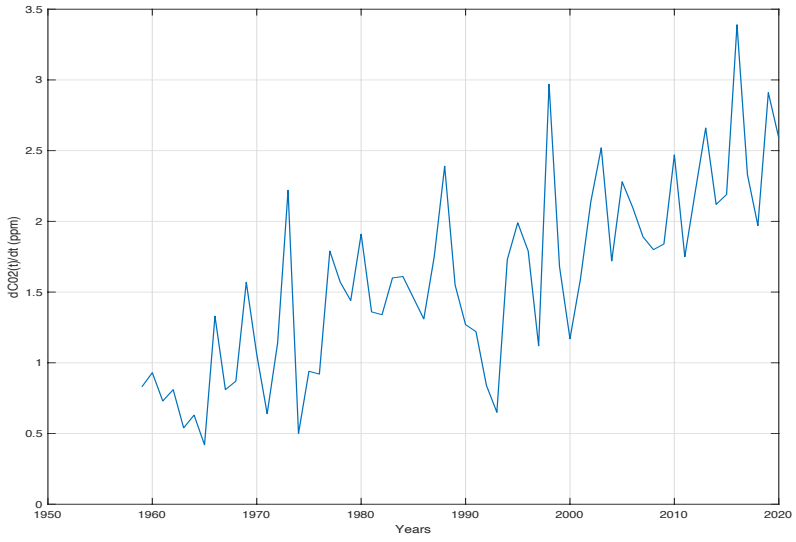

Figure 4: Annual Mauna Loa CO_2 growth rate, dCO_2/dt, for the years t = [1959...2020].

The Mauna Loa CO_2 time series has an annual growth rate $dCO_2(t)/dt = (CO_2(t) - CO_2(t-1))/dt$, for the period t = [1959, 1960...2020] (Fig. 4). It appears from Fig. 4 that the CO_2 growth rate,

$dCO_2(t)/dt$, began to increase from about 1965 and reached a maximum close to 2016 The growth rate, $dCO_2(t)/dt$, has a minimum close to the cold period in the 1960s and stabilized to a maximum when global sea temperature has a maximum from about the year 2010 (Yndestad 2022). At the same time, the growth rate (Fig. 4) has some large fluctuations.

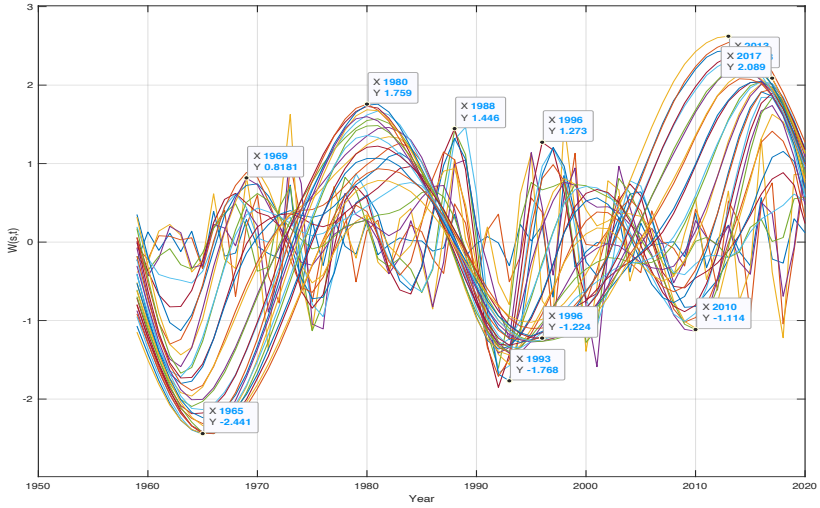

Figure 5: Wavelet spectrum, $W_{co2\text{-}m}(s, t)$, from Mauna Loa in CO2 growth (dCO_2/dt) for t = [1959…2021] and s = [1…30]. The wavelet spectrum reveals cycle periods in annual Mauna Loa CO2 growth rate (Fig. 4).

The fluctuation source is revealed by computing the signature in the wavelet spectrum [Eq.1]. The Mauna Loa time series has 62 samples, which may represent periods up to 31 years. Fig. 5 shows the computed wavelet spectrum $W_{co2\text{-}m}(s, t)$ of Mauna Loa CO_2 growth rate $dCO_2(t)/dt$ when t = [1959…2021] and s = [1…30]. The computed wavelet spectrum has min/max variations for: $W_{co2\text{-}m}$(s = min/max, t) = [(-1.64, 1965), (-0.0, 1973), (1.8, 1980), (+0.0, 1988), (-1.2. 1995), (-0, 2004), (2.5, 2013)] at intervals of [8, 7, 8, 7, 9, 9] (yr.), which has a mean cycle period of $T_{co2\text{-}m}$ = 32 years.

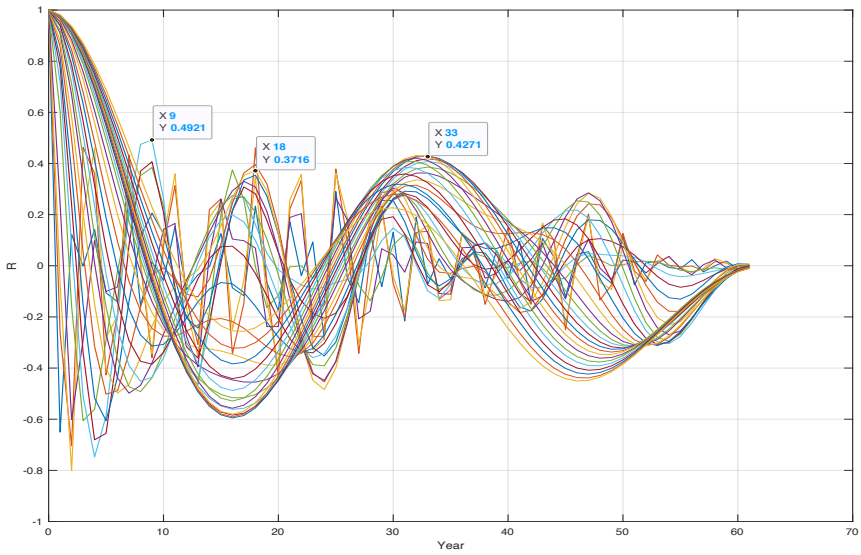

Figure 6: Autocorrelations, $WA_{co2\text{-}m}(R(s), m)$, of Mauna Loa CO_2 wavelet spectrum, $W_{co2\text{-}m}(s, t)$, for s = [1…60] and m = [1…60].

Stationary periods in the wavelet spectrum, $W_{co2\text{-}m}(s, t)$, (Fig. 6) are estimated by computing the autocorrelation of all wavelets in the wavelength spectrum $W_{co2\text{-}m}(s, t)$ [Eq. 2]. The computed wavelet autocorrelation spectrum, $W_{aco2\text{-}m}(R(s), m)$, for the wavelet spectrum: $W_{co2\text{-}m}(s, t)$, have maximum correlations at: $WA_{co2\text{-}m}(R(max), T_{co2\text{-}m}) = [(0.5, 3), (0.5, 9), (0.4, 18), (0.42, 33)]$ (Fig. 6), where the maximum correlation $R(max) = [0.5, 0.5, 0.4]$ to the stationary periods: $T_{co2\text{-}m} = [3, 9, 18, 33]$ (yr.).

CO_2 and SST signature coincidence

Global Sea Surface temperature (SST) has a coincidence to the lunar nodal spectrum: $T_{sst} = [1/3, 1, 2, 3]18.61/2 = [3.1, 9.3, 18.6, 27.9]$ (yr.) (Yndestad 2022). The coincidence difference between identified stationary CO_2 growth rate periods, $T_{co2\text{-}m}$, and lunar forced SST periods, T_{sst}, is: $[T_{co2\text{-}m} - T_{sst}] = [0, 0, 0, 5]$ (yr.), which reveals a direct coincidence between identified CO_2 growth rate periods and deterministic lunar nodal periods. The global sea surface temperature wavelet spectrum, $W_{sst}(s, t)$, has computed phase shifts at the years: $W_{sst}(s = min/max/0, t) = [(+0, 1960), (-3.9, 1977), (-0, 1993), (5.1, 2008)]$ (Yndestad 2022).

The phase difference: $[W_{sst}(s = min/max/0, t) - W_{co2\text{-}m}(s = min/max/0, t)] = [(+0, 1960), (-3.9, 1977), (-0, 1993), (5.1, 2008)] - [(-1.65, 1964), (-0\ 1973), (-1.2, 1995), (-0, 2004)] = [4, 4, 2, 4]$ years, reveals that CO_2 growth rate, $dCO_2(t)/dt$, has a $\pi/2$ (rad) phase lag from global sea temperature variations. Warmer sea surface temperature causes more rapidly accumulation of CO_2 in the atmosphere.

3.2. Atlantic CO_2 variability 1826-1960

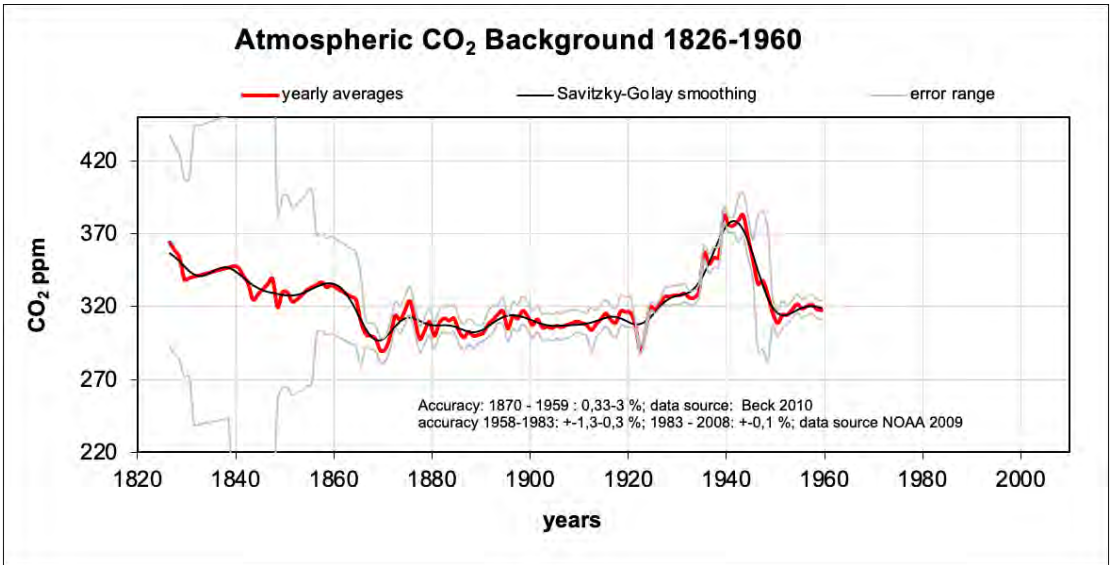

Figure 7: Beck CO_2 time series 1826-1960, (Beck February 2010, Beck 2022, Supplemental data No. 2. https://doi.org/10.53234/scc202206/20)

Estimated CO_2 for the period 1826 to 1960 is shown on Fig. 7. About 75 % of the samples were collected between latitudes of 40 and 80 N, about 50 % over sea surface or from the sea at coasts (Beck February 2010; Beck 2022). The data series is estimated from more than 200 000 single samples in about 400 historical papers from 1800 to 1960 (Beck February 2010). The Mauna Loa time series (Fig. 3) has an exponential growth from 1960. The Atlantic CO_2 time series starting in 1826 is different. The CO_2 levels are dropping from 1826 to a minimum around 1870, continued to grow from 1930 to a temporary maximum around 1940 and a new temporary minimum in 1950. The CO_2 growth in this period was questioned by Ralph Keeling (Keeling 2007). The CO_2 estimates are not accurate from 1826 to 1870. From 1870 the accuracy is

estimated to 3%. The total time series covers a total period of 134 years, which may represent a period up to 67 years.

3.3 Atlantic CO_2 wavelet spectrum from 1826 to 1960

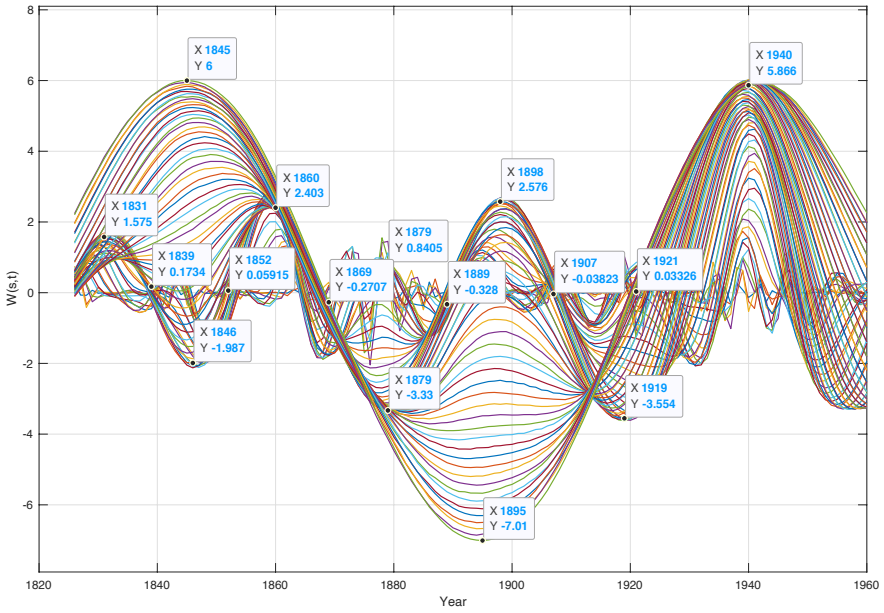

Figure 8: Wavelet spectrum, $W_{co2\text{-}a}(s, t)$, of Atlantic surface CO_2 (Beck E.G. February 2010) for $s = [1...70]$ in the years $t = [1826...1960]$.

The computed wavelet spectrum of Atlantic surface CO_2 (Beck E.G. February 2010) (Fig. 8) for s = [1...70] in the years t = [1826...1960]. The long envelope period in the wavelet spectrum (Fig. 8) has minima, maxima, and phase shifts at the years: $W_{co2\text{-}a}$(s = min/max/0, t) = [(6.0, 1845), (+0.0, 1868), (-7.0, 1895), (-0.0, 1921), (5.8, 1940)] in a total period of 95 years. The next part of the wavelet spectrum (Fig. 8) has phase shifts at: $W_{co2\text{-}a}$(s = min/max/0, t) = [(1.6, 1831), (+0, 1839), (-2.0, 1846), (-0.0, 1852), (2.4, 1860), (+0.0, 1868), (-3.3, 1879), (-0.0, 1889), (2.6, 1898), (+0.0, 1907), (-3.5, 1919), (-0.0, 1929), (2.5, 1940)], in a mean period of 36 years. The estimated 36-year wavelet cycle, $W_{co2\text{-}a}$(s = 36, t), coincides with lunar nodal periods of 2*18.6 = 37.2 years. The 95-year wavelet, $W_{co2\text{-}a}$(s = 95, t), coincides with a lunar nodal period of: 5*18.6 = 93.0 years. The CO_2 growth between 1930 and 1950 coincides with a constructive interference between the stationary lunar nodal cycles of 37.2 and 93.0 years. In this period the lunar nodal cycle has a direct relation to global sea temperature variations.

Computed upcoming minima and maxima

A stationary lunar forced 2*18.6 = 37.2-year period is expected to have upcoming minima, maxima and phase shifts at the years: $W_{co2\text{-}a}$(s = 37.2, min/max/0, t) = [(min, 1811), (max, 1829), (min, 1848), (max, 1866), (min, 1884), (max,1903), (min, 1922), (max, 1940), (min, 1959), (-0, 1968), (max, 1977), (+0, 1986), (min, 1996)…(-0, 2005), (max, 2014), (+0, 2023), (min, 2033)]. The stationary 93.0-year lunar forced period is expected to have phase shifts at the years: $W_{co2\text{-}a}$(s = 93.0, min/max/0, t) = [(6.0, 1845), (+0.0, 1868), (-7.0, 1895), (-0.0, 1921), (5.8, 1940), (+0, 1963), (min, 1986), (-0, 2009), (max, 2033), (+0, 2056)]. The stationary dominant periods have destructive interference from 1826-1930, constructive positive interference from 1930-1950, destructive interference from 1950-1987 and growth from 1987-2022. The computed CO_2 growth from 1987-2022, coincides with global sea surface temperature growth (Yndestad 2022) and CO_2 growth at Mauna Loa (Fig. 4).

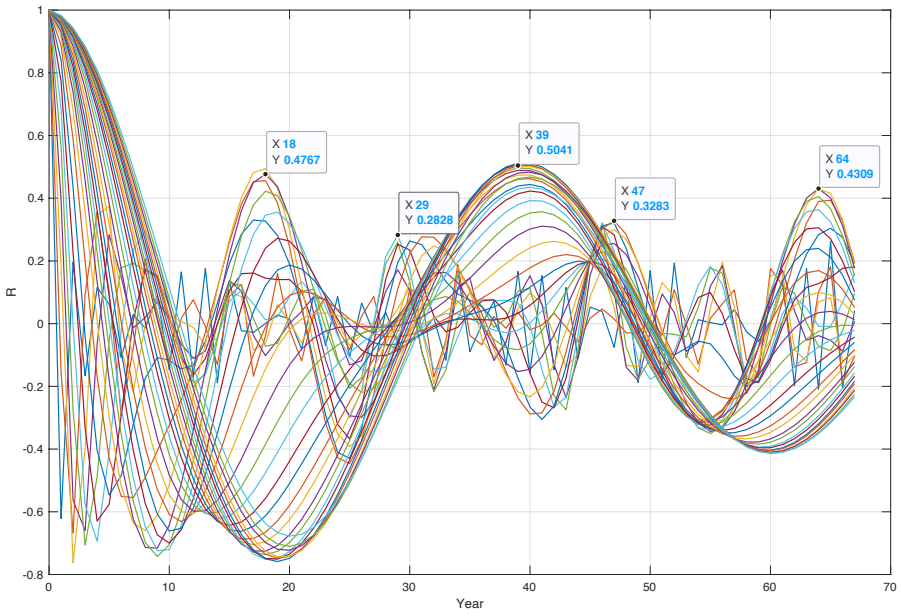

Figure 9. Autocorrelations, $WA_{co2\text{-}a}(R(s), m)$, of wavelet spectrum, $W_{co2\text{-}a}(s, t)$, for annual background growth in CO_2 (Beck 2010) for s = [1...70] and m = [1...67].

Stationary CO_2 periods in the wavelet spectrum, $W_{co2\text{-}a}(s, t)$, (Fig. 8) are estimated by computing the autocorrelation of all wavelets in the wavelet spectrum. The computed autocorrelations, $WA_{co2\text{-}a}(R, m)$ (Fig. 9), for the wavelet spectrum, $W_{co2\text{-}a}(s, t)$, have maximum correlations in the following periods: $WA_{co2\text{-}a}(R(max), T_{co2\text{-}a}) = [(0.3, 9), (0.47, 18), (0.26, 29), (0.5, 39), (0.3, 47), (0.4, 64)]$, which represents the correlations: R = [0.3, 0.47, 0.26, 0.50, 0.3, 0.4] to the periods: $T_{co2\text{-}a}$ = [9, 18, 29, 39, 47, 64] (yr.). Lunar nodal forced SST cycles have a spectrum: T_{sst} = [1, 2, 3, 4, 5, 7]18.6/2 = [9, 18.6, 27.9, 37.2, 46.5, 65.1] (yr.) (Yndestad 2022). The coincidence difference between estimated $T_{co2\text{-}a}$ cycle periods and lunar nodal forced SST cycles are: $[T_{co2\text{-}a} - T_{sst}]$ = [0, 0, 2, 0, 0, 1] (yr.), or a mean difference of 0.5 years.

3.4 Atlantic CO_2 and SST signature coincidences

Global sea surface temperature variability has a stationary period spectrum: T_{sst} = [18, 29, 39, 64, 74] (yr.), in coincides with the lunar nodal spectrum T_{ln}. The coincidence difference between stationary global sea surface periods, T_{sst}, and Atlantic CO_2 periods is: $[T_{sst} - T_{co2\text{-}a}]$ = [0, 0, 0, 0, 19] (yr.). The 19-year difference indicates that the average error from 1826 to 1870 has introduced a period shift from a 74-year period to a 93-year period in estimated Atlantic CO_2 variability. The SST has phase shifts at the years: $W_{sst}(s = min/max/0, t) = [(+0, 1897), (+0, 1960), (-0, 1993), (5.1, 2008)]$ (Yndestad 2022; Yndestad et al. 2008). The stationary 36-year Atlantic CO_2 periods has a minimum and maximum at: $W_{co2\text{-}a}(s = 36, t) = [(2.6, 1898), (-3.6, 1960)]$, which reveals a $\pi/2$ (rad) phase lag from global sea surface variations to Atlantic CO_2 variations. The extended stationary CO_2 period $W_{co2\text{-}a}(s = 37.2, t)$ has phase shifts at the years; $W_{co2\text{-}a}(s = 37.2, min/max/0, t) = [(max, 1940), (+0, 1949), (min, 1959), (-0, 1968), (max, 1977), (+0, 1987), (min, 1996), (-0, 2005), (max, 2015)]$. The phase difference between the lunar driven SST period and the lunar driven CO_2 period is: $[W_{sst}(s = min/max/0, t) - W_{co2\text{-}a}(s = min/max/0 - \pi/2 (rad), t)] = [1, 1, 3, 3]$ (yr.), which has a mean difference of only 2 years. Stationary Atlantic CO_2 periods has a $\pi/2$ (rad) phase lag from stationary Global Sea Surface periods from 1870 to 2020. Atlantic CO_2 growth rate has a maximum when SST has a maximum amplitude.

3.5 Mauna Loa CO_2 coincidences

The Mauna Loa CO_2 growth rate, dCO_2/dt, has period phase shifts at: $W_{co2\text{-}m}(s = min/max/0, t)$ = [(-1.64, 1965), (-0.0, 1973), (1.8, 1980), (+0.0, 1988), (-1.2, 1995), (-0, 2004), (2.5, 2013)]. The Atlantic 37.2-year CO_2 period has phase shifts at the years: $W_{Co2\text{-}a}(s = 37.2, min/max/0, t)$ = [(max, 1940), (+0, 1949), (min, 1959), (-0, 1968), (max, 1977), (+0, 1987), (min, 1996), (-0, 2005), (max, 2015)]. The phase difference between Mauna Loa CO_2 growth rate and extended Atlantic CO_2 periods is: $[W_{C02\text{-}m}(s = min/max/0, t) - W_{co2\text{-}a}(s = 37.2, min/max/0, t)]$ = [3, 4, 1, 1, 2] (yr.), which has a mean difference of only 2.2 years.

4. Discussion

4.1 Chemical-based CO_2 recordings

Monitoring atmospheric CO_2 started early in the 1800's by a chemical-based method. This was probably an expensive and time-consuming method that required special knowledge. Beck (February 2010) claimed that the chemical-based method was accurate, where error deviation was less than 3%. It looks like it took a few years before chemical monitoring of atmospheric CO_2 was established according to a unified best practice.

Callendar created a CO_2 time series from 1880 to 1932 based on published CO_2 measurements from different parts of the globe. The selected records were limited to publications he trusted (Thomas et al. 2016). When Beck developed his Atlantic CO_2 time series, he selected previous publications from 1826 to 1960. In the manuscript Beck (February 2010), it appears that Beck rejected some CO_2 publications he did not trust. In retrospect, it has been questioned why some early publications were rejected. Beck calculated uncertainty for each individual year (Fig. 7). This uncertainty is related to variations around a mean estimate. It appears from the figure that the time series has large variations from 1826 to 1870. In the period 1870 to 1960, the variation is about 3%. These variations indicates that the time series is reliable from 1870 to 1960.

4.2 Mauna Loa CO_2 recordings

The Mauna Loa CO_2 records from 1959 were based on infrared spectrometry. This method is obviously a faster, cheaper, and more stable method than records from chemical-registrations. Whether this was a more accurate measurement method is however unclear. Mauna Loa CO_2 records from 1959 became the new standard for recording atmospheric CO_2. In 2009, Ernst Beck came up with an unknown CO_2 atmospheric time series. A time series based on 100,000 CO_2 atmosphere records from 1826 until 1960. Beck points out that Keeling did not have CO_2 data before 1959. He also questions the Greenhouse effect and claims that more heat must be added to release more CO_2 into the atmosphere. Humlum et al. (2013) published an estimated 11–12-month phase lag from global sea surface temperature variations to atmospheric CO_2 variations (Humlum et al. 2013). This estimate supports a temperature-driven CO_2 variation.

The Mauna Loa CO_2 time series from Keeling and the Atlantic CO_2 time series from Beck are the only known long continuous CO_2 atmosphere records. This study therefore is of utmost importance for identifying the relation between CO_2 variability and climate variability. The challenge is that the time series are recorded by different methods, at different geographical positions on Earth. The results from this study have revealed that the time series are not really that different. Variations in CO_2 at Mauna Loa CO_2 and variations in Atlantic CO_2 have the same signature which reveals a variability that has the same source.

Taro Takahashi's records showed that CO_2 had large variations over sea areas on the globe. Atmospheric CO_2 is growing from the sea close to the warm equator and absorbed into the sea in cold Arctic areas. Atlantic CO_2 and Mauna Loa CO_2 looks different because the sea temperature increased in the period 1975 to 2000. Atlantic CO_2 captures regional variations more strongly than recorded CO_2 at an altitude of 3000 meters. Now the NOAA Global

Monitoring Laboratory also confirms that records of CO_2 on Mauna Loa are not the same as global CO_2.

4.3 The Mauna Lua CO_2 signature 1960-2020

This study investigates the coincidence between Mauna Loa CO_2 growth and Atlantic CO_2 density. The wavelet spectrum of CO_2 growth at Mauna Loa coincides with the signature of global ocean surface temperature and the lunar nodal tide signature (Table 1). This coincidence reveals a direct relationship between Mauna Loa CO_2 variability, global surface temperature variability and the lunar nodal tide. CO_2 growth variations at Mauna Loa, have a $\pi/2$ (rad) phase lag from global temperature variations. The phase lag reveals that higher global surface temperatures in the ocean, leads to higher speed in outflow of CO_2 from oceans and into the atmosphere. Variations in the global sea temperature, thus causes CO_2 variations in the atmosphere. The exponential CO_2 growth at Mauna Loa, is caused by global warming from 1975 to 2020. The signature of CO_2 growth also coincides with the signature of the lunar nodal tide. This signature has the periods of T_{ln} = [1/3, 1, 2, 3]18.61/2 years. The lunar nodal time has a spectrum of deterministic periods up to 446 years (Yndestad 2022). When the CO_2 signature coincides with the global sea surface temperature signature and the lunar nodal tide signature, it reveals that CO_2 growth at Mauna Loa is not controllable.

4.4 The Atlantic CO_2 signatures 1870-1960

The wavelet spectrum of Atlantic CO_2 from 1870 to 1960 confirms a direct connection between Atlantic CO_2, global sea surface temperature variations and the lunar nodal tide. The signature of Atlantic CO_2 has dominant lunar node periods of: $T_{co2\text{-}a}$ = [1, 2, 4]18.6 years. Atlantic CO_2 variability is controlled by the global ocean surface temperature variability and lunar nodal tide spectrum. The global sea surface temperature signature and the Atlantic CO_2 signature have a phase difference of $\pi/2$ (rad). This phase difference confirms that a maximum sea temperature, leads to a maximum speed in CO_2 outflow from the sea and into the Earth´s atmosphere. Variations in Atlantic CO_2 from 1870 to 1960 coincide with variations in Mauna Loa CO_2 from 1960. This coincidence confirms that both CO_2 time series are controlled by the same source.

Ralph Keeling questioned the CO_2 growth from 1930 to 1950. The wavelet spectrum analysis reveals that this growth coincides with global ocean surface temperature variations controlled by constructive interference between the 2*18.6 = 37.2 years lunar forced SST period and the 4*18.6 = 74.4 years lunar forced SST period. A continuation of the temperature period of 37.2 years, from 1940 to 2020, reveals that changes in Atlantic CO_2 and Mauna Loa CO_2 have the same period and phase relations. The phase difference is only 2 years. This close relation confirms that Atlantic CO_2 variations and Mauna Loa CO_2 variations have the same source.

The lunar nodal signature in sea surface temperature variations, is controlled by vertical mixing in oceans. Cold bottom water is mixed with surface water heated by the sun. The lunar nodal tide is a standing wave that has maximum amplitude at equator and the pole. The lunar tide thus introduces its signature in sea surface temperature variability. This vertical mixing in the oceans, may be a possible source of releasing more CO_2 from deep water into the atmosphere. Global sea surface temperature has an identified lunar nodal powered spectrum up to 446 years. Sola-forced periods influences the long sea temperature growth from 1896 to 2020 (Yndestad 2022). In this study the two CO_2 data series are too short to identify the long solar-forced period.

A study of glaciological characteristics of the Antarctic Ice Core (Ahn et al. 2012), identified a higher CO_2 density level in the warm climate period 1000-1200 and a lower CO_2 level in the cold period 1450 to 1800. This confirms that CO_2 in the atmosphere follows long-term global temperature variations. Global sea temperature is expected to continue to grow steadily until about 2025-2030. Thereafter, a new cooling period is expected in the future, to a deep minimum of approximately the year 2070 (Yndestad 2022). This means that we may expect that an accelerating CO_2 growth will continue towards the year 2030. When global ocean temperatures

are reduced to a minimum in 2070, the CO_2 emission growth from the oceans into the atmosphere is expected to be reduced.

5. Conclusion

This study investigates atmospheric CO_2 variability signatures. The study is based on a wavelet spectrum analysis of Atlantic CO_2 record for the period 1826 to 1960 and the Mauna Loa CO_2 records from 1959 to 2020. Together, the CO_2 records cover a total period of 200 years. The study has revealed that:

1. Atlantic CO_2 signature from 1826-1960 coincides with the Mauna Loa atmospheric CO_2 growth variability signature, the global sea surface temperature variability signature, and the lunar nodal tide variability signature. This is strong evidence of a lunar forced atmospheric CO_2 variations.
2. Atmospheric CO_2 variations have a maximum growth rate when global sea surface temperature variations have a maximum state. The $\pi/2$ (rad) phase lag between global sea temperature variations and atmospheric CO_2 variations, reveals that atmospheric CO2 variations are controlled by global sea temperature variations.
3. The CO_2 variability signature coincides with the lunar nodal tide signature. The lunar nodal tide spectrum reveals a chain of events from a lunar nodal tide variation to global sea surface temperature variations and atmospheric CO2 variations.
4. A lunar nodal tide spectrum in atmospheric CO_2 growth reveals that CO_2 is not controllable.

Global sea temperature variability has lunar forced periods up to 446 years and solar forced periods up to 4450 years (Yndestad 2022). The same solar forced periods and lunar forced periods are expected to be revealed in longer CO_2 time series.

Table 1. Identified signature of atmospheric Mauna Loa CO_2 growth, atmospheric Atlantic CO_2, Global Sea surface temperature and lunar nodal tide periods.

	Global Sea Surface temperature signature (SST)
Stationary SST periods (yr.)	T_{sst} = [9, 18, 28, 29, 37, 46, 57, 64, 74] (yr.)
Lunar nodal periods	$T_{ln}/2$ = [9.3, 18.6, 27.9, 37.2, 46.5, 55.8, 65.1, 74.4] (yr.)
Wsst(s, min/max/0, t)	[(-2.2, 1860), (-0, 1872), (2.2, 1883), (+0, 1897) (-3.1, 1912), (-0, 1927), (3.0, 1943), (+0, 1960), (-3.9, 1977), (-0, 1993), (5.1, 2008)]
	Mauna Loa CO_2 growth signature (dCO_2m/dt) 1959-2020
Stationary periods	$T_{co2\text{-}m}$ = [3, 9, 332] (yr.)
Lunar nodal periods	T_{ln} = [1/3, 1, 2, 3]18.61/2 = [3.1, 9.3, 18.6, 27.9] (yr.).
$W_{co2\text{-}m}$(s, min/max/0, t)	[(-1.64, 1965), (-0.0, 1973), (1.8, 1980), (+0.0, 1988), (-1.2, 1995), (-0, 2004), (2.5, 2013)]
	Atlantic CO_2 signature 1826-2020
Stationary periods:	$T_{co2\text{-}a}$ = [9, 18, 29, 39, 47, 64] (yr.)
Lunar nodal periods	T_{ln} = [1, 2, 3, 4, 5, 7]18.6/2 = [9, 18.6, 27.9, 37.2, 46.5, 65.1] (yr.)
$W_{co2\text{-}a}$(s, min/max/0, t)	[(1.6, 1831), (+0, 1839), (-2.0, 1846), (-0.0, 1852), (2.4, 1860), (+0.0, 1868), (-3.3. 1879), (-0.0, 1889), (2.6, 1898), (+0.0, 1907), (-3.5, 1919), (-0.0, 1929), (2.5, 1940)]
$W_{co2\text{-}a}$(s=37.2, min/max/0, t)	[(min, 1811), (max, 1829), (min, 1848), (max, 1866), (min, 1884), (max,1903), (min, 1922), (max, 1940), (min, 1959), (-0, 1968), (max, 1977), (+0, 1986), (min, 1996)… (-0, 2005), (max, 2014), (+0, 2023), (min, 2033)].
$W_{co2\text{-}a}$(s= 93.0, min/max/0, t)	[(6.0, 1845), (+0.0, 1868), (-7.0, 1895), (-0.0, 1921), (5.8, 1940), (+0, 1963), (min, 1986), (-0, 2009), (max, 2033), (+0, 2056)].
$W_{co2\text{-}a}$(s = 74.4, min/max, t)	[(max, 1866), (min, 1902), (max, 1940), (min, 1977), (max, 2014)]

Nomenclature

Atlantic CO_2 wavelet spectrum: $W_{co2\text{-}a}(s, t)$
Atlantic CO_2 wavelet autocorrelation spectrum: $WA_{co2\text{-}a}(R, T_{co2\text{-}a})$
Atlantic CO_2 stationary periods: $T_{co2\text{-}a}$
Cycle period spectrum: $T = [T_1, T_2, T_3 \ldots T_n]$
Coincidence cycle periods: $A*T_1 = B*T_2$
Global Sea Surface temperature: SST
Global Sea Surface temperature period spectrum: T_{sst}
Global Sea Surface temperature wavelet spectrum: $W_{sst}(s, t)$
Global Sea Surface temperature wavelet spectrum: $W_{sst}(s, t)$
Lunar nodal cycle periods: T_{ln}
Mauna Loa CO_2 stationary periods: $T_{co2\text{-}m}$
Mauna Loa CO_2 growth rate: $dCO_2(t)/dt$
Mauna Loa CO_2 wavelet autocorrelation spectrum: $WA_{aco2\text{-}m}(R, T_{co2\text{-}m})$

References

Ahn Jinho, Brook Logan Mitchell, Rosen Julia, McConnell Joseph R.. Taylor Kendrick, Etheridge David, and Rubino Mauro, 2012: *Atmospheric CO2 over the last 1000 years: A high-resolution record from the West Antarctic Ice Sheeet (WAIS) Divide ice core*, Global Biochemical Cycles, Vol. 26, Issue 2. https://doi.org/10.1029/2011GB004247

Anderson Thomas R., Hawkins Ed, Jones Philip D., 2016*: CO_2, the greenhouse effect and global warming: from the pioneering work of Arrhenius and Callendar to today's Earth System Models,* Endeavour, Volume 40, Issue 3, 2016, Pages 178-187, ISSN 0160-9327, https://doi.org/10.1016/j.endeavour.2016.07.002.

Beck Ernst-Georg, 2007: *180 Years of Atmospheric Co2 Gas Analysis by Chemical Methods.* Research Article. Energy & Environment, First Published March 1, 2007. https://doi.org/10.1260/095830507780682147.

Beck Ernst-Georg, 2008a: *50 Years of Continuous Measurement of Co2 On Mauna Loa,* Energy & Environment Vol 19 No 7. https://doi.org/10.1260/095830508786238288 Energy & Environment 19(7):1017-1028.

Beck Ernst-Georg, 2008b*: Evidence of variability of atmospheric CO2 concentration during the 20th century*. (discussion paper, May 2008). https://web.archive.org/web/20161201060229/http://www.biomind.de/realCO2/literature/evidence-var-corrRSCb.pdf

Beck Ernst-Georg, February 2010: *Reconstruction of Atmospheric CO_2 Background Levels since 1826 from direct measurements near ground.* Institute Biology III, University of Freiburg (personal communication).

Beck, Ernst-Georg, 2022*: Reconstruction of Atmospheric CO2 Background Levels since 1826 from Direct Measurements near Ground.* Science of Climate Change, 2, 148-211. https://doi.org/10.53234/scc202112/16

Daubechies, I. 1992: *Ten Lectures of Wavelet.* SIAM J. Math. Anal. 24, 499–519.

Gruber Nicolas, Gloor Manuel, Mikaloff Fletcher Sara E., Doney Scott C., Dutkiewicz Stephanie, Follows Michael J., Gerber Markus, Jacobson Andrew R., Joos Fortunat, Lindsay Keith, Menemenlis Dimitris, Mouchet Anne, Müller Simon A., Sarmiento Jorge L., and Takahashi Taro, 2009*: Oceanic Sources, Sinks, and Transport of Atmospheric CO_2.* Global Biogeochemical Cycles, 23, GB1005. https://doi.org/10.1029/2008GB003349

Humlum Ole, Stordahl Kjell, and Solheim Jan-Erik., 2013: *The Phase Relation Between Atmospheric Carbon Dioxide and Global Temperature*. Global and Planetary Change, Vo100, 51-69. https://doi.org/10.1016/j.gloplacha.2012.08.008.

Keeling C.D., Bacastow R.B., Bainbridge A.E., Ekdahl C.A., Guenther P.R., and Waterman L.S., 1976*: Atmospheric carbon dioxide variations at Mauna Loa Observatory, Hawaii,* Tellus, 28, 538-551. https://doi.org/10.1111/j.2153-3490.1976.tb00701.x

Keeling Ralph F, 2007: *Comment on "180 Years of Atmospheric Co2 Gas Analysis by Chemical Methods" by Ernst-Georg Beck.* Energy and Environment, 18(2), 259–282. https://www.jstor.org/stable/44397310.

Krajick Kevin, 2019: *Taro Takahashi, Who Uncovered Key Links Between Oceans and Climate. Traced Flows of Carbon Dioxide Across the Planet*. Columbia Climate School, Press Release, December 4. https://news.climate.columbia.edu/2019/12/04/taro-takahashi-who-uncovered-link-of-oceans-to-climate/.

Kunzig Robert and Broecker Wallace, 2008: *Fixing Climate*. Profile books ltd. London ISBN 987 1 84668 860 7.

Massen, Francis and Beck, Ernst-Georg, 2011: *Accurate Estimation of CO2 Background Level from Near Ground Measurements at Non-Mixed Environments.* In book: *The Economic, Social and Political Elements of Climate Change.* Edition: Climate Change Management. Chapter: 31. Publisher: Springer. Editor: Walter Leal Filho. https://doi.org/10.1007/978-3-642-14776-0. https://www.researchgate.net/publication/234004309_Accurate_Estimation_of_CO2_Background_Level_from_Near_Ground_Measurements_at_Non-Mixed_Environments

MATLAB 2020: MATLAB. *Wavelet Toolbox. Users Guide.* Portola Valley, CA, USA: The Math Works Inc.

Meiyer Harro A.J., 2007: *Comment on "180 Years of Atmospheric Co_2 Gas Analysis by Chemical Methods" by Ernst-Georg Beck:* Energy & Environment, 18(2), 2007. https://doi.org/10.1260/0958-305X.18.5.635.

Tansinez Pieter P., Fung Y. and Takahahi Taro, 1990: *Observational Constrains on the Global Atmospheric CO_2 Budget*. Science, Vol 247, No. 4949, 1431-1438. https://doi.org/10.1126/science.247.4949.1431.

Thoning K.W., Tans P.P. and Komhyr, W.D. *1989: Atmospheric Carbon Dioxide at Mauna Loa Observatory 2. Analysis of The NOAA GMCC Data, 1974-1985, J. Geophys. Research,* vol. 94, 8549-8565. https://doi.org/10.1029/JD094iD06p08549

Yndestad, H., Turrell, W. R., and Ozhigin, V., 2008: *Lunar Nodal Tide Effects on Variability of Sea Level, Temperature, and Salinity in the Faroe-Shetland Channel and the Barents Sea.* Deep Sea Res. Oceanographic Res. Pap. 55 (10), 1201–1217. https://doi.org/10.1016/j.dsr.2008.06.003.

Yndestad Harald, 2022: *Jovian Planets and Lunar Nodal Cycles in the Earth's Climate. Variability,* Frontiers in Astronomy and Space Sciences, 10 May. https://www.frontiersin.org/article/10.3389/fspas.2022.839794.

Conflict of Interest
No conflicts of interest are declared.

Author Contributions
This document is the author´s contribution.

Founding
This work has no founding.

Acknowledgments
The author thanks the editor Prof. Jan-Erik Solheim, guest editor Cand. Real. Stein Bergsmark. Valuable review comments from Prof. Ole Humlum, Cand. Real. Stein Bergsmark and Prof. Jan-Erik Solheim. Prof. Ole Henrik Ellestad and Prof. Jan-Erik Solheim for the many useful discussions of Beck´s work since 2009.

The Holocene Climate Change Story: Witnessed from Sola, Norway. Part 2

Correspondence to
mthovland@gmail.com

Vol. 2.3 (2022)

pp. 275 -287

Transition from interglacial (Eem) to glaciation (Weichsel), to the current interglacial (warm) period, Holocene, including changing sea-levels: transgressions and regressions.

Martin Torvald Hovland

Independent Scientist, Sola, Norway

Abstract

Part 2 reviews some of the pertinent knowledge about ancient climate variations, from ~ 70 Ma BP until the LGM (Last Glacial Maximum), 20 ky ago. There have been four distinct states over the last 50 Ma: *Hothouse*, *Warmhouse*, *Coolhouse*, and the current *Icehouse* climate state. Humanoids (mainly Neanderthals) lived in Europe from around 120 ky BP in caves. Anatomically modern humans (AMHs) came around 50 ky BP, during the midst of the Weichselian glaciation. The Neanderthals became extinct from around 40 ky BP and can have succumbed due to the last magnetic polarity shift, occurring between 42 and 40 ky BP. The icehouose climate state, with glaciations, started ~2.5 Ma ago. The sea-level has been at least 120 m lower than at Present. Last time around 25-20 kY BP during the LGM. During the deglaciation period (20 – 15 ky BP) the mean sea-level rise was about 20 mm per annum.

Keywords

Neanderthals, Anatomically modern humans, (AMHs), Weichselian glaciation, Hothouse, Warmhouse, Coolhouse, Icehouse, climate states, Last Glacial Maximum, (LGM).

Submitted 19-10-2021, Accepted 16-01-2022. https://doi.org/10.53234/scc202212/11

1. Introduction

The county of Sola (58° 55’ N, 5° 40’ E; see Part 1, Fig. 1) located in coastal Norway has a long and rich history of archaeological finds that date back to when Norway was first populated, immediately after the Weichselian glaciation. This glaciation culminated during the Last Glacial Maximum (LGM), about 20,000 years BP. The warming started then, and continued until about 12,800 years BP, at which time a new glaciation pulse arrived, during the Younger Dryas (YD). This 1,100 year long, brutally cold period, caused the fast-retreating glaciers to suddenly stop, and re-advance, leaving tell-tale morainic ridges throughout Scandinavia and Siberia (Mangerud, 2021). The nearest YD-morainic ridge to Sola, occurs in the Lysefjord, about 30 km inland.

2. The last 70 million years – Earth's climate and tectonic development

However, before we go back to Sola, let us take a brief look over our shoulder, and check out the chronology of Earth and climate history that led us into the current state of repeated glaciations. Modern geological and paleoclimatic science has managed to piece together an interesting narrative of the tectonic, climatic, and life history over the last 70,000,000 years (70 million years, Ma).

One of the world's most successful multinational scientific co-operations is, perhaps: the 'International Ocean Discovery Program' (IODP, previously known as the 'Deep-Sea Drilling Project', DSDP, and later, the 'Ocean Drilling Program', ODP). By using several suitable vessels, including the renowned workhorse 'Sedco 471 *Resolution'*, and the newer Japanese vessel '*Chikyu'*, the program, consisting of some 22 nations, has acquired hundreds of deep-water sediment cores from most oceans of the world, up to water depths of 6 km (for more information, see: www.iodp.org).

In 2001, this endeavor resulted in one of the most read paleoclimatic articles ever published, - by Jim Zachos and his team. The five authors of this review work is titled: «**Trends, rhythms, and aberrations in global climate 65 Ma to Present**». Here, they state that: «*The climatic evolution includes gradual trends of warming and cooling driven by tectonic processes on time scales of 10^5 to 10^7 years, rhythmic or periodic cycles driven by orbital processes with 10^4 to 10^6 years cyclicity, and rare rapid aberrant shifts and extreme climate transients with durations of 10^3 to 10^5 years*». Thus, the most anomalous such aberrant shift was found to be the mysterious temperature jump of the Late Paleocene, ~55 Ma BP. This temperature spike lasted about 200 ky (200,000 years) and has been named the Late Paleocene Thermal Maximum, LPTM (Fig. 1).

The LPTM-event is characterized by a 5° to 6°C rise in deep-sea temperature in less than 10 ky. In addition, sea surface temperatures (SSTs) as constrained by planktonic isotope records also increased, by as much as 8°C at high latitudes and lesser amounts toward the equator. An associated notable change in climate was globally higher humidity and precipitation, as evidenced by changes in the character and patterns of continental weathering. The event is also characterized by a ~3.0‰ negative carbon isotope excursion of the marine, atmospheric, and terrestrial carbon reservoirs, widespread dissolution of seafloor carbonate; mass extinction of benthic foraminifera; widespread proliferation of exotic planktic foraminifera taxa; and the dispersal and subsequent radiation of Northern Hemisphere land plants and mammals (Zachos et al., 2001; Bell & Seroussi, 2020).

The graph in Fig. 1 shows the Global deep-sea oxygen and carbon isotope records (green curve) based on deep-sea (>1000 m depth) sediment data compiled from more than 40 DSDP and ODP sites. Most of the data are derived from analyses of two common benthic foraminifers: *Cibicidoides* and *Nuttallides*.

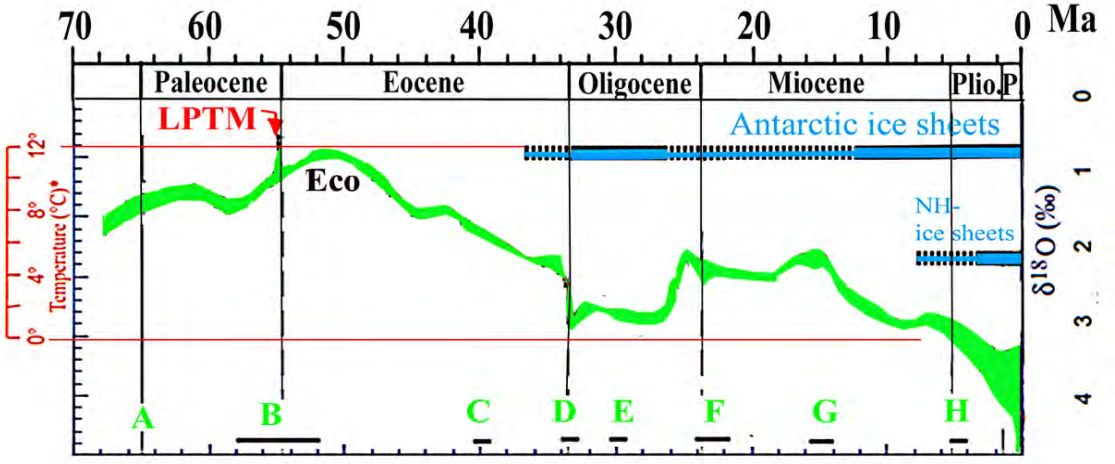

Figure 1. Global deep-sea oxygen isotope record (green curve), based on data compiled from more than 40 DSDP and ODP sites. The sedimentary sections from which these data were generated are classified as pelagic (e.g., from water depths >1000 m) with lithologies that are predominantly fine-grained, carbonate-rich (~50%) oozes or chalks. Most of the data are derived from analyses of two common and long-lived benthic taxa, *Cibicidoides* and *Nuttallides*. The $\delta^{18}O$ proxy temperature scale (shown in red on the left) was computed for an ice-free ocean, and thus only applies to the time preceding the onset of large-scale glaciation in Antarctica (~35 Ma). From the early Oligocene period to Present. In the figure, LPTM denotes the Late Paleocene Thermal Maximum, which was followed by the Eocene Climate Optimum period (Eco). The two blue horizontal bars provide a rough qualitative representation of ice volume in each hemisphere relative to the LGM, with the dashed bar representing periods of minimal ice coverage (<50%), and the full bar representing close to maximum ice coverage (>50% of present). Some key tectonic and biotic events are indicated in green letters and black bars at the bottom. These are explained in the text. (Modified from Zachos et al., 2001).

The figure also shows the temperature proxy scale of this curve. Because the direct coupling between the δO^{18} isotopic value and temperature is only valid for an open ice-free ocean, the proxy-temperature values are only valid from 70 Ma BP until the Antarctic ice sheets formed ~35 Ma ago, and the Arctic Sea ice, ~8 Ma ago (illustrated with blue horizontal bars in Fig. 1).

2.1 Some major events that occurred over the last 70 Ma

Figure 1 also indicates the periods of some major climatic, tectonic, and biological events occurring over the last 70 Ma. They are illustrated with green letters and black bars (Fig. 1). There is, of course, a myriad of major events that occurred on Earth over this long time-period, but only a very few select ones are shown here (from Zachos et al., 2001).

Thus, *Event A* (Fig. 1) refers to the meteor impact that occurred ~65 Ma ago at the so-called K-T boundary (the boundary between the two geological time-periods Cretaceous, K, and Tertiary, T). It had such a devastating impact that it is reckoned to have caused a mass extinction which also included almost all dinosaur animals.

Event B (Fig. 1) is also at a geological time-boundary, the Paleocene-Eocene transition, e.g., at the LPTM, at ~55 Ma BP. This was the time of active rifting and volcanism in the northern Atlantic Ocean. India collides with Asia. Mammals disperse around the world. The LPTM includes benthic extinction.

Event C occurs during the Eocene, ~40 Ma ago. Plate reorganization and a distinct, general reduction of seafloor spreading rates.

Event D, close to the Eocene – Oligocene transition, ~33 Ma. The glaciation of Antarctica starts. The Tasmanian – Antarctic passage opens. Archaic mammals and broad-leaf forests decline. Baleen whales appear.

Event E, during the Oligocene, ~30 Ma. The Drake passage (between South America and Antarctica) opens, giving room for the circum-Antarctic current. Large carnivores and other mammals diversify.

Event F, during the Miocene, 23 - 20 Ma. The Red Sea starts rifting. General coral extinction. Tibetan Plateau uplift accelerates. Seals and sea lions appear.

Event G, during the Mioecene, ~15 Ma. The Mid-Miocene climate optimum. Columbia river volcanism. East Antarctic ice sheet grows.

Event H, during the Miocene – Pliocene transition, 8 – 6 Ma. The West Antarctic Ice Sheet grows. Panama Seaway closes. Arctic sea ice grows. Hominids appear.

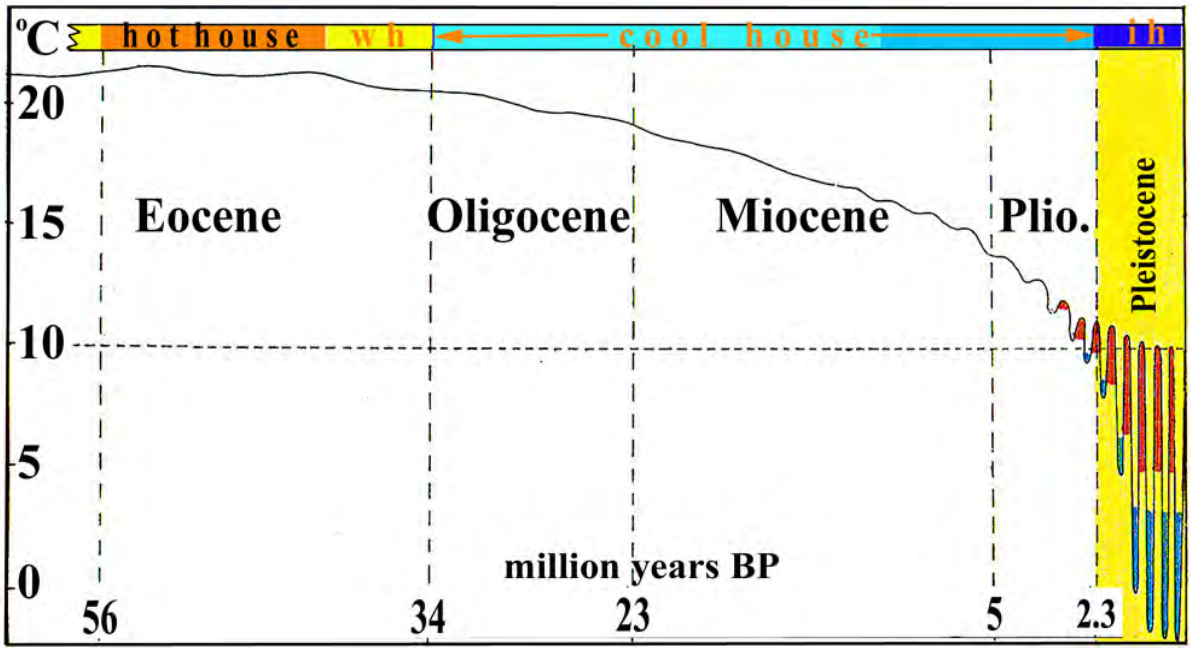

Figure 2. A schematic temperature graph showing the reconstructed mean surface temperature curve for Central Europe, as published by Paul Woldstedt (1954), slightly modified by Andersen and Borns (1994), who added colours on the right side (to enhance the cyclic ice-ages with glacial periods, blue, and interglacials, red, on a yellow background). The graph has also been modified by the current author, up-dating the ages for each of the time-periods, and adding the horizontal, coloured bar showing the extent of the four climate states: – Hothouse, Warmhouse (wh), Coolhouse, and Icehouse (ih) -periods, according to Westerhold et al. (2020). (Modified from Woldstedt, 1954; Andersen and Borns, 1994, and Westerhold et al., 2020). See text for more information.

It should be evident, that many of the events mentioned here, are not only isolated events, but may also be important causative events for the developing climate on Earth. For example, it is known that passages between oceans have had great impacts on the exchange of water between major ocean basins. For example, between the Atlantic and the Pacific oceans. Thus, the opening

of the Tasman – Antarctic passage led to glacial conditions on the East Antarctic continent ~35 Ma BP.

2.2 Reconstructed mean temperatures for Central Europe (56 Ma – Present)

However, the most notable and dramatic trend shown by the green curve in Fig. 1, is the steady cooling trend from around 50 Ma, until Present. This very important trend is more clearly illustrated in an earlier temperature graph, published by Woldstedt (1954). Although this older graph (Fig. 2) is only valid for Central Europe, it clearly shows how the climate gradually deteriorated and became cooler and cooler. It also demonstrates how the periodic glaciation cycles started during the Pliocene, about 2.5 million years ago and reflects the current climate situation on Earth.

In a recent article by Westerhold et al (2020), where the authors published "…*a new and highly resolved, astronomically dated continuous composite benthic foraminifer isotope record*…" for the last 70 Ma, with the aim of finding out more about climate predictability, they studied characteristic 'climate states', where the World undergoes a gradual transition, through: *"…four climate states – Hothouse, Warmhouse, Coolhouse, to Icehouse…*». Through their analyses, they managed to document that these four states are based on their "…*distinctive response to astronomical forcing depending on greenhouse gas concentrations and polar ice sheet volume*." (Westerhold et al., 2020, p. 1383).

Whereas these two temperature proxy curves in Figures 1 and 2, show how the climate has changed, in: "*trends, rhythms, and aberrations*", or rather, in particular temperature states: "*Hothouse, Warmhouse, Coolhouse, and Icehouse"* (e.g., Zachos et al., 2001, and Westerhold et al., 2020), there can be no doubt that the climate has consistently deteriorated (cooled) over the last 50 million years.

However, we will now move back to the Late Pleistocene and take a closer look at the period leading up to the LGM and the Holocene, and especially, the humanoid migration/population in Europe and the Americas. One relevant question needs to be answered: Was Norway (and the county of Sola) ever populated by humans prior to the Holocene period? We will demonstrate that the answer to this question must be, No!

3. From the Eem to the Holocene

As clearly stated by Westerhold et al. (2020), the current state of the world climate is an 'Icehouse'-state, in comparison to earlier, and warmer periods. The schematic temperature curve of Woldstedt (1954), Fig. 2 clearly illustrates the dramatic climatic cyclicity, which started ~ 2.5 Ma ago, when the climate started flipping in and out of mid-hemispherical glaciations of the northern European and North American continents, divided by shorter warm periods, called interglacials.

The two most recent glacial periods are the Saale, which lasted from ~235 ky to ~130 ky BP, and the Weichselian, from ~115 ky to ~20 ky BP (e.g., the LGM). The previous interglacial period, the Eem only lasted from ~130 ky to ~115 ky BP, and was a couple of degrees warmer than the current interglacial, the Holocene.

In Figure 3A the reconstruction of Earth's mean surface temperature variations is shown for the last cycle, e.g., from Eem to the Holocene. The Eem interglacial lasted for about 15 ky and must

have been optimal for humans to live and thrive at Sola, on the SW coast of Norway, even though the sea level was 5 – 10 m higher than at present (Fig. 3B). Because most of Norway had been covered by the Weichselian ice, snow, and water, any potential artifacts from this period would have been removed and washed away. Only at very few locations, including at Fjøsanger, near Bergen have sediments from the Eemian period been found in Norway. However, no remains of animals or humans have been found there (Vorren and Mangerud, 2006).

But there is one over-riding reason for there not being such remains or evidence: Modern humans had not entered Europe at that time. There may have been Neanderthals, but no *Homo sapiens*. As we shall see, they arrived Europe during the Weichselian glaciation.

It needs to be mentioned that the American glaciations and interglacial periods have different names than those used for the European periods. The American equivalent to the Eem interglacial is the Sangamon interglacial, and the American equivalent to the Weichselian is the Wisconsin glaciation.

*3.1 How (why) do interglacial periods end**?***

One of the mysteries about what may trigger the abrupt cooling at the termination of an interglacial period, like Eem, has recently been addressed by Yin et al. (2021). By analyzing the changes at the end of interglacials of the past 800 ky, they found that there exists a threshold in the level of astronomically induced insolation below which abrupt changes occur. Their causative effects are summed up as follows: "*When decreasing insolation reaches a critical value, it triggers a strong, abrupt weakening of the Atlantic meridional overturning circulation (AMOC) and a cooler mean climate state accompanied by high-amplitude variations lasting for several thousand years. The mechanism involves sea ice feedbacks in the Nordic and Labrador Seas. The ubiquity of this threshold suggests its fundamental role in terminating the warm climate conditions at the end of interglacials*." (Yin et al., 2021, p. 1035).

3.2 Human population in Europe and North America in Weichsel/Wisconsin

Humanoids and Anatomically Modern Humans (AMHs), existed on earth long before they found their way to Europe and North America, as shown in Table 1.

From Table 1, we see that *Homo sapiens neanderthalensis*, also called Neanderthals are known to have existed for more than 125 ky BP, which is just beyond the Eemian interglacial: "*The Neanderthals lived in large areas of central Europe and in the Mediterranean region up to the Middle Weichselian about 40 – 30 ky BP; at that time this species appears to have disappeared rather suddenly, and the modern species, Cro-Magnon type humans (*AMHs*), took over*." (Andersen and Borns, 1994).

3.3 Neanderthals in Europe, during Eem

So, let us see how our ancient ancestors came to Europe and what they experienced before migrating to Norway. In northern Spain, there is a large cave called the 'Estatuas' cave, which was a hive of humanoid activity 105 ky ago, which is ~10 ky after the Eemian interglacial warm period.

Table 1. Human development through pre-history (based on Andersen and Borns, 1994).

EARLY HUMANS	**Pre-historic cultures**	**Tool industries**	**Tools**
Homo sapiens sapiens (Cro-Magnon) 40 – 10 ky BP	Mesolithicum Upper – Younger Paleo-lithicum,	Magdalenien Solutrien Aurignacien	Arrowheads, knives, etc.
Homo sapiens neanderthalensis 125 – 40 ky BP	Middle Paleo-lithicum	Mousterian	
Homo erectus 1,5 Ma BP – 500 ky BP	Older Paleolithi-cum	Levalloisien Acheulien	Rough stone tools
Homo habilis 2.5 – 1 Ma BP	Older Paleolithi-cum	Olduvaien	Rough stone tools

The artifacts found at the bottom of this cave show that the Neanderthals used stone tools to butcher red deer, also that they made fire (Gibbons, 2021a). But the real find in the cave was remnants of the Neanderthal's nuclear DNA, from bones and teeth. By analyzing the DNA-distribution in the cave the researchers found that one group of Neanderthals replaced another: "*Neanderthals thrived and diversified during the warm, moist interglacial period that started 130,000 years ago. But about 110,000 years ago, temperatures in Europe dipped suddenly as a new glacial period set in. Soon after, all but one lineage of Neanderthals disappeared. Members*

of the surviving lineage repopulated Europe during later, relatively warm spells, with some taking shelter in Estatuas cave." (Gibbons, 2021a, p. 223).

3.4 Modern humans and Neanderthals mingle in Central Europe during Weichsel

In Bulgaria, large caves have also turned out a bounty of archeological humanoid finds and information about our ancient ancestors, some 1300 generations before they arrived in Norway. "*The four-story labyrinth of galleries in Bulgaria's Bacho Kiro cave has long been a magnet for all sorts of humans. Neanderthals came first, more than 50,000 years ago, and left their characteristic Mousterian stone tools among the stalagmites. Next came modern humans in at least two waves; the first littered the cave floor with beads and stone blades stained with ochre, about 45,000 years ago. Another group settled about 36,000 years ago with even more sophisticated artifacts*." (Gibbons, 2021b, p. 115). So, it is impossible for modern humans to have visited Norway during the Eem interglacial, as they never arrived to Europe from the east (Asia) and south (Africa) before about 45 ky BP.

The strange fact that Neanderthals did not make it through the Weichsel, shows that they must have, somehow, succumbed before the LGM. It has been speculated that they were ousted by AMHs. However, we shall see that there is a new and perhaps more sound explanation for their extinction. There was a magnetic reversal period, 42 – 40 ky BP, with some rather special environmental changes occurring, which may have been too much for them (see later).

3.5 Warmer periods during Weichsel: Interestadials

It is important to note, that the glacial periods, like Weichsel also include long periods with milder climate, the so-called 'interstadial' periods. Some of these milder periods can be seen on the two graphs in Fig. 3, where the upper graph (A) shows the average global temperature during Eem and Weichsel. Notice that there are at least six peaks with higher temperatures before the LGM.

The same can be seen also in the middle graph (Fig. 3B), which shows a record of the global sea-level variations. Here it is worth noting that the sea-level during Eem was higher than during the Holocene. Furthermore, the remarkable similarity between the two graphs (Figs. 3A and B) is also worth noting. It shows that the maximum drawdown of the world's-ocean during the LGM was about 120 m below the current sea-level. There are about 6 milder periods during the Weichselian glaciation with only less that 40 m lower sea-level than at Present.

Despite a general cold climate, the character of glacial periods is, based on stable isotope analyses, rather climatically complex. Paleoclimatologists using the δO^{18} stable isotope signal have identified different 'isotope stages', which are defined as warmer periods and colder periods during the glaciations, with the warm periods called 'interstadials', - and, the cool periods called 'stadials'.

3.6 Isotope stages during the Weichselian glaciation.

In Fig. 3C, the first five isotope stages are illustrated with their characteristic isotope values, which correspond to deep ocean mean temperatures. The oldest isotope stage shown in Fig. 3C, is isotope stage 5e, which is the warm Eemian interglacial period, from 130 to 115 ky BP. The following isotopic stages are 5d – 5a, consisting of two cool stadials (5d and 5b) and three warm

interstadials (5c and 5a). During the two stadials (5d and b), there is evidence of good-sized glaciers being developed in Scandinavia (Andersen and Borns, 1994).

However, a much colder climate develops during the middle Weichselian, isotope stages 4 and 3, e.g., from 75 – 25 ky BP. The climate cooling was rapid and marked the start of a very long cold period. "*During the major cold peak of isotope stage 4, the tundra/prairie covered central and northern Europe, and the glaciers expanded to cover much of Scandinavia. The Oceanic Polar Front moved south to the latitude of southern France and extended westwards towards North America. To the north of this latitude most of the North Atlantic Ocean was covered with pack ice during winters*." (Andersen and Borns, 1994, p. 53).

The climate also remained cold during most of isotope stage 3 (60 – 25 ky BP). Glaciers then covered considerable parts of Fennoscandia, as evidenced by glacial deposits in northern Sweden and Finland and on the west coast of Norway. But the climate and glaciers fluctuated with two to five slightly warmer interstadials recorded in various parts of northern Europe. During two interstadials, about 30 ky ago and somewhere between 40 and 70 ky BP, the west coast of Norway was ice free.

Whereas isotope stage 1 is the warm Holocene, interglacial period, isotope stage 2 is the LGM, where the glaciers in northern Europe grew to their largest extent. This very cold period, where the sea-level had retreated (or 'regressed') to ~120 m, lasted for nearly 10 ky. Because of the extreme cold, the lower atmosphere was also relatively dry. With large regions of the seafloor of the world exposed, there was a peak in dust in the lower atmosphere. This is because much of the newly exposed seafloor consisted of fine clay particles that dried out and easily became mobilized by strong winds.

The land bridges that occurred during the extreme ocean lowstand, included the Bering Strait, between Asia and America, the strait between New Zealand's northern and southern islands, and the strait between Australia and Papua New Guinea. Large areas of the North Sea were either covered by ice or became dry land. However, between Norway and this land, there were no bridges because of the deep water in the Norwegian Trough (see Part 1).

3.7 The population of North America during the Wisconsin glaciation (115 – 25 ky BP)

It was long thought that the first people in North America were the Clovis, that arrived around 13 ky BP. But when older sites showed up, 'pre-Clovis' people were dated to 16.5 ky BP. However, now there is evidence that people were in America even before the LGM, at around 26.5 to 20 ky BP.

This is, despite the fact, that the only viable migration routes from Asia to America were dependent on timing and glacial conditions. During the LGM, the ice sheets were too massive to pass for migrating humans. During some of the Wisconsin interstadials the glaciation of the North American continent was divided in two large glacier complexes or ice sheets: the northern (Laurentide) and the southern (Cordilleran) ice sheets. Between these there was a variably wide 'Ice-Free Corridor', where humans could have traveled south of the large ice sheets. Recently, Bennett et al. (2021) found definitive evidence confirming the presence of modern humans in North America during the LGM. This evidence comes in the form of fossilized human and animal footprints in semi-dried lake muds in New Mexico: "*We report the discovery of a series of human footprints from White Sands National Park (WHSA Locality 2) in south-central New Mexico that occur on multiple stratigraphic horizons interbedded with seed layers. Our results indicate that humans*

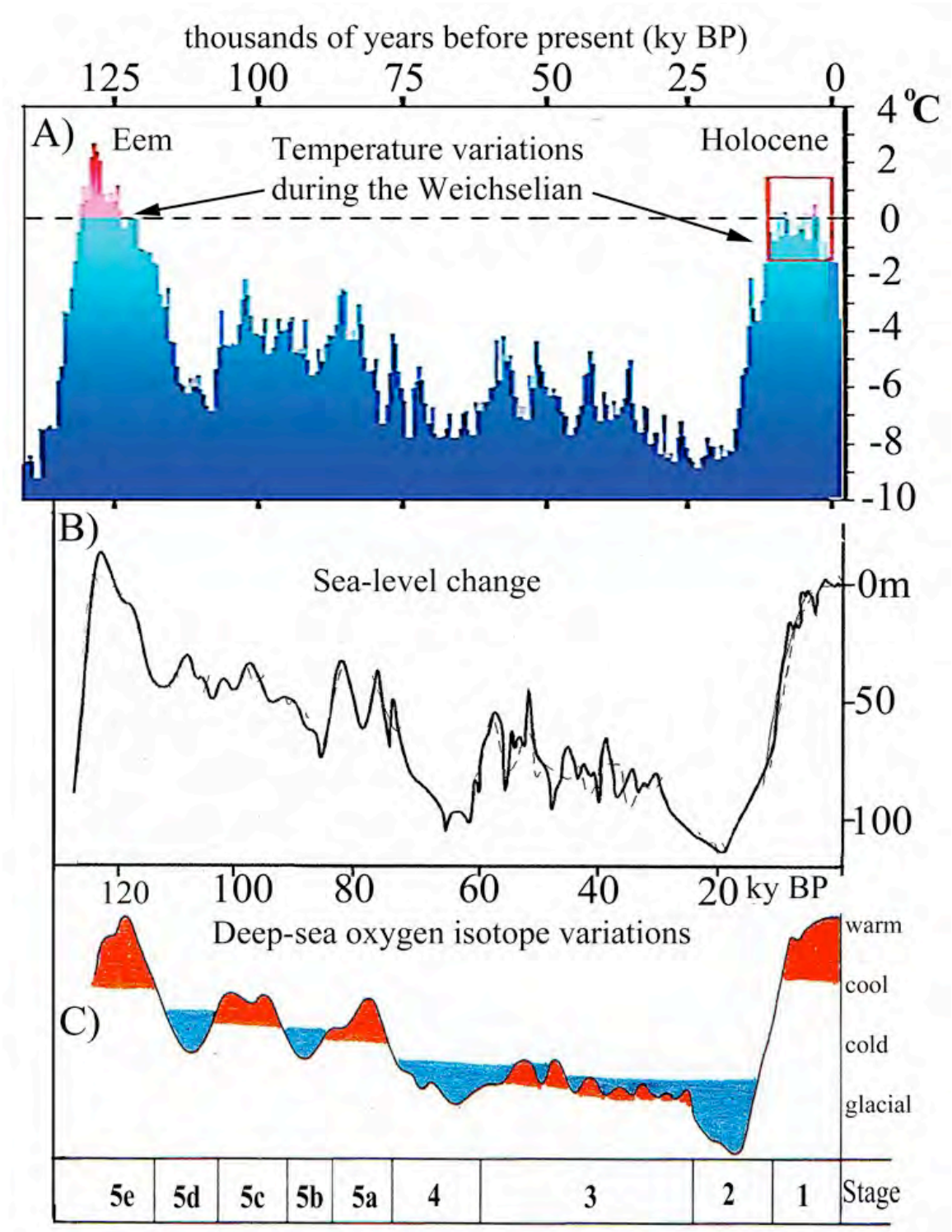

Figure 3. Three different graphs that show a co-variation between three different physical parameters. They all bear the same message: The past 120 thousand years have seen dramatic climate changes. A) shows the mean global surface temperature variations. This temperature graph is based on two Antarctic ice-cores: Vostok and EPICA Domes. (See www.climatedata.info/proxies/ice-cores/). The global sea-level change graph in (B) is based on isotope records of planktonic fauna from the Red Sea (modified from Siddall et al., 2003 and Momber et al., 2019). Finally, the deep-sea oxygen isotope variations, in (C) are modified from Andersen and Borns (1994) and Martinson et al., 1987).

were present on the landscape by at least ~23 ky, with evidence of occupation spanning approximately two millennia." (Bennett et al., 2021, p. 1528).

They also conclude that these humans must have arrived:"…*before the glacial advances of the LGM closed the Ice-Free Corridor and the Pacific Coastal Route that prevented human migration from Asia*." This example of new discoveries clearly shows that there are potentially numerous new discoveries to be made, with respect to early human migration and population dynamics both in northern Europe and North America.

3.8 A magnetic polarity shift around 42 ky BP, during late-Weichselian and Wisconsin.

How does a shift in magnetic polarity of the Earth affect humans? Because the Earth's magnetic field has steadily weakened over the last 170 years, and the magnetic North Pole is moving more rapidly than before, this is currently a relevant question to ask. It is known that the last major magnetic inversion occurred during the last part of the Weichselian, over a period of about 1 ky, from ~42 ky to 41 ky BP. However, there is some frustration because there are no signs of dramatic environmental changes occurring on Earth from studies of ice- and sediment cores.

However, some recent studies of ancient New Zealand kauri trees, enabled the researchers to develop a detailed record of atmospheric radiocarbon levels across the Laschamps Excursion (the name of the last major magnetic inversion, e.g., 'polar shift'). As the researchers widened their studies to other fields, they found surprising implications, and sum up their findings as follows: "*The implications of this study are considerable. The event is very close in timing to the globally widespread appearance and increase in figurative cave art, red ochre handprints, and changing use of caves ~42 to 40 ky BP, e.g., in Europe and Island Southeast Asia. This sudden behavioral shift in very different parts of the world is consistent with an increasing or changed use of caves during the event, potentially as shelter from the increase of ultraviolet B, potentially to harmful levels during GSM (Grand Solar Minimum) or SEPs (Solar Energetic Particles), which might also explain an increased use of red ochre sunscreen. Rather than the actual advent of figurative art, early cave art would therefore appear to represent the preservation of preexisting behaviors on a new medium. Other important archaeological boundaries during the wider Laschamps event include the extinction of the Neanderthals along with the disappearance of some of the first European AMH (Anatomically Modern Human) cultures*." (Cooper et al., 2021, p. 817).

The main environment disturbances are: markedly increased levels of solar and cosmic radiation, due to the weakened geomagnetic field. This would cause increased ionization and decreased stratospheric ozone levels, potentially generating regional climatic impacts, particularly in lower latitudes. Around the Pacific Basin, there is evidence of a major and often sustained change in behavior ~42 – 40 ky BP. These include local glacial maxima in Australasia and the Andes, long-term shifts in atmospheric circulation patterns, and continent-wide aridification and megafaunal extinction in Australia. In North America, the same period experienced a rapid expansion of the Laurentide Ice Sheet (LIS), from a local minimum close to 42 ky BP. (Cooper et al., 2003).

3.9 Fluctuations in sea-level, from Eem to Holocene

Over the past 20 ky, there has been approximately 120 m of eustatic sea-level rise due to glacial melting. From Figure 3 it is easy to see that abrupt cooling during the end of the Eemian interglacial period leads to abrupt lowering of the mean sea-level. The reason, of course, is that the seawater that evaporates, subsequently leading to precipitation over colder land, as snow and

hail. On land, the snow will accumulate, rather than melt to water and flow back into the ocean. Over time, this leads to a lowering of the sea-level. During warming, the sea-level will start rising again, because of snow melting and precipitation as rain, rather than snow and hail. The three graphs in Fig. 3A, B, and C demonstrate that there is full harmony between temperature change, sea-level change, and deep-sea oxygen isotope variation. This also means that the global sea-level is a proxy, or an equivalent, to global ice volume.

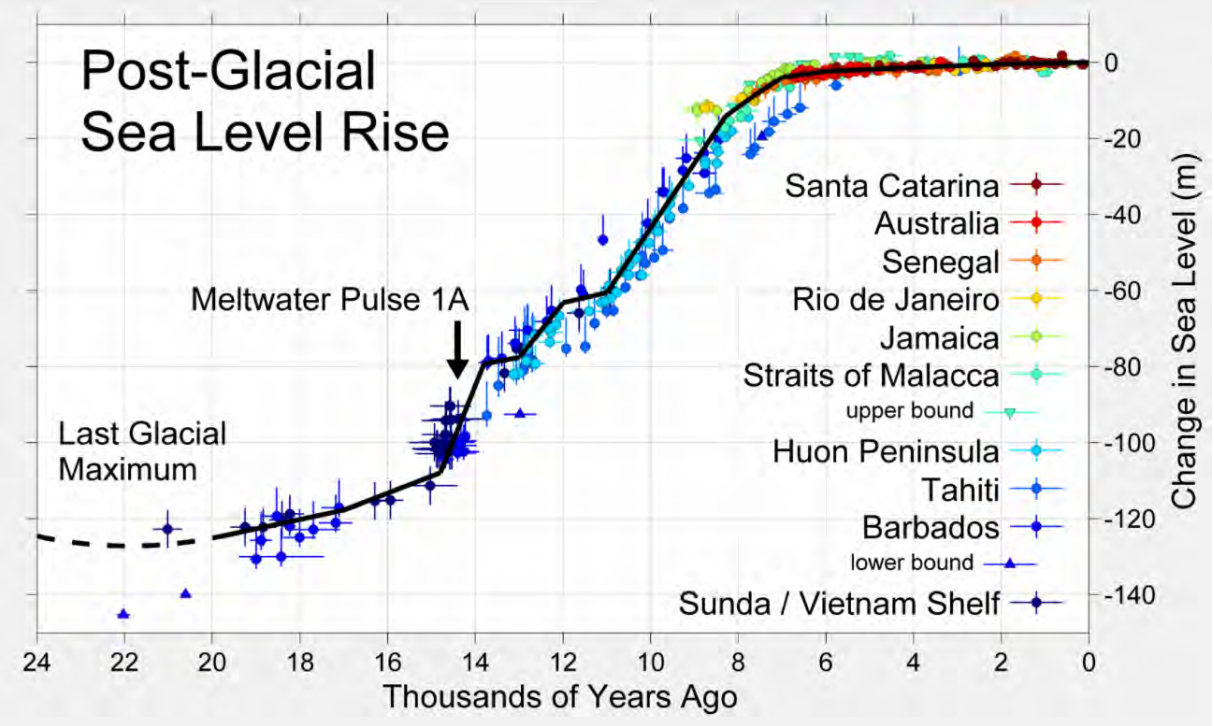

Figure 4. A classical sea-level curve for the LGM – Holocene period. It is based sea level highstands reconstructed from dating fossil coral reef terraces. It shows the deglaciation period from LGM, 20 ky BP and throughout the Holocene (based on Siddall et al., 2003).

The sea-level curve reconstruction shown in Fig. 3B is based on oxygen isotope records from Red Sea sediment cores: «*This study takes advantage of the fact that the Red Sea is extremely sensitive to sea-level change, as a consequence of the narrow (18 km) and shallow (137 m) character of its only connection with the open ocean (the Strait of Bab el Mandab). Reduction of the strait profile by sea-level lowering decreases the exchange transport of water masses through the strait*.» (Siddall et al., 2003, p. 853)

According to Siddall et al. (2003), there have been maximal sea-level rises of up to 35 m, at rates of up to 20 mm yr^{-1} during the Weichselian. This is also equivalent to the mean rate of change during the last deglaciation, following the LGM, as also shown in Fig. 4.

To be continued in the next issue. (Part 3: The very first Mesolithic settlers at Sola, - first ever settlement of *Homo sapiens* in Norway).

Acknowledgements

Advice and comments by Håkon Rueslåtten are greatly appreciated.

Editor: Geir Hasnes; Reviewer: anonymous.

References

Andersen, B.G. and Borns Jr., H.W. (1994) *The Ice Age World.* Scandinavian University Press (Universitetsforlaget, Oslo). ISBN 82-00-21810-4, 208 pp.

Bennett, M.R., Bustos, D., et al. (2021) *Evidence of humans in North America during the Last Glacial Maximum.* Science 373 (6562), 1528-1531.

Cooper, A., Turney, C.S.M., et al., (2021) *A global environmental crisis 42,000 years ago*. Science 371 (6531), 811-818.

Gibbons, A. (2021a) *When modern humans met Neanderthals; Ancient genomes from first modern humans in Europe tell stories of diverse origins, ancient trysts*. Science, 372 (6538) 115-116.

Gibbons, A. (2021b) *DNA from cave dirt traces Neanderthal upheaval*. Science, 372 (6539), 222-223.

Mangerud, J. (2021) *En uventet klimakatastrofe under siste istid*. (In Norwegian). https://forskersonen.no/geofag-geokjemi-istiden/en-uventet-klimakatastrofe-under-siste-istid/1882907

Martinson, D.G., Pisias, N.G., Hays, J.D., Imbrie, J., Moore, T.C., Shackleton, N.J. (1987) *Age dating and the orbital theory of ice ages: Development of a high-resolution 0 to 300 000-year chronostratigraphy*. Quaternary Research 27, 1-30.

Momber, G., Sakellariou, D., Rousakis, G., Bailey, G.N. (2019) *The multi-disciplinary search for underwater archaeology in the southern Red Sea.* In: Rasul, N.M.A., Stewart, I.C.F. eds. Geological Setting, Palaeoenvironment and Archaeology of the Red Sea. Springer Nature, pp. 605-628.

Siddall, M., Rohling, E.J., Almogi-Labin, A., Hemleben, Ch., Meischner, D., Schmelzer, I., Smeed, D.A. (2003*) Sea-level fluctuations during the last glacial cycle.* Nature 123, 853 – 857.

Vorren, T. O., Mangerud, J. (2006) Istider kommer og går. In: Ramberg, I.B., Bryhni, I. and Nøttvedt, A. eds. *Landet blir til*. Norsk Geologisk Forening, pp. 482-515. ISBN 978-92-92344-31-6. (In Norwegian).

Westerhold, T., Marwan, N., et al. (2020) *An astronomical dated record of Earth's climate and its predictability over the last 66 million years*. Science 369 (6509), 1383-1387.

Woldstedt, V.P. (1954) *Die Klimakurve des Tertiärs und Quartärs in Mitteleuropa. Eiszeitalter und Gegenwart,* Bd. 4/5, 5-9. (In German).

Yin, Q.Z., Wu, Z.P., Berger, A., Goosse, H., Hodell, D. (2021) *Insolation triggered abrupt weakening of Atlantic circulation at the end of interglacials.* Science 373 (6558), 1035-1040.

Present Uplift in Norway Due to Glacier Unloading Since the 'Little Ice Age'

Correspondence to
wf@tectonor.com

Vol. 2.3 (2022)

pp. 288-296

Willy Fjeldskaar[a] and Aleksey Amantov[b]

[a]*Tectonor AS, Stavanger, Norway*

[b]*VSEGEI, St. Petersburg, Russia*

Abstract

The observed present rate of uplift in Scandinavia increases from zero on the western coast of Norway to ~1 cm/yr in the Baltic Sea area. This domelike uplift is generally assumed to be the result of glacial isostasy due to melting of the huge glaciers of late-glacial time. The mountain glaciers of Norway have previously not been considered to affect the present rate of uplift. We have now calculated the effect of the decaying glaciers since the Little Ice Age and found that the effect is a significant factor in the ongoing rate of uplift in Norway.

While the last huge sheet over Scandinavia melted away around 9 000 years ago, a cooling trend (Neoglaciation) some thousand years later was responsible for the establishment and growth of the Norwegian mountain glaciers. After several periods of glacier growth and decay most Norwegian glaciers probably culminated in mid 1700s AD during the Little Ice Age. From the Little Ice Age the glaciers started to decay and finally ended at the present thicknesses of the glaciers.

We calculated both the isostatic and elastic response of the unloading of the mountain glaciers. When a force (positive or negative) is applied to the Earth's surface, there is an immediate elastic deformation proportional to the stress. This will be followed by a time-dependent isostatic response. The elastic displacement is gradually recovered as the Earth adjusts toward isostatic equilibrium. When isostatic equilibrium is achieved, there will be no elastic deformation. There are thus basically two causes of elastic effects: (l) loading/unloading of ice caps, (2) isostatic movements caused by the loading/unloading.

The isostasy is calculated with a low-viscosity asthenosphere of 1.8×10^{19} Pas and an effective elastic lithosphere thickness Te ~30 km. The elastic modelling assumes the shear rigidity $\mu = 0.7 \times 10^{11} N/m^2$. This unloading of the Norwegian glacier over the last 300 years lead to present rate of uplift in glaciated areas of more than 2.0 mm/yr in the areas of mountain glaciers.

Submitted 07-12-2021, Accepted 08-01-2022. https://doi.org/10.53234/scc202212/10

1. Introduction

The observed ongoing rate of uplift in Scandinavia increases from zero on the western coast of Norway to ~1 cm /yr in the Baltic Sea area. Figure 1 shows the observed current uplift in Fennoscandia according to the recent NKG2016LU (Vestøl et al., 2016). This domelike uplift is generally assumed to be the result of glacial isostasy due to melting of the huge late-glacial ice sheets. The last remains of the huge glaciers melted away around 9 000 cal yr BP. Mörner (1980) claimed that the post-glacial uplift is caused by two different mechanisms – one exponential and one linear factor. Mörner's idea is disputed; the consistent picture given by the observations of the deglaciation, palaeo-shoreline tilts and present rate of uplift does not require two different mechanisms. It has been shown previously (e.g. Fjeldskaar, 1997; Fjeldskaar and Amantov, 2017) that the best-fitting parameters for palaeo-shoreline tilts also are the best-fitting parameters for the present rate of uplift.

Even so, Mörner's idea about an additional factor in the current uplift may still be viable; the question is how significant this factor is. Clearly, most of the uplift signal can be explained by isostatic response to the deglaciation after the last ice age. However, the west coast of northern Norway is the most important exception here. Fjeldskaar et al. (2000), Amantov and Fjeldskaar (2013) and Fjeldskaar et al. (submitted) found that this is an area where the measured present rate of uplift is significantly greater than that predicted by glacial isostatic models.

This paper investigates the affects of the reduction of the mountain glaciers in Norway for the present rate of uplift. Most of the Norwegian glaciers were developed during a colder Late Holocene period and probably culminated in mid 1700s AD during the Little Ice Age.

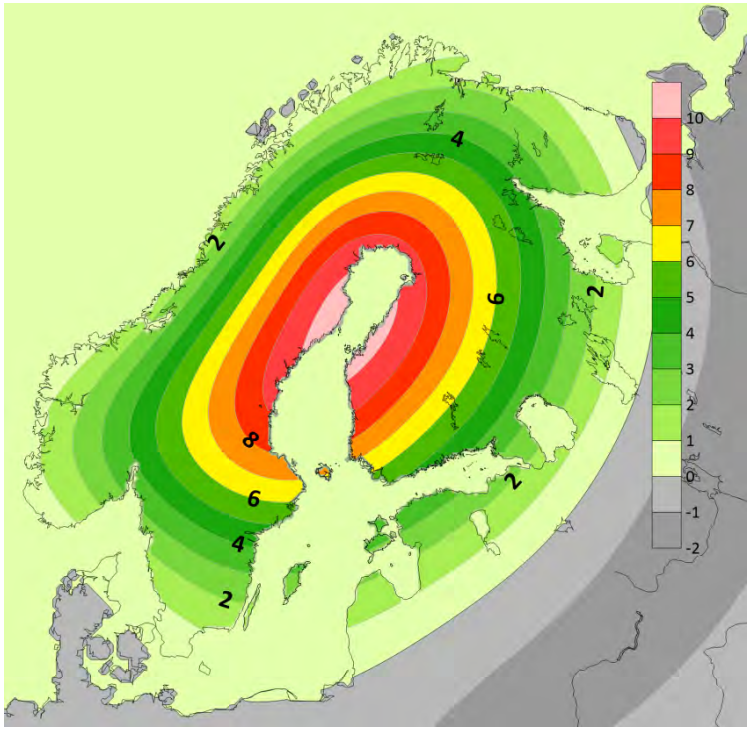

Figure 1. Observed present rate of uplift (in mm/yr) from Vestøl et al. (2016).

After the Little Ice age there has been a significant reduction of the glaciers, which will result in land uplift in both northern and southern Norway.

2. Mountain glaciers

Most Norwegian mountain glaciers melted away during the Holocene Climatic Optimum (HCO); as a consequence of warmer summer temperature (e.g. Nesje, 2009) between 8 000 and 6 000 cal yr BP (e.g. Nielsen et al., 2018). Following this warm period, glaciers started to reform during the Neoglaciation which started ~6 000 cal yr BP and ended with the Little Ice Age some 300 years ago (e.g. Nesje, 2009 and references therein).

After several periods of glacier growth and decay most of the Norwegian glaciers probably culminated in the Little Ice Age (Nesje, 2009). From the mid 1700s AD the glaciers started to decay and finally ended at the present glacier thicknesses. We have made a model of the glacier thickness growth and decay in which we assume that the glacial growth started at 6 000 cal yr BP and grew to a maximum 300 years ago (for maximum exceeding the current ice thicknesses, see Fig. 2). From 300 years ago the glaciers started to decay in thicknesses (as given in Fig. 2) before present status is achieved.

In the modelling the glacier growth from 6 000 to 300 cal yr BP is assumed to take place with uniform velocity, so is the decay from 300 to present. The spatial resolution in our modelling is 10 km; this high spatial resolution is a requirement (in addition to high temporal resolution) in order to do realistic modelling of the isostatic and elastic response due to the glacier changes of the Late Holocene.

Figure 2. Model of the unloading of mountain glaciers. Dark blue colour shows ice thicknesses exceeding 100 m compared to present day.

3. Isostatic response

The isostatic response to the load of the changing glaciers is in our study modelled by an incompressible viscous half-space in which the viscosity may vary with depth, i.e. the properties are constant within layers of variable thickness. The viscous fluid is overlain by an elastic lithosphere of uniform thickness. The mantle is considered fully adiabatic; no buoyancy forces affect the flow other than those related to the surface load redistribution. The method used here is described in Fjeldskaar (1994, 1997) and Fjeldskaar and Cathles (1991). The best-fitting model of the present rate of uplift based on the glacial history has a low-viscosity asthenosphere of 1.8 x 10^{19} Pa s and a weak lithosphere with flexural rigidity 2 x 10^{23} Nm (effective elastic thickness Te ~30 km) (Fjeldskaar et al., submitted). The mantle has a viscosity of 10^{21} Pa s. The Earth´s parameters are similar to the parameters found e.g. for Lake Mead area, USA. Based on the observed subsidence in the area around the lake Kaufman & Amelung (2000) found the best-fitting parameters to be an effective elastic lithosphere thickness of ~30 km over a mantle viscosity of 10^{18} Pa s.

The isostatic response of the assumed decay of the glaciers after the Little Ice Age was modelled with the same Earth rheology. The calculated ongoing isostatic uplift of the decreasing glaciers is close to 2 mm/yr for both northern and southern areas of Norway (Fig. 3). The theoretical present uplift due to the mountain glaciers decay is thus significant compared to the observed uplift in those areas (cf. Fig. 1). The reason for this significant effect is simply that

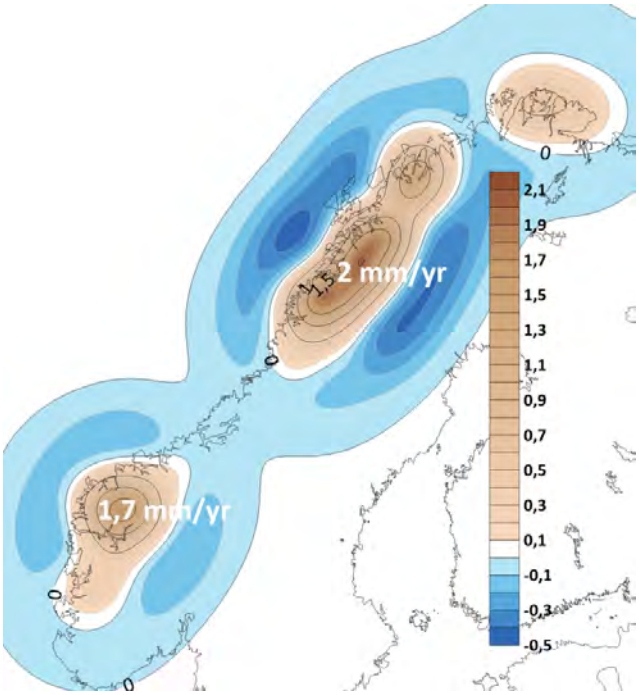

Figure 3. Calculated present rate of uplift due to isostatic response of the unloading of mountain glaciers (in mm/yr).

the decay of the mountain glaciers takes place much closer to present time. In addition the relaxation time for low wavelength deflections (like the this significant effect is simply that the decay of the mountain glaciers takes place much closer to present time. In addition the relaxation time for low wavelength deflections (like the mountain glaciers) is much lower than for the Fennoscandian type late-glacial huge ice sheets (for relaxation times vs. wavelengths, cf. Fjeldskaar and Amantov, 2017).

4. Elastic deflections

When a force is applied to the Earth's surface, there is an immediate elastic deformation proportional to the stress. Almost all solid rocks behave elastically when the applied forces are not too large, and return to their original shape when the force is removed. The elasticity of a crystalline solid arises from the action of interatomic forces, which tend to maintain each atom in its equilibrium lattice position. Rocks behave quite differently in response to applied forces, depending on the elastic properties of the rocks. Changes in rock type within the crust, vertically and horizontally, contribute to variations in the response. The elastic behaviour of a material can be characterized by specifying the Lame's parameters λ and μ.

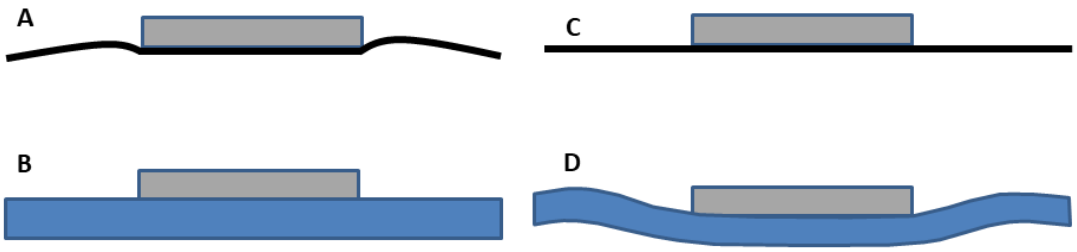

Figure 4. Illustration of the interrelation between isostatic and elastic deflections. (A) Immediate elastic deflection, (B) immediate isostatic deflection, (C) equilibrium elastic deflection after infinite time, and (D) equilibrium isostatic deflection after infinite time.

The elastic displacement is gradually recovered as the Earth adjusts toward isostatic equilibrium. When isostatic equilibrium is achieved, there will be no elastic deformation. There are thus basically two causes of elastic effects: (l) loading/unloading of ice caps, (2) isostatic movements caused by the loading/unloading. This is illustrated in Figure 4. At the loading of the ice sheet, there will be an immediate elastic response (A). The immediate isostatic response (B) will be close to zero, because of a finite viscosity of the mantle. After infinite time, the lithosphere reaches an equilibrium isostatic position (D), which means that the surface load is balanced by buoyant forces. Lower parts of the Earth will, thus, not 'see' any loads at the surface.

Elastic deflection is a function of the wavelength of the load, and also of the elastic properties of the crust. The response *u(k)* of an incompressible elastic medium to a surface load of wave number k is (Cathles, 1975):

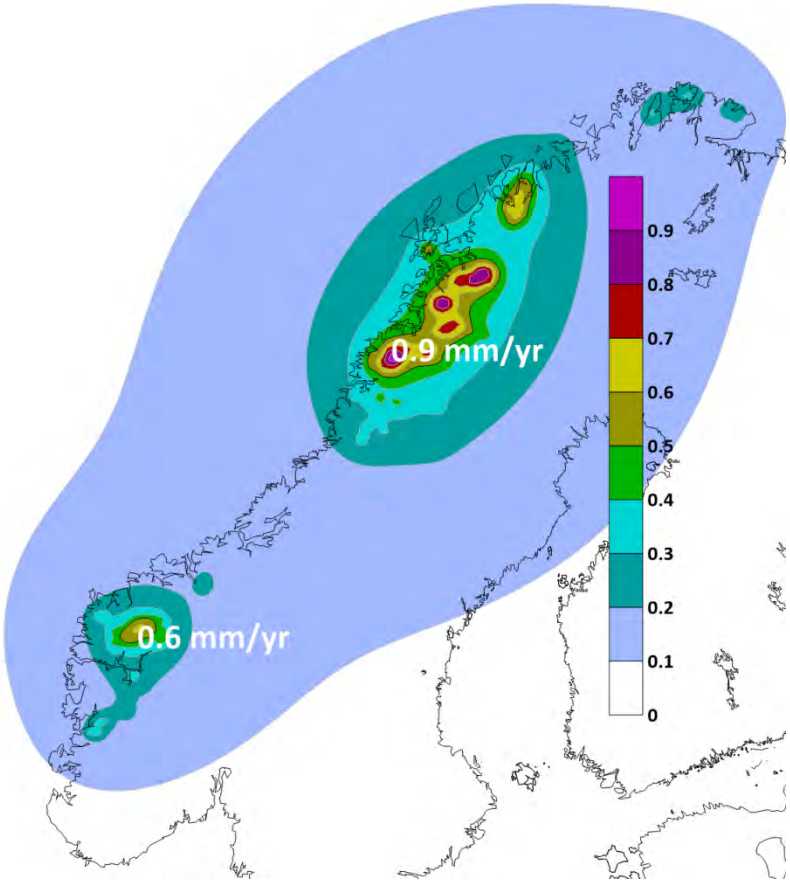

Figure 5. Present elastic response to the melting of the mountain glaciers (in mm/yr).

$$u(k) = \frac{\rho_0\, g\, h}{\mu\, k}$$

where μ is the shear rigidity, g is the gravity, h is the thickness of the load, and ρ_o is the density. In the modelling we have used shear rigidity $\mu = 0.7 \times 10^{11}$ N/m^2. The method for the calculations is described in Fjeldskaar (2000). The calculated ongoing elastic uplift due to the unloading of the mountain glaciers has a maximum in northern Norway of 0.9 mm/yr, and in southern Norway of 0.6 mm/yr (Fig.5).

5. Total response of unloading of mountain glaciers

The total present uplift due to the combined isostasy and elastic response (Figs 3 and 5) of the decaying mountain glaciers is very close to 2.5 mm/yr in northern as well as southern Norway (Fig. 6a).

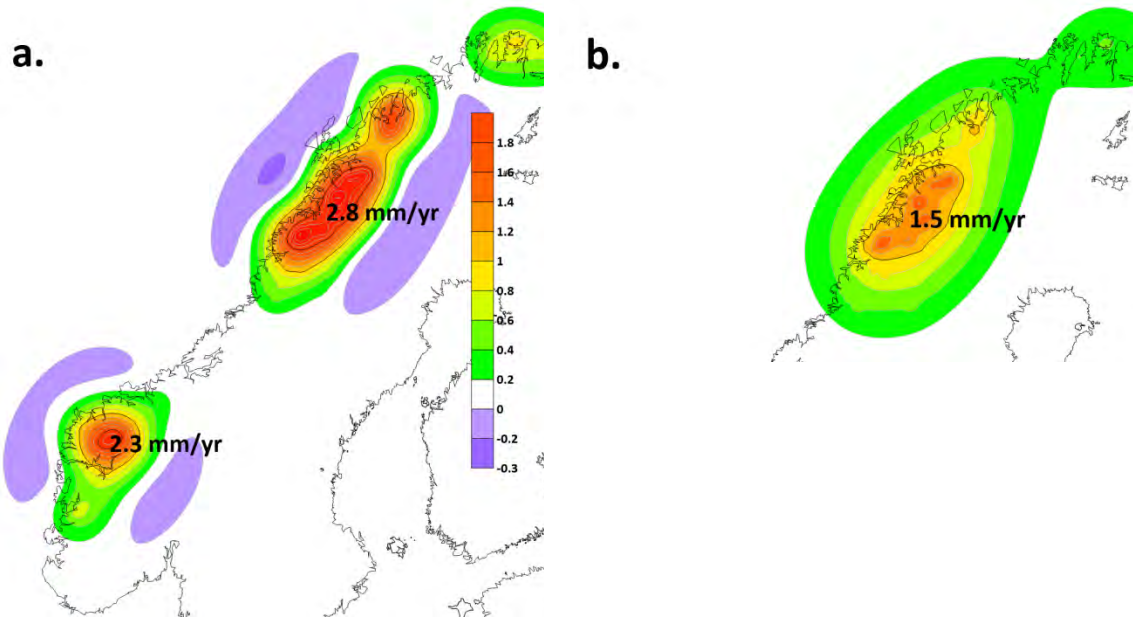

Figure 6. Calculated combined isostatic and elastic present uplift due to unloading of glaciers over the last 300 years. a) effective elastic lithosphere thickness Te = 30 km; b) for Te =80 km.

6. Discussion

We have added a second Earth rheology model with a thicker effective elastic lithosphere (Te = 80 km; fr = 5 x10^{24} Nm) because Fjeldskaar and Bondevik (2020) found evidence of a possible increase in Te (or alternatively a significant tectonic component) towards the northernmost part of Norway in their study of the Tapes transgression. Present total uplift for northern Norway with a model of thicker effective lithosphere thickness is 1.5 mm/yr (Fig. 6b).

There are significant uncertainties in these calculations, however, related primarily to the timing of the maximum glaciations, and to the magnitude of the maximum ice thicknesses. The glaciers during the Neoglaciation changed over time and there were several intermittent periods with extensive glaciers (Nesje, 2009). Our modelling is limited to one period of maximum glaciers, set to 300 years ago, and we assume uniform velocity growth from 6000 cal yr BP to 300 years ago. The resulting isostatic effect could, however, be different if we had taken into account that glaciers experienced several periods of significant advances and retreats during the period before the Little Ice Age maximum. In addition, the maximum extension does not necessarily coincide in time with maximum volume.

We have tested various options of the Neoglacial glaciations and deglaciations, all assuming the glacial growth and reduction to take place simultaneously on all glaciers. This is probably a reasonable assumption over a limited areas like northern and southern Norway. If we change the maximum ice thickness to take place much earlier, e.g. at 2500 cal yr BP, the ongoing isostatic uplift will be reduced, but will still be significant (close to 1.5 mm/yr in northern Norway) and with a maximum in the same location. However, the elastic effect will be reduced because the areas will be closer to isostatic equilibrium.

The magnitude of the ongoing uplift will increase with a greater maximum ice thickness. As expected, there is a clear tendency of increasing ongoing uplift if the maximum ice thicknesses are of more recent time. The ice thicknesses during a tentative maximum carry significant uncertainties. Even for small glaciers the late thickness reduction is likely to exceed 100 m (e.g. Bakke et al., 2010). If, however, our model (Fig. 2) is exaggerating the ice loads, the magnitude of the uplift will be reduced, but the shape of the calculated uplift will still be similar to the uplift shape of Figure 6. On the other hand, with a doubling of the ice thickness, there will also be a doubling of the isostatic and elastic response.

It is also worth mentioning that many researchers use a different approach to glacial isostasy than we do, a global GIA model based on the correspondence principle (cf. e.g. Peltier, 1974). That model implies a significantly different Earth rheology from what we have used above. Steffen and Wu (2011) have reviewed modelling results on Fennoscandian rheology for such models based on observations of both postglacial and ongoing uplift. Their suggested Earth rheology for Fennoscandia consists of an effective elastic lithosphere thickness (Te) between 75 and 160 km, and a viscosity of the lower mantle up to 100 times higher than the upper mantle and without a low viscosity asthenosphere. Such thick effective elastic lithosphere will lead to insignificant ongoing isostatic response of the glaciers decay, but the elastic response will still be as shown in Figure 5.

Conclusion

Most Norwegian mountain glaciers melted away in a period between 8 000 and 6 000 cal yr BP. This (warm) period was followed by the Neoglaciation which startet around 6 000 cal yr BP and ended with the Little Ice Age. After several periods of glacier growth and decay most of the Norwegian glaciers probably culminated in mid 1700s AD. The last 300 years is characterized by a very significant decay of the Norwegian mountain glaciers.

The calculated ongoing isostatic response of the glaciers decay is close to 2 mm/yr in areas of northern and southern Norway, while the elastic response is close to 1 mm/yr in northern Norway. The total present uplift of the combined isostatic and elastic response of the mountain glaciers unloading exceeds 2 mm/yr both in northern as well as southern Norway.

Editor: Geir Hasnes; Reviewers: Anonymous.

References

Amantov, A., Fjeldskaar, W., 2013. *Geological - geomorphological features of the Baltic region and adjacent areas: imprint on glacial - postglacial development*. Regional Geology and Metallogeny, St. Petersburg. No. 53, 90-104, St. Petersburg. УДК 551.4:551.793(262.24)

Bakke, J., Dahl, S.O., Paasche, Ø., Riis Simonsen, J., Kvisvik, B., Bakke, K., Nesje, A., 2010. *A complete record of Holocene glacier variability at Austre Okstindbreen, northern Norway: an integrated approach*. Quat. Sci. Rev., 29, pp. 1246-1262

Cathles, L.M., 1975. *The Viscosity of the Earth's Mantle*. 386 pp., Princeton Univ. Press, Princeton, N.J.

Fjeldskaar, W., Amantov, A., Bungum, H., submitted. *The present rate of uplift in Fennoscandia – northern Norway glacial-isostatic anomalies and possible relations to seismic activity.*

Fjeldskaar, W., Bondevik, S., 2020. *The Early-Mid Holocene transgression (Tapes) at the Norwegian coast – comparing observations with numerical modelling.* Quaternary Science Reviews**,** DOI: 10.1016/j.quascirev.2020.106435.

Fjeldskaar, W., Amantov, A., 2017. *Tilted Norwegian post-glacial shorelines require a low viscosity asthenosphere and a weak lithosphere*. *Regional Geology and Metallogeny* No 70, p. 48-59. УДК 551.435.4.038:551.14/.15(481:26).

Fjeldskaar, W., Cathles, L., 1991. *Rheology of mantle and lithosphere inferred from post-glacial uplift in Fennoscandia. In Sabadini, R., Lambeck, K. and Boschi, E. (eds): Glacial Isostasy, Sea Level and Mantle Rheology*. Kluwer Academic Press, p. 1-19.

Fjeldskaar, W., Lindholm, C., Dehls, J.F., Fjeldskaar, I., 2000. *Post-glacial uplift, neotectonics and seismicity in Fennoscandia. Quaternary Science Reviews*, Vol. 19, 1413-1422.

Fjeldskaar, W., 2000. *How important are elastic deflections for the Fennoscandian post-glacial uplift?* Nor. J. Geol.. 80, 51-56.

Fjeldskaar, W., 1997. *The flexural rigidity of Fennoscandia inferred from the post-glacial uplift. Tectonics* 16, 596-608.

Fjeldskaar, W., 1994. *Viscosity and thickness of the asthenosphere detected from the Fennoscandian uplift*. Earth and Planetary Science Letters 126, 399-410.

Kaufman, G., Amelung, F., 2000. *Reservoir-induced deformation and continental rheology in vicinity of Lake Mead*, Nevada. Journal of Geophysical Research: Solid Earth, 105(B7), 16341-16358. [2000JB900079].

Mörner, N.-A., 1980. *The Fennoscandian uplift: geological data and their geodynamical implication* In: Earth Rheology, Isostasy and Eustasy (N.-A. Mörner, Ed.), p. 251-284. John Wiley & Sons

Nesje, A., 2009. *The Latest Pleistocene and Holocene alpine glacier fluctuations in Scandinavia.* Quaternary Science Reviews 28, 2119-2138. https://doi.org/10.1016/j.quascirev.2008.12.016

SCC

What Causes Increasing Greenhouse Gases?

Summary of a Trilogy

Correspondence to
harde@hsu-hh.de

Vol. 2.3 (2022)
pp. 297 - 301

Murry Salby[†1], *Hermann Harde*[2]

[1]*Ex Macquarie University, Sydney, Australia*

[2]*Helmut-Schmidt-University, Hamburg, Germany*

The Intergovernmental Panel on Climate Change (IPCC) classifies the human influence on our climate as extremely likely to be the main reason of global warming over the last decades. Particularly anthropogenic emissions of carbon compounds, with carbon dioxide (CO_2) as the main culprit and methane (CH_4) as a distant second, are made responsible for the observed temperature changes, while any natural forcings are almost completely excluded.

This post summarizes the results of three studies [1-3] addressing the question, how much human or native emissions can be made responsible for the observed increase of Greenhouse Gases (GHG), in particular the rising mixing ratio of CO_2 in the atmosphere.

I. Control of Atmospheric CO_2: Relation of Carbon 14 to the Removal of CO_2

In a first study we perform an in-depth analysis on the record of atmospheric $^{14}CO_2$, an isotopic tracer of CO_2, to better understand how CO_2 is removed from the atmosphere [1].

The observed CO_2 evolution, inclusive of its annual cycle, has recently been reproduced in numerical simulations [4-7]. They show, how the abundance of CO_2 in the atmosphere is controlled by a competition between two opposing influences, the feed of CO_2 through emission, and its removal through absorption, both at the Earth's surface. This competition governs time-mean CO_2, where absorption figures centrally. It determines if and how fast CO_2 grows, as well as the magnitude of its perturbation, e.g., by anthropogenic emission. Yet, actual observations of CO_2 absorption are scarce. However, the impact of global absorption on atmospheric CO_2 is represented in carbon 14, an isotope of atmospheric carbon that has been observed in the troposphere since the 1950s [8].

Carbon 14 has a radioactive decay time of 8267 years (e-folding time). On time scales of relevance, the operation of $^{14}CO_2$ is virtually identical to that of the preponderance of carbon dioxide molecules, $^{12}CO_2$, comprised chiefly of the stable isotope carbon 12. Dynamical, chemical, and thermodynamic processes acting on those two isotopes of CO_2 (including those in the biosphere) are, for practical considerations, indistinguishable.

This feature makes carbon 14 a unique tracer of atmospheric CO_2 and provides an unrivalled means, through which to understand key mechanisms controlling the evolution of atmospheric CO_2. Once CO_2 is introduced into the atmosphere, whatever influence is experienced by one isotope is experienced by the other. Owing to this property and its artificial enrichment by nuclear testing, ^{14}C is central to estimates of CO_2 absorption, which vary widely. Absorption, in turn, is essential to understanding changes of atmospheric CO_2.

During the 1950s and early 1960s, atmospheric testing of nuclear devices sharply enriched ^{14}C in the stratosphere. Through the atmospheric circulation, ^{14}C-enriched air in the stratosphere was subsequently transferred into the troposphere. By 1963, when the Nuclear Test Ban Treaty

(NTBT) was implemented, tropospheric ^{14}C had increased by nearly 100%. The NTBT virtually eliminated the anomalous nuclear source of ^{14}C, leaving its perturbation of ^{14}C to decline through absorption and overall ^{14}C to return to its unperturbed equilibrium abundance. Represented in the decline of ^{14}C is the removal of all CO_2, through its absorption at the Earth's surface.

Our analysis of the ^{14}C record reveals that in addition to long-term behavior it is also important to consider short-term changes that have been largely ignored. Those changes exhibit the underlying mechanisms responsible for the observed decline of atmospheric $^{14}CO_2$ and, thereby, for removal of overall CO_2. They represent effective absorption that is considerably faster than appears in the average decline of $^{14}CO_2$, initially and also later in its long-term decline.

This means we have to distinguish between direct absorption with an absorption time of only about 1 yr, and an effective absorption with an absorption time τ_{eff} up to 10 yrs, the latter depending on the degree of re-emission of previously absorbed CO_2 back from the Earth's surface to the atmosphere [6].

Fluctuations of emission operating on time scales of only a couple of years introduce anomalous CO_2 that falls within the short-time regime, i.e., before re-emission can intensify and offset direct absorption. Such perturbations will therefore experience effective absorption that is fast, comparable to direct absorption. On the other hand, emission that varies slowly or is invariant will introduce anomalous CO_2 that falls within the long-time regime, when re-emission has intensified and offsets direct absorption. Such perturbations will therefore experience effective absorption that is slow, operating at only a fraction of the pace of direct absorption.

The average decline of $^{14}CO_2$ is slowed initially by periodic re-enrichment from the stratosphere, which offsets direct absorption at the surface. Finally, however, its decline is slowed by re-emission of absorbed $^{14}CO_2$ from the surface, which likewise offsets direct absorption. Based on these fundamental principles and solving the coupled balance equations for the stratosphere, the troposphere and Earth's surface this reproduces the observed evolution of $^{14}CO_2$, on long as well as short time scales.

Applying the same considerations to anthropogenic emission of CO_2 recovers effective absorption that is an order of magnitude faster than the mean decline of $^{14}CO_2$. The difference follows from magnified disequilibrium between the atmosphere and the Earth's surface. While $^{14}CO_2$ was perturbed impulsively by nuclear testing, the absorption of anthropogenic CO_2 is perturbed continuously by fossil fuel emission. This continuous anthropogenic emission maintains a disequilibrium between the atmosphere and the surface. Thereby, it inhibits a larger offset of direct absorption by re-emission and thus, results in faster effective absorption of anthropogenic CO_2.

Altogether, the observed behavior of $^{14}CO_2$ provides an upper bound on the anthropogenic perturbation of atmospheric CO_2, which can only contribute a few percent of the observed increase.

From the IPCC's own estimates of extraneous carbon reservoirs, the anthropogenic contribution to increased CO_2 has been shown to be no more than 15% - 35% [4 - 7]. The present analysis does not rely upon such estimates and shows that the anthropogenic perturbation must even be smaller.

II. Control of Atmospheric CO_2: Influence of Tropical Warming

In the second part of this three-pronged study we explore an important natural influence that likewise figures in the control of atmospheric CO_2 [2]. Surface processes which regulate emission and absorption of CO_2 depend intrinsically upon temperature. Many, like soil respiration, even increase exponentially with temperature, typical of Arrhenius temperature dependence that operates in chemical reactions underpinning surface processes.

Global temperature today is ~ 0.7 K warmer than it was half a century earlier. The most reliable record of global temperature is the satellite record from the Microwave Sounding Unit (MSU) suite of instruments [9], which retrieves temperature with homogeneous and near-global sampling

of the Earth. It indicates that over much of the Earth, surface temperature underwent no systematic (e.g., ubiquitous) heating during the last four decades, over which it was observed by MSU. Perceptible heating was only introduced by just two brief intervals, both not more than about two years long: one preceding the El Niño 1997, the other the El Niño 2016. Such heating in 20 years separated steps would be virtually impossible by continuously emitted anthropogenic GHG, which are mainly released in the northern midlatitudes.

Exceptional, however, is surface temperature in the tropics, where temperature systematically increased during the four decades observed by MSU. The sustained increase is also mirrored in the independent record of anomalous sea surface temperature from the Hadley Centre [10].

Owing to the dependence on temperature of physical and chemical processes that regulate CO_2 emission, CO_2 must have experienced a parallel influence. This can directly be scrutinized by investigating the interdependence of the observed temperature records and the *net* CO_2 emission, the component of emission that actually changes CO_2 and is derived from the measured concentration in the atmosphere as the instantaneous rate of change of CO_2.

As widely accepted reference we rely on the measurements of CO_2 at Mauna Loa, Hawaii [8], which are largely free of local distortions, at least till November 2022. They approximate the global abundance of CO_2, which, on time scales longer than a month, is well mixed over the free atmosphere.

Thermally-induced emission, especially from tropical land surface is found to represent much of the observed evolution of net CO_2 emission. It accounts for sporadic intensifications of net emission that operate on interannual time scales, notably, during the episodes of El Niños, and equally well for the long-term intensification during the last half century. Jointly, these unsteady components of net emission determine the thermally-induced component of anomalous CO_2 and closely track the observed evolution of CO_2 (see also Part III, Figure 1).

The veracity with which the thermally-induced component reproduces the observed evolution of CO_2 has two important implications: (i) Tropical land temperature should be a robust predictor of atmospheric CO_2. By contrast, other contributions to net emission which operate incoherently with the temperature afford virtually no predictive skill. Such is the case for anthropogenic emission, upon which climate projections of the IPCC rest. (ii) The anthropogenic perturbation of CO_2 must be so small to lie almost within the noise of calculation. It can represent but a few percent of increased CO_2. That, in turn, requires a removal time, which must be of order only a year. Anthropogenic CO_2 is then removed from the atmosphere almost as fast as it is introduced, sharply limiting its accumulation in the atmosphere (see Part I).

In relation to CO_2, what is responsible for that warming is immaterial. Its influence on CO_2 should not be confused through circular reasoning. The observed warming, which forces increased CO_2 through intensified net emission, cannot itself be the result of increased CO_2. Otherwise, anomalous CO_2 and net emission that forces it would have increased twice as much as was observed: (i) the increase required to produce the observed warming plus (ii) the thermally-induced response to that warming, which, irrespective of what caused the warming, induces an intensification of net emission that is nearly identical to what is observed.

The direction of causation is also clear from the interdependence of net emission and temperature - for interannual fluctuations as well as for the long-term increase. In addition to having strong coherence with temperature, the two unsteady components of net emission have the same phase relationship to temperature, both varying *in phase* with temperature. The strong coherence and in-phase relationship to temperature reveal that, irrespective of time scale, changes of tropical temperature induce simultaneous changes of CO_2 net emission.

Under the opposite direction of causation, were the observed changes of tropical temperature induced by changes of CO_2, they would result in a fundamentally-different phase relationship. The time scale of thermal damping, which drives temperature towards thermal equilibrium, is only a couple of weeks. It is much shorter than both unsteady time scales. Through anomalous radiative

forcing, the comparatively gradual changes of CO_2 would therefore induce simultaneous changes of temperature, in phase with CO_2. However, net emission, which changes CO_2, must lead CO_2 by a quarter cycle. Net emission would thus also lead temperature by a quarter cycle - behavior contradicted by their observed in-phase relationship. Net emission of CO_2, which determines anomalous CO_2, is forced by changes of tropical temperature - not vice versa.

III. Theory of Increasing Greenhouse Gases

In the third and culminating part of this trilogy we investigate the physical mechanisms, through which observed warming can produce the observed evolution of CO_2 [3].

Our preceding studies on nuclear-perturbed carbon 14 [1] and on thermally-induced emission, notably in the tropics [2], were inspired by numerical simulations which, on the basis of observed temperature, were able to reproduce the observed evolution of atmospheric CO_2, including its annual variation and stepwise increase [4 - 6]. In this contribution we integrate these findings and explore the underlying physical mechanisms in an in-depth analysis by calculating the net emission of tropical oceans and land as response to temperature variations.

The conservation law governing atmospheric CO_2, supported by the *observed* temperature dependence of surface fluxes and *observed* temperature in the tropics, is then used, first to calculate the time-varying response of CO_2 net emission and as integral the atmospheric concentration or mixing ratio r_A, which can directly be compared with measurements at Mauna Loa [7].

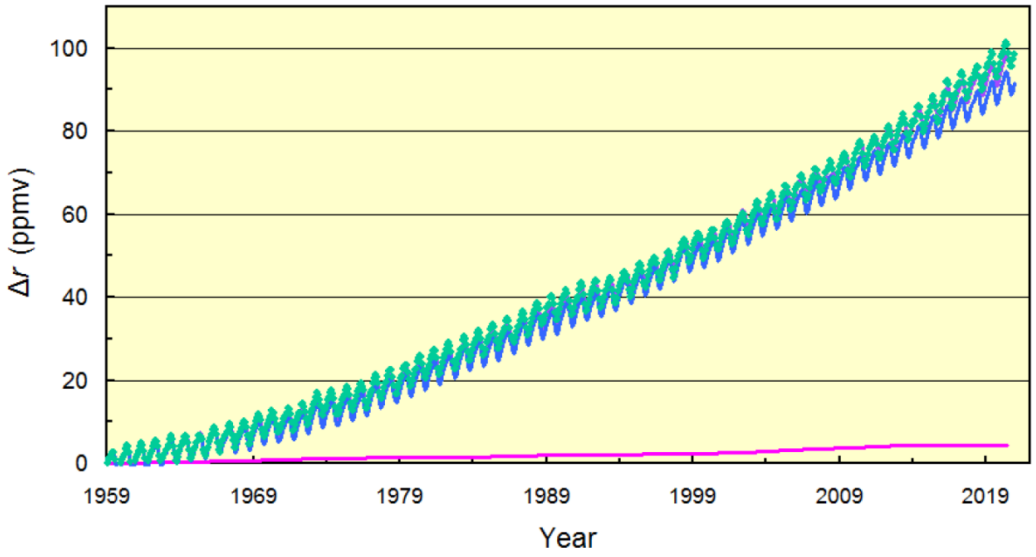

Figure 1: Observed increase of CO_2 (Green), compared against the calculated increase (Purple) that lies mostly beneath observed CO_2, but emerges near the end of the record. Plotted separately is the contribution from thermally-induced emission (Blue) and from anthropogenic emission (Magenta).

In Figure 1 is displayed the observed increase of r_A (Green). Superimposed is the calculated anomalous CO_2 that is forced by the total emission (Purple - almost completely covered by the Green Graph). It closely tracks the observed evolution of anomalous CO_2. Almost as closely tracks the calculated component of thermally-induced CO_2 (Blue).

Also superimposed in Fig. 1 is the anthropogenic component of anomalous CO_2 (Magenta). Comparatively small, it tracks the instantaneous equilibrium level of anthropogenic CO_2. With an effective absorption time of about 1 yr, as this results from an independent analysis of the induced anthropogenic CO_2 changes, relative to mean net emission during the Mauna Loa era, the anthropogenic component represents not more than 4% (see also Part I).

Like carbon dioxide emission, also CH_4 emission increases with temperature. It too is emitted by

biomass, chiefly through anaerobic processes that operate in well-irrigated regions like wetlands, and those influences magnify CH_4 emission particularly from tropical land, where biomass and precipitation are abundant.

The simultaneous intensification of CO_2 and CH_4 emission is precisely what is expected from observed warming in the tropics. Therefore, this single physical mechanism provides a unified understanding of the joint increase of these greenhouse gases, one that follows naturally from thermally-induced emission.

Altogether we find a strong correspondence to observed net emission that follows theoretically from behavior in the tropics - not in the extratropics, where anthropogenic emission is concentrated. Independently, the same correspondence to observed net emission follows empirically from anomalous temperature in the tropics (see Part II), as well as from a time-lag analysis of anomalous CO_2 [11].

In both theoretical and empirical evaluations, thermally-induced emission of CO_2 represents interannual intensifications of net emission, notably during episodes of El Niño. Represented equally well is the long-term intensification of net emission during the last half century. The strong correspondence to observed changes indicates that, although operating on disparate time scales, both unsteady components of CO_2 net emission share the same physical mechanism.

References

1. M. Salby, H. Harde, 2021: *Control of atmospheric CO_2 - Part I: Relation of carbon 14 to the removal of CO_2*, Science Climate Change Vol. 1, No. 2, pp. 177-195, https://doi.org/10.53234/scc202112/30.
2. M. Salby, H. Harde, 2021: *Control of Atmospheric CO_2 - Part II: Influence of Tropical Warming*, Science of Climate Change, Vol. 1, No.2, pp. 196-212, https://doi.org/10.53234/scc202112/12.
3. M. Salby, H. Harde, 2022: *Theory of increasing greenhouse gases*, Science of Climate Change, Vol. 2, No. 3, pp. 212-238, https://doi.org/10.53234/scc202212/17.
4. H. Harde, 2017: *Scrutinizing the carbon cycle and CO_2 residence time in the atmosphere*, Global Planetary Change, 152, pp. 19-26, http://dx.doi.org/10.1016/j.gloplacha.2017.02.009
5. H. Harde, 2019: *What humans contribute to atmospheric CO_2: Comparison of carbon cycle models and observations,* Earth Sciences, 8, pp. 139-158, https://doi.org/10.11648/j.earth.20190803.13
6. H. Harde, M. Salby, 2021: *What controls the atmospheric CO_2 level?* Science of Climate Change, Vol. 1, No. 1, pp. 54 - 69, https://doi.org/10.53234/scc202106/22.
7. E. Berry, 2021: *The impact of human CO_2 on atmospheric CO_2*, Science of Climate Change, Vol. 1, No.2. pp. 213-249, https://doi.org/10.53234/scc202112/13.
8. CDIAC, 2017: Carbon Dioxide Information Analysis Center, ESS-DIVE Archive, https://cdiac.ess-dive.lbl.gov/,
9. R. Spencer, J. Christy, D. Braswell, 2017: *UAH version 6 global satellite temperature products: Methodology and results*, Asia-Pacific J. Atm. Sci., 53, 121-130.
10. J. Kennedy, N. Rayner, C. Atkinson and R. Killick, 2019: *An ensemble data set of sea surface temperature change from 1850: The Met Office Hadley Centre HadSST.4.0.0.0 Data Set*, JGR Atmospheres, 124, 7719-7763.
11. O. Humlum, K. Stordahl and J.-E. Solheim, 2013: *The phase relation between atmospheric carbon dioxide and global temperature,* Global Planetary Change, Vol. 100, pp. 51-69.

On the Theory of the Earth's Physical Parameters, Distributed in Space and Time

C.(Kees) le Pair and C.A.(Kees) de Lange

CLINTEL, The Netherlands

Correspondence to clepair@casema.nl

Vol. 2.3 (2022)

pp. 302-309

Abstract

Present day treatises dealing with weather and climate often use seemingly physical quantities, while they are in fact averages of such. Inserting these into formulas is physically not permitted. It leads to an assumption of the magnitude of the so-called 'greenhouse effect' several tens of K off. The often-used explanation of the 'average temperature of the earth' of 288 K is physically untenable. Another widely accepted property of the greenhouse, the 'back radiation', violates elementary thermodynamics. A well-insulated, sun-heated home is a better model. It would diminish the role of atmospheric CO2. Air in general is a fairly strong insulator and also a good heat transporter depending on mass motion and latent heat. The article presents theoretical and experimental arguments in support of these statements.

Keywords: Greenhouse effect; averaging temperatures; opaque and transparent media; sun-heating.

Submitted 22-11-2022, Accepted 12-12-2022. https://doi.org/10.53234/SCC202212/15

1. Introduction

The notion 'the earth's climate' is vague and non-physical. There is no measurable quantity associated with it. We can take local measurements of temperature (T), pressure (P), humidity, precipitation, incident radiation (Ieff), etc., but these quantities vary, not only with geographic location, but also with time, altitude, and depth. Several quantities only have a definite meaning in a well-defined volume and in a state of equilibrium, which on earth rarely prevails. One can calculate averages over locations and time periods, but such values have little overlap with the human experience on Earth. The local climates of Greenland and the Sahara are very different. Moreover, taking averages has no physical meaning.

In response to societal requests, meteorologists have developed admirable techniques, that, with certain probability in a limited time interval, will predict T, precipitation, wind force, etc. Weathermen translate those forecasts into terms such as 'fair in the morning with showers in the afternoon followed by a cool night'. International co-operation, better measuring techniques, increasing the number of weather stations, balloons, radar, satellites, greatly improved computation facilities, and additional knowledge of the atmospheric transport processes allow for an extension in the time interval for which forecasts have some validity.

This time interval is now approximately a week. (In fact, when comparing predictions with later measurements and by utilising probability theory, the forecasts have significance over a longer range. However, to a farmer, a 55% chance of frost after 8 days and a 45% chance of a heat wave is useless).

There is a difference between our tacit implicit knowledge of the climate and the capacity of

meteorology to predict the weather. Suppose that on December 22nd we wish to predict the temperature around noon on January 31 . Meteorology is unable to provide an answer. However, we all know that, in all probability, it will be colder by then, despite the sun being higher in the sky end of January. In order to get some idea about the evolvement of the physical parameters, processes other than those taking place in the atmosphere alone play a key role. Changes in solar activity, the role of the biosphere, and the oceans covering about 70% of the surface of the earth should be considered.

The retention of heat within our oceans and the Earth's solid surface is vital for the energy balance of our planet. The effects on the distribution of parameters such as P,T over location and time are major. These influences are handled as perturbations on the atmospheric circulation models in current computations. However, there is evidence that relevant relaxation times might stretch over periods of hundreds of years. Ice core measurements on glacial cycles show that rise and fall of atmospheric CO_2 concentration lags about 700 years behind rise and fall of atmospheric temperature. The ocean needs time to warm up before it releases its dissolved CO_2. Major influences of this kind are unsuitable to be dealt with by perturbation theory.

The term 'the Earth's temperature' is frequently used, while the concept is an ill-defined fallacy. The temperature of the Earth's core is about 5000 K. The air temperature about 10 km above the surface is usually around 223 K. That is roughly the same as the temperatures in the polar regions at ground level. Elsewhere, temperatures may reach 323 K. In scientific papers 288 K is often mentioned as the average surface temperature. As we shall demonstrate in sections 2 and 3, this value is not explained through physics, or rather, the explanation is wrong. This value of 288 K is the starting point for hypotheses on temperature change and its causes. It is the unsolid base for public discussions and government measures, referred to as the average of station temperatures 2 m above ground. There is some fuzziness about the inclusion of polar regions, partly due to the scarcity of data available. It remains unclear how one can scientifically justify how to compare measurements at sea level with those in mountainous regions and on high-level plateaus.

2. Averaging temperatures and Stefan-Boltzmann (SB)

In a nutshell, the current assumption about the 'temperature of the Earth' is the AGW (anthropogenic global warming) hypothesis. A solid black sphere at our distance from the Sun with albedo $\alpha = 0{,}3$ and emissivity $\varepsilon = 1$ absorbs and emits equal amounts of radiation. It would have a stable temperature of 255 K, according to Stefan-Boltzmann's Law, $Ieff = \sigma T4$ (the SB- constant, $\sigma = 5{,}67... \cdot 10^{-8}$ $Wm^{-2}K^{-4}$).

The measured averaged temperature of the Earth (2 m) is 288 K. The difference of 33 K is bridged by the atmospheric greenhouse effect, a radiative phenomenon mainly provided by H_2O and CO_2. Adding to the latter raises the temperature. The strength of the CO_2 contribution is discussed in terms of CO_2 sensitivity and is said to be about +1 K in case of doubling of the CO_2 concentration. This temperature increase is subsequently re-enforced by more H_2O vapour into the atmosphere, referred to as a positive 'forcing' or feedback, resulting in a combined effect between +1,5 K and + 4 K. Other influences that may affect temperature are either not considered or assumed to remain constant.

However, this AGW hypothesis, rests on two assumptions: first, the solid black sphere distributes the energy received from the Sun uniformly over its surface, i.e. everywhere and all times the same temperature prevails; secondly, the sphere is opaque and may be

treated as a SB-radiator, while the Earth is merely a (semi-)transparent body. This second point will be dealt with in section 3.

Assuming a completely equalised temperature over the total radiative surface of the Earth is clearly disregarding the observations. Due to a lack of data concerning the real temperature distribution, we look at the opposite extreme of a completely uniform temperature. That would be every square meter at any moment in equilibrium with the there and then incoming solar energy; or at 3 K, the temperature of the universe in dark places. Such a sphere would also maintain a constant average surface temperature. Properly calculated, with the same α and ε like in the case of the uniform temperature, we find an average temperature T = 145 K. Please note the difference 255 K and 145 K. This shows that a small change in temperature distribution would have a dramatic effect on the average temperature.

A picture of the radiation balance used in the AGW hypothesis is given in Figure 1. It underlines the role of greenhouse gases and shows a so-called 'backradiation' of 342 Wm^{-2}.

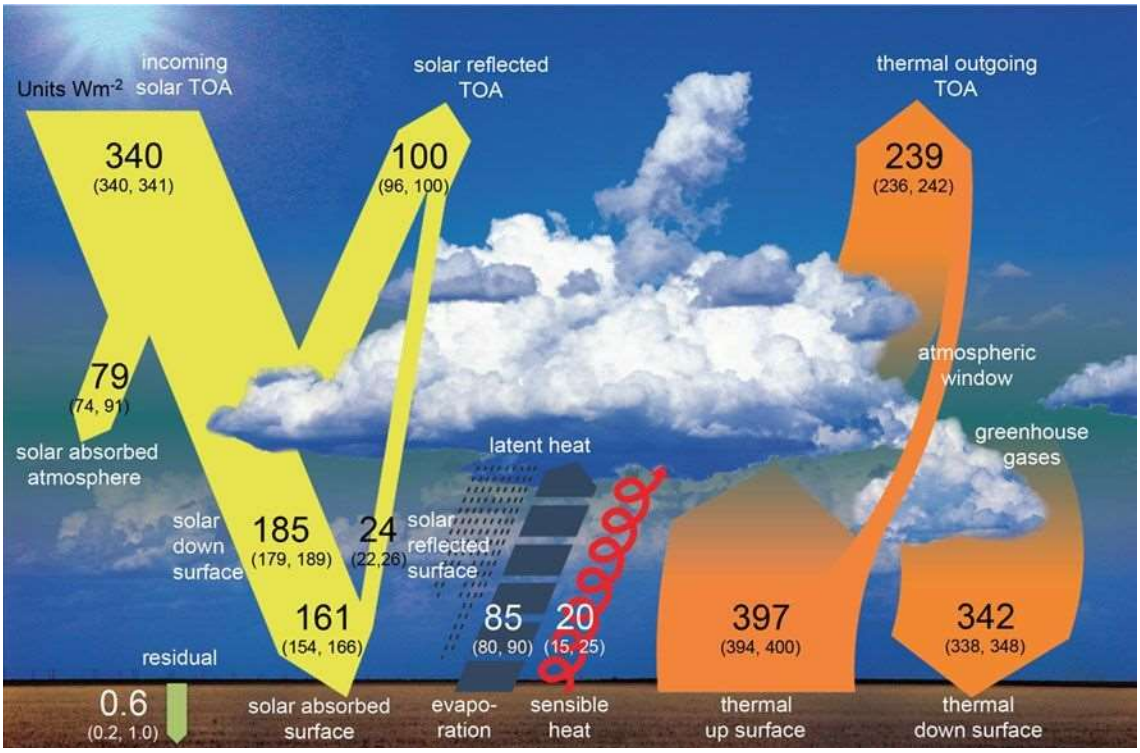

Figure 1. Radiation balance (AGW) with an appreciable role for greenhouse gases. (Wild et al. 2013).

The depicted back radiation is a physical curiosity, or oddity if you like. In the troposphere, the temperature normally decreases with altitude. According to the second law of thermodynamics, heat and thermal radiation do not flow against a temperature gradient. Mixing collective phenomena with quanta is tricky.

In conclusion, it is not correct to consider the temperature of 255 K as the base from which the greenhouse effect does its 'beneficial' work, namely, to raise the average temperature of the

Earth to 288 K. The greenhouse effect should either bridge a much wider gap than 33 K, perhaps even 40-60 K wider, or other factors should be invoked to make up for the deficit. If the 400 ppm CO_2 in the atmosphere, as well as the H_2O vapor, would make up 83 K instead of 33 K, a doubling of the CO_2 concentration would have a much stronger effect than the current 1 K predicted. In the last few years we have seen a steady decline in the estimated forcing in climate literature. We therefore reject the possibility of CO_2 as the main cause for an extensive greenhouse effect.

3. Opaque and transparent media

Many papers and textbooks on the climate issue treat the Earth as a solid opaque medium, radiating according to SB. The atmosphere and the oceans, however, are partly transparent. The solar energy penetrates. It passes through them and is absorbed following a general absorption law $I_d = I_o e^{-kd}$, in which k is a frequency dependent coefficient and d is the distance. The AGW hypothesis accounts for this effect only when dealing with the atmosphere. The greenhouse gases are supposed to block most infrared radiation, with a temperature augmentation of 33 K as a result. The oceans, however, are treated in a different way, although their heat capacity exceeds by far that of the atmosphere. In order to restore the energy balance in the oceans, the dissipated energy (at a depth of 100+ m) has to be transported back to the surface, and ultimately back to space. Since water has a high absorption coefficient for the relevant frequency range, this transport is mainly achieved by slow mass movement with help from conduction. At the surface, the options for transport are: evaporation, conduction, radiation and again mass movement. On solid ground the effect is different, but also there we have energy retainment, wich causes a radiative behaviour quite different from that of an opaque black body in which the surface temperature is determined by incoming light and immediate balancing SB-radiation.

These processes result in higher internal temperatures of turbid medium bodies than in solid opaque 'SB-bodies'. Since the transport processes and the interaction of different frequencies with matter are complicated, we have not been able to make verifiable estimates of the size of the effect. However, rough calculations (le Pair 2018) suggest that the turbidity effect is large enough to waive possible doubt on its determining influence on the temperature at all spatial locations relevant for climate on Earth.

We must therefore conclude that the AGW hypothesis and accompanying models are incomplete and undeserving of 'theory' status due to the unaccountability of the oceanic phenomenon and its smaller, solid-surface counterpart.

4. Origin of the greenhouse assumption

The greenhouse CO_2 supposition originated around 1975. The Earth had just gone through a 30 year cooling period, lasting from 1940 – 1972. Observe Figure 2; the GISS-NASA records of Arctic temperatures. After 1975 we entered a period in which atmospheric CO_2 and temperature seemed to rise at the same rate.

During those 30 years, climate scientists warned about an incoming ice age. They advised to decrease fossil fuel consumption in order to avoid this fate, see Figure 3.

Please note that the atmospheric CO_2 concentration in those days was rising as well, albeit at a slightly slower pace.

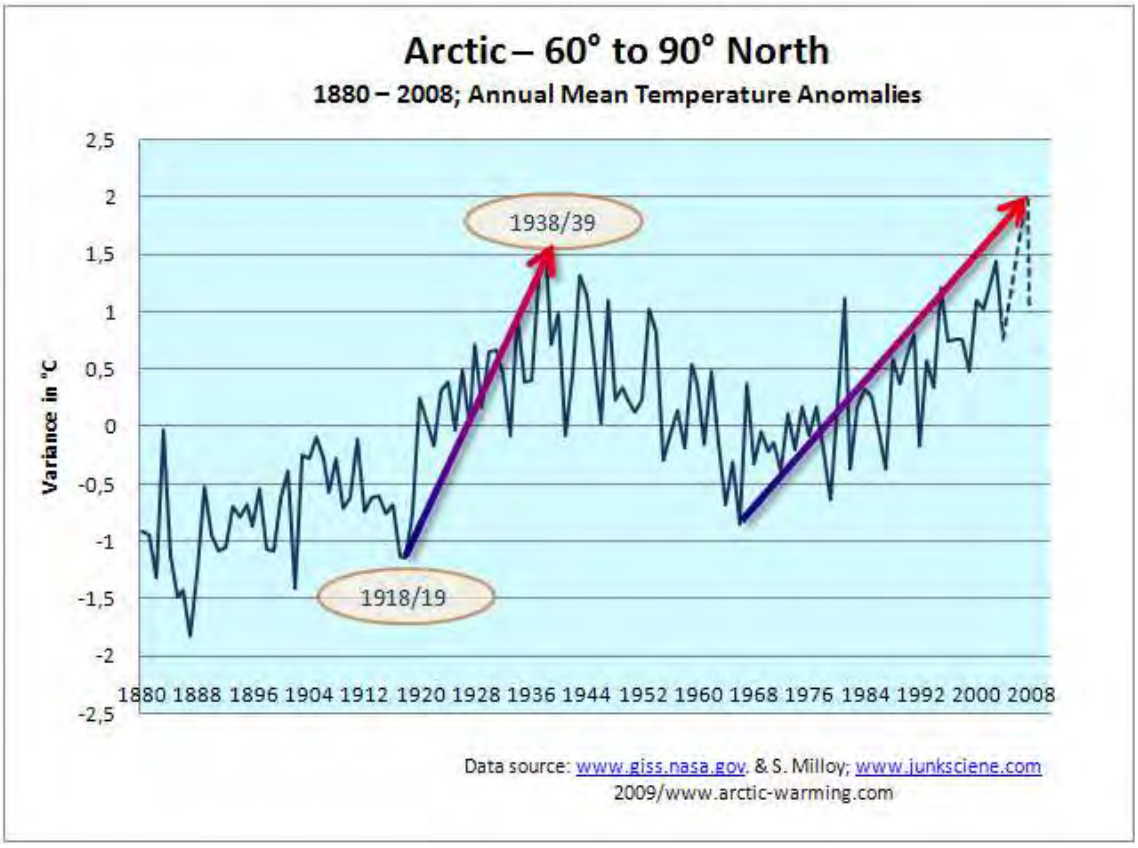

Figure 2. Arctic temperature variance relative to the year 1974, www.giss.nasa.gov.

Figure 3. Climate warning in 1971. Less fossil fuel consumption would prevent the ice age.

5. Ultimate test of the model

The real test for the AGW climate models is a comparison with experimental results. After all, a model may be a useful tool even if it contains mistakes. When some errors cancel each other, the instrument may still provide a useful rule of thumb. Observe the example of AGW projections of the tropical 'mid-tropospheric' temperatures as predicted by 32 model runs, used by the International Climate Panel IPCC. Figure 4 depicts these projections, alongside the satellite and balloon measurements during the period 1979 – 2018.

The atmospheric CO_2 content is the sole factor that determines the AGW model results. Furthermore, these models are parametrized to account for effects such as cloud formation, for which no hard physical laws exist. Even the IPCC has reservations about the long-term predictive power of complex climate models containing a multitude of non-linear coupled integro-differential equations. In any case, the predictions displayed in Figure 4 differ too much from the experimental satellite and balloon data available to be considered reliable theoretical predictions. The average model outcome shows a warming of 1,1 K during period 1979-2018. In the same period, the measurements show 0,4 K. This disparity disqualifies the predictive quality of the models. No real solid physical proof justifying the causal relationship between CO_2 and temperature exists, thus this result should come as no surprise. The only evidence presented consists of probabilistic calculations, which have been criticised by renowned statisticians due to the uncertainty of the data and shortage of time series.

Perhaps the most serious criticism of the AGW hypothesis is its assumption that no other natural phenomena cause climatological change except for atmospheric CO_2. We know from reliable

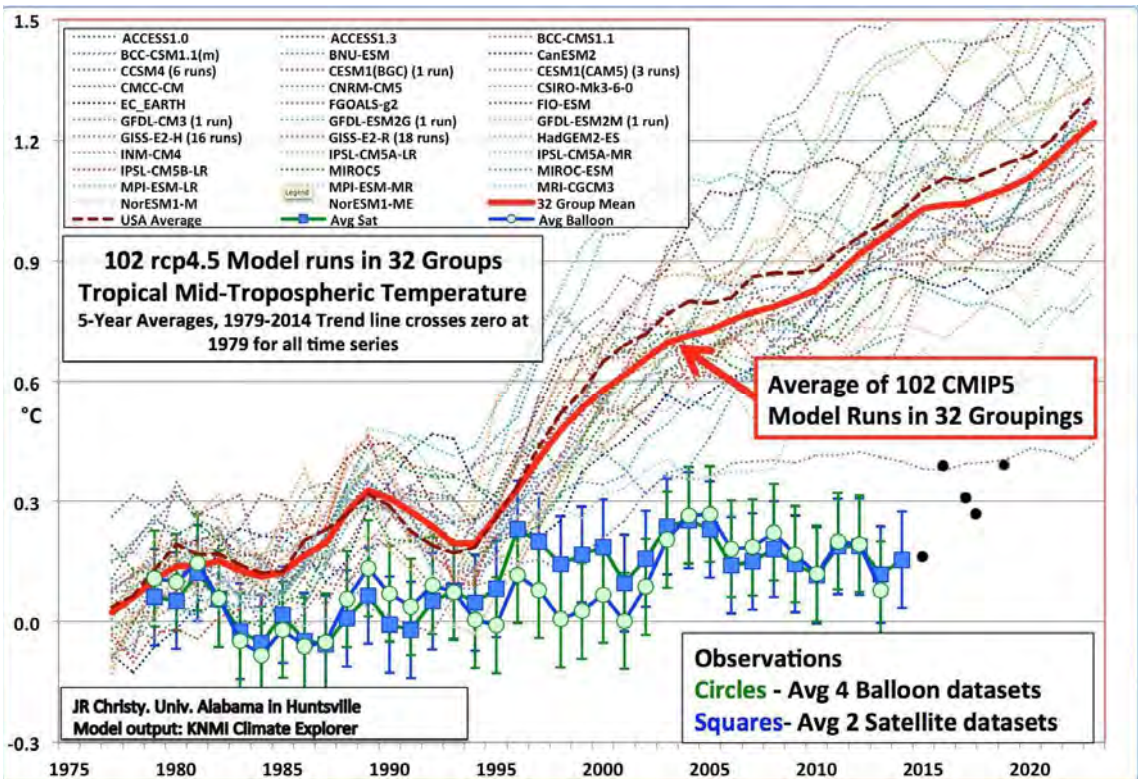

Figure 4. Comparison between AGW-model results and actual measurements. Explanations in the picture. J.R. Christy's, UAH, series ended 2014. We added later data provided by Roy Spencer of the same experiments, the black dots.

proxies that European temperatures in the Medieval Warm Period were higher than at present (e.g. glaciers were smaller then). At the moment, the world is recovering from the Little Ice Age, which was not a regional, but a world-wide event. It ended around 1670, after which proxy temperatures indicated a steady rise; long before industrialisation set in and humanity began to use fossil fuel in significant quantities. Moreover, the AGW claim that the only driver of warming is atmospheric CO_2 has been falsified. M. Lockwood (1999) revealed that the Sun's coronal magnetic flux increased by a factor of 2,3 (!) since 1901. Our prime heating source has undergone changes in some way.

The IPCC have also presented model calculations on the Arctic Sea ice extent (Eisenman et al. 2011). The 21 model runs show the percentage of minimum sea ice compared to the mean during the period 1980 – 2000. The runs cover all possibilities between 10% to 100% reduction in the period 2020 – 2100 (!). This does not deserve the qualification 'theory building'. It is merely a clumsy approach that declares the target to be whatever you hit afterwards. Whatever it may be, it is not physics.

Thus, by comparing AGW model results with the best measurements available in various areas, we may reject the CO_2 hypothesis without reservations. CO_2 may be influential, or it may not be. In any case, its role is overestimated.

6. Our Sun-heated home

With the greenhouse hypothesis rejected, the question arises: which theory describes the observed changes in the Earth's physical observables? Changes clearly occur. The rising sea level is the phenomenon which may well be the most conclusive indicator of the Earth's rising temperature. The level increase is caused by melting land ice and by the thermal expansion of the oceans. Nothing suggests that the ocean basin is shrinking due to tectonic movement, or that other esoteric causes are to blame. 15,000 years ago, the sea level was 120 m lower than at present.

The records from Dutch coastal stations are possibly the most trustworthy records to exist. They show a steady rise of 19 cm per century[1] during a period of some 150 years. Accidentally, this concurs with NOAA's world-wide average of coastal station data[2]. Due to tectonic movements, Dutch soil is sinking at a rate of roughly 4 cm per century, while the soil is rising in Scandinavia. Big land masses and ice masses make the sea's less level than is often thought. However, there is general consensus that sea levels rise, providing significant evidence to support global warming.

It is an undeniable fact that without oceans, atmosphere, O_2, N_2, H_2O, CO_2, CH_4 and some other rare gases our planet would be much less pleasant to inhabit. They act as insulators, radiation shields, heat transporters, heat storage and more, thus globally affecting temperatures, whether averaged or not.

The surplus energy collected in oceans and the Earth's surface is transported to higher atmospheric layers and, ultimately, out to space. Due to their low density, gases are notoriously bad

[1] https://tidesandcurrents.noaa.gov/sltrends/sltrends_station.shtml?id=150-031

[2] https://tidesandcurrents.noaa.gov/sltrends/sltrends_global.html

radiation emitters. Instead, the upper layers of the atmosphere are suitable insulators to keep us warm.

In section 3 we argued that in order to obtain temperatures significantly higher than those above a simple opaque surface irradiated by the Sun, one would not need infrared shielding as such. The effect of turbidity on the temperature distribution can be quite powerful. We visualise the Earth, our home, as a lone sphere orbiting the Sun wrapped in turbid blankets of water and air. On its path through space and time, it periodically catches different amounts of solar energy, which it accumulates, keeps, disperses, stores, re-emits and keeps as heat, bioenergy, chemical energy, and fossil energy for later use. Some processes take a second, other millions of years. It is much like keeping ourselves warm under a cosy cover in a cold night with a hot water bottle that is occasionally refilled.

How all these mechanisms really function in detail is not yet known. The processes are far too many and too complex. However, their existence is irrefutable. The future of young physicists is not without opportunity for new discoveries.

Nieuwegein, Monnickendam
2019 09 23.

This article appeared also on: Principia Scientific International: https://principia- scientific.org/on-the-theory-of-the-earths-physical-parameters-distributed-in-space-and-time/

Funding: None.

Editor: Jan-Erik Solheim; Reviewer: anonymous.

References

Eisenman, I., Schneider, T., Battisti, D.S. and Bitz, C. M., 2011, *Consistent Change in the Sea Ice Seasonal Cycle in Response to Global Warming,* Journal of Climate, 24 (20), 5325-5335. https://doi.org/10.1175/2011JCLI4051.1

le Pair, C., 2018, https://principia-scientific.com/radiation-balance-and-transparent-media-3/

Lockwood M., Stamper R., and Wild, M.N., *A Doubling of the Sun's Coronal Magnetic Field during the Past 100 Years.* Nature, 399, 437-439. http://dx.doi.org/10.1038/20867

Wild, M., Folini, D, Schar, Chr., Loeb, N., Dutton, E.G., and König-Langlo, G., 2013, *The global energy balance from a surface perspective*. Climate Dynamics 40 (11-12), 3107-34. https://doi.org/10.1007/s00382-012-1569-8